Simulation of charge transport in amorphous organic semiconductors

Zur Erlangung des akademischen Grades eines

DOKTORS DER NATURWISSENSCHAFTEN (Dr. rer. nat.)

von der KIT-Fakultät für Physik des
Karlsruher Instituts für Technologie (KIT)
angenommene

DISSERTATION

von

M.Sc. Pascal Friederich

Simulation of charge transport in amorphous organic semiconductors

Abstract

Amorphous organic semiconductors are used in many applications such as organic light emitting diodes (OLEDs) and organic photovoltaics (OPV). The almost unlimited variety of chemical compounds and material combinations makes experimental material and device improvement difficult. Theories describing the mechanism of charge transport in amorphous materials exist. Most of them rely on empiric material parameters, therefore rendering the prediction of charge mobility of unknown materials impossible. Thus, new models are required to understand relations between molecular structure and macroscopic thin film properties. The insight gained in such methods can then be used to systematically design materials with desired properties.

The challenge in modeling charge transport in amorphous materials is twofold. Models must incorporate effects on vastly different length scales ranging from the electronic structure of single molecules in the sub-nanometer scale to percolation effects on distances up to the micrometer scale. Charge mobility and energy dissipation during transport depend exponentially on the energy disorder in amorphous systems. This quantity arises from single molecule conformation and intermolecular interaction.

Simulation of charge transport in disordered materials requires the analysis of the electronic structure of atomistic molecular systems. In this work, a multiscale modeling approach is developed and used to describe charge transport in amorphous organic semiconductors. The model incorporates different established and newly developed simulation techniques on various levels of coarse graining. Comparison of the simulated charge mobility of nine widely used organic materials with experimental data shows the predictive capabilities of the model. Factorization of the charge carrier mobility allows the identification of single-molecule properties, which mainly determine charge mobility. Using design rules derived from this analysis, the widely used electron conducting molecule Alq_3 is systematically modified to maximize its electron mobility while preserving the energy levels to keep its optical properties stable. The most promising candidate of these simulations has been synthesized and characterized. The new compound aligns with the theoretical prediction and exhibits an electron mobility which is three orders of magnitude higher than the mobility of the initial material. This example is a proof of principle of rational *in-silico* material design.

Simulation von Ladungstransport in amorphen organischen Halbleitern

ZUSAMMENFASSUNG

Viele Anwendungen der organischen Elektronik wie beispielsweise organische Leuchtdioden (OLEDs) oder organische Photovoltaik (OPV) basieren auf amorphen halbleitenden Molekülen. Die fast unendlichen Variationsmöglichkeiten organischer Materialien erschweren gezielte experimentelle Materialentwicklung. Bestehende Theorien für den Ladungstransport in amorphen Materialien basieren weitgehend auf empirischen Materialparametern und können so nicht zur prädiktiven Vorhersage von Eigenschaften neuer Materialien benutzt werden. In dieser Arbeit werden Modelle entwickelt, die dem Zweck dienen, den Zusammenhang zwischen mikroskopischen Moleküleigenschaften und deren makroskopischer Leitfähigkeit zu verstehen und somit die Ladungsträgermobilität neuer Materialien vorauszusagen.

Zwei Aspekte stellen bei der Entwicklung von Modellen für den Ladungstransport in amorphen Materialien besondere Herausforderungen dar. Zum einen müssen Effekte auf vielen Größenskalen berücksichtigt werden, die von der elektronischen Struktur einzelner Moleküle in Subnanometerbereich bis hin zu Perkolationseffekten im Mikrometermaßstab reichen. Zum anderen hängt die Ladungsträgermobilität exponentiell von der Energieunordnung im amorphen Material ab. Diese wird von der Konformation einzelner Moleküle sowie von deren Wechselwirkung mit ihrer ungeordneten Umgebung bestimmt.

Um die Effekte auf allen Größenskalen zu berücksichtigen, wird in dieser Arbeit ein Multiskalenmodell zur Simulation von Ladungstransport in organischen Halbleitern vorgestellt. Die Energieunordnung atomar aufgelöster Morphologien wird mithilfe der Quantum Patch Methode bestimmt, die die elektronische Struktur amorpher Moleküle selbstkonsistent bestimmt. Die mit diesem Modell berechnete Ladungsträgermobilität zeigt gute Übereinstimmung mit experimentellen Daten. Darüber hinaus erlaubt das Modell eine Zerlegung der Ladungsträgermobilität in Faktoren, die von einzelnen Moleküleigenschaften abhängen. Dies ermöglicht die Ableitung von Designkriterien für neue organische Moleküle. Mithilfe dieser Kriterien wurde die Elektronenmobilität eines bekannten Materials durch Änderung der chemischen Struktur gezielt erhöht. Bei dieser Modifikation wurden die Energielevels bewusst konstant gehalten, um optische Eigenschaften nicht zu verändern. Das somit gewonnene Material wurde synthetisiert und elektronisch charakterisiert. In Übereinstimmung mit den theoretischen Vorhersagen zeigt das Material eine um drei Größenordnungen erhöhte Elektronenmobilität. Dieses Beispiel demonstriert die Durchführbarkeit von *in-silico* Materialentwicklung.

Contents

1

Introduction

Organic semiconductors are a class of materials with a wide range of applications such as organic photovoltaics (OPV) [1–4], organic light emitting diodes (OLEDs) [5, 6] and organic field effect transistors (OFETs) [7, 8]. Each of these applications has its own advantages and disadvantages in comparison to their inorganic counterparts. Commercially available OLED displays (Fig. 1.1) are an energy efficient alternative to conventional LED displays. They can be manufactured to be semi-transparent and flexible, making new types of display design and integration possible. A major drawback is their limited lifetime and color stability currently preventing the application in lighting technologies. Organic solar cells on the other hand are less efficient than silicon based photovoltaics or thin-film technologies such as CIGS solar cells [9, 10]. Their advantages are potentially easier and cheaper production techniques such as roll-to-roll printing as well as the application in lightweight mobile devices. Organic field effect transistors can be integrated in cheap electronic devices, where the transistor size and speed does not play a crucial role. Examples are printable RFID tags, which are used as identifiers in hundreds of different areas related to logistics [11]. Another possible application is the combination of OFETs with (transparent) OLED displays which require logic circuits in the background.

Although OLED displays have been commercially available for several years, there are many physical aspects of organic electronics in general which are to date not well understood. Many theories and models exist to describe coherent charge transport in crystalline, inorganic materials. The fundamental mechanism of charge transport in disordered materials is also understood. Nonetheless, quantitative methods for the calculation and prediction of charge transport properties of new materials are lacking. Macroscopic properties of amorphous material de-
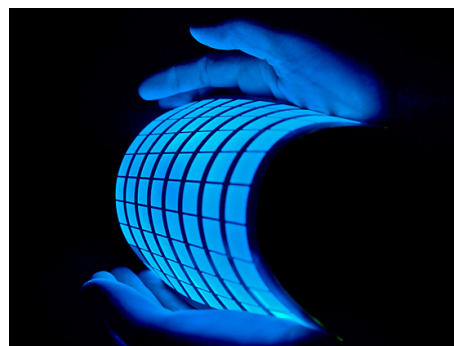
Figure 1.1: Organic light emitting diode (OLED) (source: computerworld.ch).

pend on mesoscale ordering effects as well as on electronic properties of single molecules. This interdependence of different length scales makes it challenging for analytic models as well for numerical methods to describe all relevant processes of charge transport. New concepts and models are required to close the gap between molecular properties on the nanometer scale and macroscopic thin film characteristics. Multiscale modeling is one way to describe the physics of charge transport on different time and length scales and therefore understand fundamental properties of organic materials.

One of the advantages of organic materials is the nearly infinite variety of different molecules which can be used for various applications. Macroscopic material properties can be controlled and fine-tuned by chemical functionalization and design, by adjustment of the nano- and micromorphology of amorphous thin films and by employing mixtures of materials. Prominent examples are guest-host systems and chemically doped layers as used in almost all available OLEDs or phase separated bulk heterojunctions in organic solar cells. To systematically explore and exploit this diversity of materials and their combinations, fundamental questions have to be solved concerning microscopic processes and mechanisms. Systematic improvement of the charge carrier mobility of organic materials requires detailed understanding of molecular properties as well as reliable theoretical methods to predict these properties. Due to the complexity of the systems, purely analytical approaches tend to fail in fully covering all relevant effects. Therefore, different analytical and numerical approaches have to be combined to describe all relevant processes on many different length and time scales.

In this work, I will address several of the aforementioned challenges. The incorporation of different length scales was tackled by development and implementation of a multiscale approach for the simulation of charge transport in disordered organic materials. The methodology of this approach is presented in Chapter 3 and

specifically in Chapter 3.1. It consists of several successive steps building upon one another. For the generation of atomistic morphologies, molecule specific force field parameters are required. These are determined using a quantum mechanical analysis of single molecules. The parameters obtained in this first step are then used in classical molecular dynamics or Monte Carlo methods for the generation of amorphous thin film morphologies. These systems are analyzed using quantum mechanical methods in order to extract electronic properties relevant for charge transport. In the last step, the master equation of charge transport in the amorphous system is solved using an analytical effective medium approach. These simulation and modeling approaches have been developed by many researchers over the course of several years. Of special relevance is the work on atomistic morphology generation [12, 13] as well as the development of the generalized effective medium model [14]. Subject of this work is the development of a method for quantum mechanical analysis of large disordered molecular systems. For this purpose, I developed the Quantum Patch method, which evaluates the electronic structure of polaronic states in amorphous molecular systems incorporating polarization and other environment effects. This enables the calculation of energy disorder on a fully quantum mechanical basis. I will discuss existing methods and basic principles in Chapter 2, while the methods developed and improved in this work are introduced in Chapter 3.

I will present results of the application of the multiscale simulation approach on scientifically and technologically relevant systems in Chapter 4. I verify the validity of this approach by comparison with experimental data in Chapter 4.3 and Chapter 4.4. In Chapter 4.5, I use the multiscale method to gain insight into the molecular origin of charge transport properties of different materials. Furthermore, I use the simulation methods to elucidate the origin and influence of various correlations on charge transport properties. Examples are spatial correlations of energy levels due to long-range electrostatic interaction and local correlations between electron and hole energies influencing exciton transport. These correlations are discussed in more detail in Chapter 4.5.

So far, the method was only applied and validated using known materials. One of the main goals of material modeling is the systematic modification and improvement of material properties which directly influence device efficiency. Thus, I demonstrate the predictive power of the multiscale approach by applying it to novel materials (Chapter 4.6). For that, I combined the insight gained in understanding the relations between molecular properties and charge carrier mobility to systematically improve the electron mobility of a specific material, namely Alq_3. Several promising derivatives of this material were identified and are presented in

Chapter 4.6. The most promising of them shows an increase in electron mobility of more than two orders of magnitude. This theoretical prediction was experimentally verified and confirmed by synthesis and electronic characterization of the material. The experimental measurements and a comparison to theory are presented in Chapter 4.6.3.

I applied the multiscale workflow to several other material systems and applications. For the sake of brevity, not all of them are presented in detail in this work. Examples are the analysis of doped systems [15], spatially correlated systems with a net orientation of molecules leading to the giant surface potential (GSP) effect [16]. Furthermore, I analyzed periodic systems with low energy disorder. In self-assembled molecular wires [17], charge mobility is determined by the electronic coupling between molecular units. Both on- and off-wire hopping processes contribute to charge transport. In self-assembled metal-organic frameworks (MOFs) [18] loaded with guest molecules, the superexchange effect presented in Chapter 3.3 [19] can play an important role. Furthermore, my analysis of correlations in disordered organic systems contributed to the development of analytical methods which require molecule specific input such as energy disorder and correlation strength [20, 21]. As a last example, I discuss the influence of morphology on charge transport properties of binary bulk heterojunctions. Here, the formation of material domains on the mesoscale and disorder effects at grain-boundaries on the nanoscale play an important role in the performance of a solar cell. I show that annealing of the bulk heterojunction can increase the domain purity. This increases the exciton diffusion length as well as charge carrier mobility which finally leads to an improved efficiency of the solar cell.

One key result of this work is the introduction and analysis of a multiscale modeling approach which quantitatively predicts charge transport properties of a wide range of ordered and disordered molecular materials. The approach furthermore provides insight into relations between molecular properties and macroscopic charge transport characteristics which go well beyond the possibilities of existing methods. This insight on the one hand helps to understand details of the charge transport process even beyond the limit of experimental accessibility. On the other hand, the approach enables targeted improvement of material properties in form of rational *in-silico* material design, as shown by the three orders of magnitude increase in electron mobility of Alq_3.

2

Theory of organic electronics - fundamental principles and theoretical methods

The aim of this chapter is to give a brief overview over the fundamental principles of organic electronics and its applications, *e.g.* organic light emitting diodes (OLED) and organic solar cells (OSC). In addition to that, existing theories and methods required for description of charge transport in organic materials will be introduced. For the sake of brevity, this introduction will solely cover the concepts required for the methods development and application presented in Chapter 3 and 4. References to more exhaustive discussions in literature will be given in the text.

The first part of this Chapter (Section 2.1) briefly introduces the basic principles of organic semiconductors and organic electronics. The working principle of organic light emitting diodes and organic photovoltaics (OPV) will be outlined in Sections 2.1.3 and 2.1.2. Theoretical models of the charge transport mechanism in amorphous organic systems help to understand and systematically improve the materials used for organic electronics devices. Examples of these models for charge transport in disordered systems will be presented in Section 2.1.4. Here, transport of localized charge carriers in disordered systems will be discussed. Main emphasis is the Marcus theory and the concept of energy disorder in amorphous organic systems which is the main determinant of charge mobility in disordered systems. Furthermore, the connection between microscopic hopping rates and macroscopic properties like the charge carrier mobility is introduced in Section 2.2.3. Within this context, the generalized effective-medium model (GEMM) is presented. The basic principles of Hartree-Fock theory (HF) and density functional theory (DFT)

are derived in Section 2.3. These theories were applied for the quantum mechanical calculation of the electronic structure of molecules in this work. Both methods require atomistically resolved structures of molecules and large molecular systems as input. These can be generated using the classical molecular dynamics (MD) and Monte Carlo (MC) methods presented in Section 2.4.

2.1 FUNDAMENTALS AND APPLICATIONS OF ORGANIC ELECTRONICS

The field of organic electronics has undergone a long development process starting with the discovery of semiconducting organic polymers. Today, applications of organic electronics range from cheap printable organic transistors for smart flexible labels over lightweight polymer solar cells to energy efficient OLED displays with high contrast ratios and fast reaction times. The basis and common feature of all applications are semiconducting organic materials. They are usually divided into two classes, namely polymers and small molecules. Their physical and electronic properties will be described in Section 2.1.1 followed by an introduction of the basic principles of OLEDs (Section 2.1.3) and OPV (Section 2.1.2).

2.1.1 ORGANIC SEMICONDUCTORS

Inorganic semiconductors can be described as materials with a Fermi level E_{F} located in an energy gap of density of states $D(E)$. The density of states depends on the band structure of the material which is closely related to the periodicity of the materials' crystal structure. Amorphous organic semiconductors on the other hand are different from their inorganic counterpart. The lack of long range periodicity leads to fundamentally different charge transport properties compared to periodic systems with delocalized states. This will be discussed in Section 2.1.4.

The origin of the semiconducting properties and the energy gap of organic molecules arises from the sp^2-hybridization of carbon atoms in aromatic systems. Three of the valence electrons of carbon contribute to three sp^2-hybridized σ-bonds while the fourth 2p$_{\mathrm{z}}$-orbital perpendicular to the plane of the σ-bonds hybridizes with the 2p$_{\mathrm{z}}$-orbitals of neighboring atoms to delocalized π-orbitals. Similar to inorganic crystals, the hybridization leads to the opening of a energy gap between occupied π- and unoccupied π^*-orbitals (see Fig. 2.1). These orbitals usually contribute to the highest occupied molecular orbital (HOMO) and the lowest unoccupied molecular orbital (LUMO). The π-π^* gap (HOMO-LUMO gap) depends on the size of the delocalized aromatic system. A single isolated benzene ring (6

aromatic carbon atoms) or even an ethylene molecule (only 2 carbon atoms, see Fig. 2.1) show HOMO-LUMO gaps of $6.8\,\mathrm{eV}^*$ and $7.8\,\mathrm{eV}^*$, making these materials insulators. The larger the π-conjugated system, the smaller becomes the energy gap (down to 2-3 eV and further). In the extreme case of infinite sp^2-hybridized carbon atoms in a graphene sheet, the energy gap completely closes to zero.
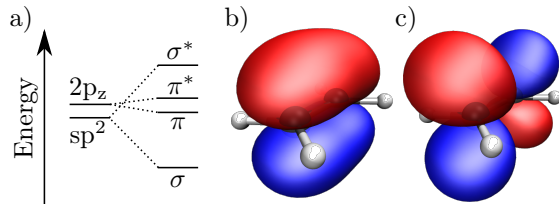
Figure 2.1: a) Atomic sp^2 and $2\mathrm{p_z}$ orbitals of the two carbon atoms of ethylene hybridize and form binding σ and π orbitals and anti-binding σ^* and π^* orbitals. b) HOMO orbital of ethylene. This occupied orbital is a symmetric linear combination of two atomic $2\mathrm{p_z}$ orbitals while the LUMO orbital shown in c) is an antisymmetric linear combination leading to an anti-bonding orbital

Typical molecules used in organic electronics applications usually consist of π-conjugated units connected to each other via single bonds. The size of the total conjugated system depends on the dihedral angle between planes of different conjugated units. In a simplified model, the conjugation over such a dihedral bond continues in case of parallel planes while in case of perpendicular planes, the states on both sides are decoupled. HOMO and LUMO orbitals do not necessarily belong to the same conjugated unit of a molecule. Furthermore, the electronic structure of the molecule can be modified using electron attracting or repelling functional groups and/or substitutions of carbon atoms with *e.g.* nitrogen. Aliphatic side groups such as linear or branched alkyl chains can increase the solubility of molecules in different solvents. Metal-organic complexes incorporating heavy transition metals and conjugated ligands are used in OLEDs to increase the spin-orbit coupling.

These and more possible modifications of conjugated molecules lead to a nearly infinite number of different molecules exhibiting different optical and electronic properties. This wide range and flexibility of potential materials is one of the major advantages of organic electronics compared to its inorganic counterpart. At the same time, it is one of its main drawbacks, as it makes systematic improvement of materials and devices difficult.

---

*The vales were obtained in DFT calculations using a B3LYP functional [22] and a def2-SV(P) basis set [23] as implemented in Turbomole [24].

Two possible applications of organic semiconductors will be given in the next two sections. In organic light emitting diodes, organic semiconductors are used for flexible, lightweight displays with high efficiencies, low energy consumption and at the same time high contrast ratios and fast reaction times. Two of the major drawbacks which remain to be solved are the stability and lifetime of OLEDs, especially of blue emitters, as well as the closely related applicability in large area devices such as television screens or lighting applications. Here, limits in stability and processability of the materials lead to spatial inhomogeneities of the OLED device. Flexible and lightweight organic solar cells on the other hand are currently a niche product in the photovoltaics sector. Large area solution processed OPV has shown to be possible but suffers from a low power conversion efficiency and low long-term stability. Efficiencies of over 10 % were reached under laboratory conditions while printed large area devices show efficiencies of only 3 %.

In both applications, improved materials with higher stability and better optoelectronic properties might lead to a better device performance and solve the issues mentioned above. Aim of this work is the systematic investigation of the relations between molecular structure and macroscopic properties. Comprehension of these relations makes systematic and targeted molecule design possible. One examples of this will be given in Chapter 4.6.

2.1.2 ORGANIC SOLAR CELLS

The light to energy conversion process of an organic solar cell (OSC) [25, 26] consists of several steps. Initially, photons are absorbed in a layer of organic semiconducting material. The excitons created in this process migrate in a diffusive process to a material interface where they are separated into pairs of electrons and holes (see Figure 2.2). These are then extracted via the electrodes on both sides of the active layer.

Unlike in inorganic semiconductors, the excitons are strongly bound with a binding energy larger than room temperature (RT). The exciton can only be separated at a material interface where either an electron or a hole is transferred from the absorbing donor material to the acceptor material. To maximize the donor-acceptor material interface, the active layer of a solar cell consists of a blend of two materials with different energy levels and absorption properties. These two materials are phase separated into a metastable, closely interconnected domain structure, called bulk heterojunction. One of the two material domains, in many cases a polymer, absorbs light in the visible spectrum while the other material, mainly fullerene derivatives, accepts electrons.
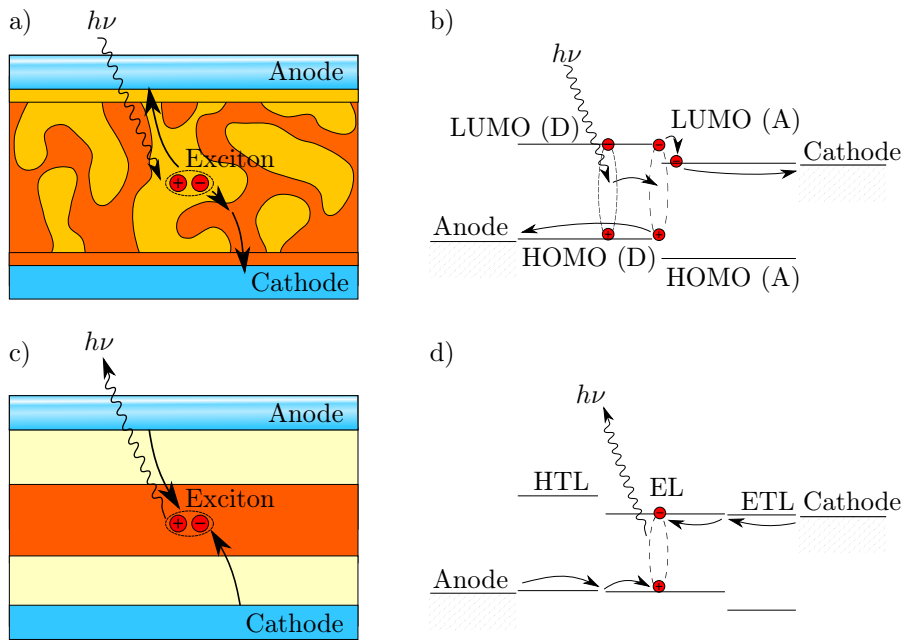
Figure 2.2: a) Schematic illustration of an organic solar cell. The active layer consists of a bulk heterojunction sandwiched between hole or electron transport layers and the electrodes. Photons are absorbed in the bulk heterojunction and separated at material interfaces. Electrons and holes leave the device via the electrodes and generate electric current. Panel b) shows the band diagram of the active layer and the electrodes of an organic solar cell. Panels c) and d) are the corresponding illustrations of an organic light emitting diode. The OLED consists of a multilayer architecture of different materials for charge injecting, recombination and light emission.

The diffusion process of the exciton is not directed and cannot be influenced by internal or external fields. To obtain high quantum efficiencies, all excitons have to reach a material interface within their material dependent diffusion length. The exciton diffusion length is limited by the exciton lifetime which again depends on molecular properties. Typical values of diffusion lengths of organic semiconductors are between $5\,\mathrm{nm}$ and $30\,\mathrm{nm}$, making relatively small material domains necessary. After exciton dissociation, the separated charges have to be extracted from the bulk heterojunction. This process requires closed paths of all material domains to the respective electrodes. The dependence of charge mobility on disorder makes larger domains desirable. A method for the simulation of material demixing and domain formation in organic solar cells will be introduced in Chapter 3.4. Results of this method are presented in Chapter 4.7.5.

The active layer of the solar cell is usually sandwiched between an electron transport and hole blocking layer (ETL) on the cathode side and a hole transport and electron blocking layer (HTL) on the anode side. The two blocking layers avoid shunts and make sure that each type of charge carrier can only reach its respective electrode. As mentioned above, most organic solar cells use polymers as absorber materials. The acceptor material is often a fullerene [27] derivate like $PC_{60}BM$. As thin films of organic polymers cannot be fabricated in a vapor deposition process, solution processing of at least the active layer becomes necessary. Solution processing methods in principle offer a potentially cheap and well scaling production technique known from established roll-to-roll printing processes. At the same time, processing conditions, material (im)purity and the influence of solvent materials in multilayer systems pose a challenge for the large-scale production of highly efficient devices. Vapor deposited organic solar cells on the other hand show higher efficiencies and better controllability of multilayer structures at a higher production cost. Vapor deposited solar cells are based on small molecule absorbers and fullerenes or other organic electron conductors as acceptor materials. Maximum power conversion efficiencies reached with organic solar cells are between $10\,\%$ and $12\,\%$ [28, 29].

There are multiple unsolved scientific questions in which theoretical approaches and modeling techniques can aid experiment and lead to a better understanding of materials and device characteristics. Examples are the search for ideal optical properties of the active material [30, 31], exciton separation at materials interfaces, charge transport and conductivity of amorphous materials, especially of polymers and demixing and domain formation in bulk heterojunctions. These open scientific questions and challenges leave room for material and device improvement

and make organic photovoltaics an ideal system for theoretical and modeling approaches.

2.1.3   ORGANIC LIGHT EMITTING DIODES

In organic light emitting diodes (OLEDs), similar processes as in organic solar cells occur in a reversed order. In an idealized picture, electrons are injected from the cathode through an electron transport layer into the active material. Holes are injected at the same time from the anode through a hole transport layer (see Figure 2.2c and 2.2d). In the active layer, electrons and holes meet and form bound exciton states which recombine after a certain time. Each radiative decay of an exciton produces a photon which is emitted by the OLED.

The active layer typically consists of a host material with a certain concentration of guest molecules with a smaller HOMO-LUMO gap compared to the host. Electrons, holes and excitons are trapped on molecules of the guest material reducing the chance of non-radiative decay processes due to exciton-polaron quenching and triplet-triplet annihilation. The concentration of guest molecules is decisive for charge transport properties and the efficiency of the OLED [19].

Due to spin-statistics, 75 % of the generated excitons are in a triplet state and only 25 % are singlets. Due to low spin-orbit coupling in light elements such as carbon, oxygen, nitrogen and hydrogen, the triplet excitons have comparably long lifetimes. This increases chance of interaction with polarons which leads to non-radiative decay or even detrimental excitations which might destroy molecules and therefore induces aging effects. Two approaches to efficiently harvest triplet excitons and reduce the lifetime of triplet excitons are discussed in literature. In the first approach, emitter molecules are used which include heavy (transition) metals, *e.g.* Iridium complexes like Tris[2-phenylpyridinato-C^2,N]iridium(III) (Ir(ppy)$_3$). These molecules exhibit low triplet lifetimes and efficient singlet-to-triplet conversion rates (intersystem crossing) [32–34]. A second approach for triple harvesting is based on molecules in which the energy difference between the triplet state and the single state is smaller than the thermal energy at room temperature. In most molecules, the singlet state is several hundred meV higher in energy than the triplet state. By targeted molecule design, it is possible to decrease this gap and enable a thermally activated conversion of triplet states into singlet states with rather high conversion rates. In the singlet state, the excitons radiatively de-excite in a fluorescent process. This process is called thermally activated delayed fluorescence (TADF) [35–38]. As an alternative to the TADF process, triplet excitons can be harvested using excimer [39, 40] or exciplex [41–44] states using bound electron-hole states delocalized over two equal or different molecules. Here,

an internal quantum efficiency of 100 % can be reached. At the same time, the emission spectrum is broader compared to exciton-decay on single molecules.

Open scientific questions in OLEDs range from charge mobility and conductivity over optoelectronic properties and long-term stability of host and emitter molecules to anisotropy effects which can be used to improve photon outcoupling and device efficiency [45, 46]. Most of them are strongly related to the improvement of material properties. Investigation of structure-property relations between molecules and desired macroscopic device characteristics help to find design rules for targeted improvement of materials. This challenge can be tackled using appropriate multiscale methods which cover the entire length scale from single molecules to device characteristics. These methods allow for detailed *in silico* analysis of amorphous organic systems and therefore guide experiments on their way to more efficient OLED devices.

2.1.4 TRANSPORT OF LOCALIZED CHARGE CARRIERS IN DISORDERED SYSTEMS

A common characteristic of almost all organic materials used in OLEDs and OSCs is their amorphous structure. This structure leads to fundamentally different charge transport properties compared to crystalline materials. In materials with a periodic structure, the electronic wave function follows the periodicity of the crystal structure and charge transport can in a simplest approximation be described as the propagation of delocalized waves or quasi particles.

In disordered organic semiconductors consisting of *e.g.* small molecules, energy disorder, weak intermolecular couplings and reorganization of the molecular structure upon charging prevents hybridization between the electronic states of different molecules. This leads to the localization of the wave functions of charge carriers (positive and negative polarons) on single molecules (see Figure 2.3c). Charge transport mainly occurs in form of tunneling or hopping processes of charge carriers between different π-conjugated fragments (molecules) of the system. This mechanism is called hopping transport. Methods to theoretically describe and quantify hopping transport will be introduced in the next sections.
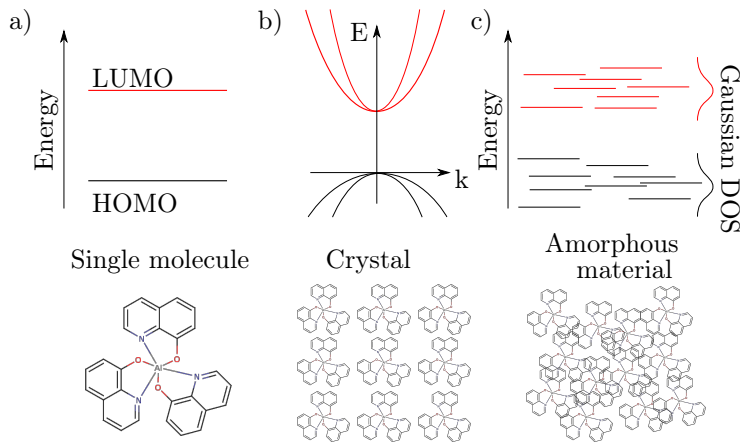
Figure 2.3: a) Single molecules in vacuum have clearly defined energy levels. b) Interaction of molecules in periodic crystals leads to delocalization of states and to the formation of bands in reciprocal space. c) In disordered systems, each molecule retains its individual energy levels. Intermolecular, mainly electrostatic interaction and deformation of the molecules in the amorphous structure shifts the energy levels of each single molecule. This leads to a (almost Gaussian) density of states of each molecular energy level, in particular of HOMO and LUMO energies.

2.2 MODELING OF HOPPING TRANSPORT IN DISORDERED SYSTEMS

Hopping transport can be quantitatively described in various ways. Two modeling approaches, namely master equation approaches (ME) and kinetic Monte Carlo simulations (KMC), describe the amorphous system in a coarse grained way. The molecular system is mapped on a graph consisting of sites representing molecules and connections representing hopping possibilities. In the simplest case, the site distribution can be approximated as a cubic lattice. In more advanced approaches [47], a distribution of points is used, which follows the same neighbor distance characteristics as the center of mass positions of the disordered molecules in the condensed phase.

The master equation describes the time derivative of the occupation probability $p_i(t)$ of a certain site i as the sum of all fluxes in and out of this site.

$$\frac{\mathrm{d}p_i(t)}{\mathrm{d}t} = \sum_j (p_j(t)k_{ji} - p_i(t)k_{ij}) \tag{2.1}$$

The terms on the right side of the equation describe the probability flux $\sum_j p_j(t)k_{ji}$ from neighboring sites j to site i and the probability flux $\sum_j p_i(t)k_{ij}$

away from site i to its neighboring sites j. k_{ij} denotes the hopping rate from site i to site j. In a steady state, the time derivative of p_i becomes zero and quantities such as charge carrier mobility can be obtained. The master equation can be solved either analytically or numerically.

In kinetic Monte Carlo approaches [48–50], all hopping processes occurring during charge transport are explicitly modeled. A certain number of electrons is distributed in the system. In each Monte Carlo step, the rates k of all possible hopping processes are calculated and one rate is chosen with a probability corresponding to its contribution to the sum of all rates $K = \sum k$. The chosen step is carried out and the time is updated with a time step $\delta t = K^{-1}\ln(1/x')$, with x' being a random number between 0 and 1. In this way, a random but representative trajectory of the system is obtained, which obeys thermodynamic laws. From this trajectory, the equilibrium charge density and charge mobility as well as percolation paths can be extracted. A extension of this method will be presented in Symalla *et al.* [19].

Both master equation approaches and KMC simulations require hopping rates. In many examples in literature [51–53], the Miller-Abrahams rate [54] was used, which depends on the energy difference ΔE_{if} between the initial and the final state, the hopping distance r_{if} and a parameter α which can be interpreted as the inverse wave function decay length.

$$k_{\mathrm{if}} = k_0 \exp(-2\alpha r_{\mathrm{if}}) \begin{cases} \exp(-\Delta E_{\mathrm{if}}/(k_{\mathrm{B}}T)) & \text{if } \Delta E_{\mathrm{if}} > 0 \\ 1 & \text{else} \end{cases} \qquad (2.2)$$

This equation can be derived from a stationary solution of the master equation [54]. Due to the phenomenological distance dependence and the neglect of molecular reorganization, the Miller-Abrahams equation does not fully capture all relevant quantum mechanical effects of hopping transport. A more detailed description of the hopping rate is provided by Marcus theory [55, 56], which was primarily developed for donor-acceptor complexes to quantify the rates of charge transfer processes. Its details will be explained in the next section.

2.2.1 Marcus theory

Rudolph A. Marcus developed a theory for the quantitative description of redox reaction rates involving electron transfer processes between reactants in solution. This theory can also be applied to describe charge transfer processes of localized states in organic semiconductors.
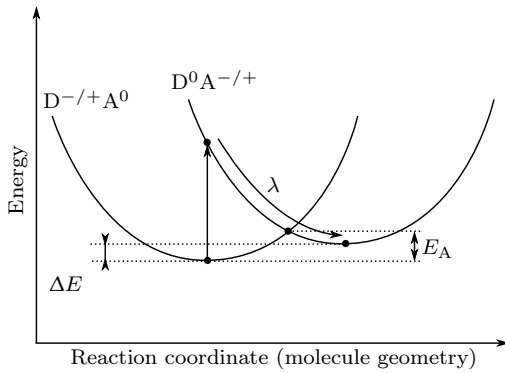
Figure 2.4: Marcus parabolas representing the total system in the states where the donor is charged (left, $D^{-/+}A^0$) and the acceptor is charged (right, $D^0A^{-/+}$) The activation energy E_A can be calculated using the energy difference ΔE and the reorganization energy λ (see Eq. 2.3).

The calculation of the Marcus hopping rate for a charge transfer between two molecules requires three microscopic parameters. The prefactor of the Marcus rate depends on the square of the electronic coupling $|J_{if}|^2$ between the localized molecular states before (initial) and after (final) the charge transfer process. The exponential function depends on the energy barrier or activation energy E_A between the two states. Marcus theory uses a parabolic approximation of the Gibbs free energy $G(\vec{q})$ of the system as a function of the multidimensional reaction coordinate $\vec{q}$. The frozen molecular orientation in condensed amorphous system makes entropic effects negligible [57]. Thus, the Gibbs free energy can be approximated as the total energy of the system.

The parabolic dependence of the total energy $E(\vec{q})$ on $\vec{q}$ leads to an activation energy E_A which depends on the difference in total energy ΔE between the initial and final state and the reorganization energy λ of the charge transfer process.

$$E_A = \frac{1}{4\lambda}(\lambda + \Delta E)^2 \ . \tag{2.3}$$

This activation energy can be calculated as the intersection of the two Marcus parabola shown in Fig. 2.4. Combining the full prefactor with an exponential function of the activation energy according to the Arrhenius equation [58, 59] leads to the full Marcus hopping rate [55, 56].

$$k = \frac{2\pi}{\hbar}\left|J\right|^2 \frac{1}{\sqrt{4\pi\lambda k_B T}} \exp\left(-\frac{(\lambda + \Delta E)^2}{4\lambda k_B T}\right) \tag{2.4}$$

There are two assumptions which have to be fulfilled in order to make Marcus theory applicable [60]. The first assumption is the localization of charge carri-

15

ers to clearly defined hopping sites, which is called the localized polaron model. It is fulfilled if the hopping sites have only weak electronic coupling elements compared to their reorganization energy. In disordered small molecule systems, this assumption is fulfilled as typical reorganization energies are in the order of $100 - 500\,\mathrm{meV}$ and the largest electronic couplings usually do not exceed $10\,\mathrm{meV}$ (see also Chapter 4.4). The second condition for Marcus theory is related to the phonon mediated and therefore temperature activated nature of the hopping process. Marcus theory is applicable in a high temperature regime where the thermal energy $k_\mathrm{B}T$ is large compared to the energies of the vibronic states $\hbar\omega$ responsible for the reorganization of molecules upon charging. These vibrational states can therefore be treated as a continuum of states including all states required for the charge transfer reaction.

In the following sections, details about the calculation of the molecule and system dependent parameters J, λ and ΔE required for the Marcus rate will be given.

ELECTRONIC COUPLING

The electronic coupling between two states can be calculated using the Löwdin orthogonalization method [61, 62]. Here, the highest occupied molecular orbital (HOMO) is assumed to represent the wave function of an additional hole (missing electron) whereas the lowest unoccupied molecular orbital (LUMO) represents the electron wave function.

$$J_\mathrm{if} = \frac{F_\mathrm{if} - \frac{1}{2}(F_\mathrm{ii} + F_\mathrm{ff})S_\mathrm{if}}{1 - S_\mathrm{if}^2} \tag{2.5}$$

The matrix elements $F_\mathrm{if} = \langle\mathrm{i}|\,F_\mathrm{dimer}\,|\mathrm{f}\rangle$ and $S_\mathrm{if} = \langle\mathrm{i}|\,S_\mathrm{dimer}\,|\mathrm{f}\rangle$ are calculated using the Fock and overlap matrices of a molecular dimer system. The states $|\mathrm{i}\rangle$ and $|\mathrm{f}\rangle$ are the highest occupied molecular orbital (for $J_\mathrm{if,HOMO}$) or the lowest unoccupied molecular orbital (for $J_\mathrm{if,LUMO}$) of the single molecule i (f), expanded to the dimer-basis. Extensions of this method were developed in the work of Paul Kleine [63]. These explicitly consider additional charges and polarization effects. In addition, the electronic coupling between more complicated states like excitations can be calculated with this method.

ENERGY DIFFERENCES

As mentioned above, one of the decisive quantities for the Marcus hopping rate is the total energy difference between the initial and the final state. This energy

difference mainly depends on the individual conformations and environments of the two molecules involved in the hopping process. Disorder effects will be discussed in detail in Chapter 2.2.2 and 4.5. If the hopping takes place in an external electric field $\vec{F}$, the energy difference ΔE has an intrinsic contribution ΔE_{int} and a contribution due to the external electric field $\vec{F}_{\mathrm{ext}}$. This external contribution can be written as

$$\Delta E_{\mathrm{ext}} = \int_V \Phi(\vec{r})_{\mathrm{ext}} \left(n_{\mathrm{f}}(\vec{r}) - n_{\mathrm{i}}(\vec{r}) \right) \mathrm{d}\vec{r}^3 \ , \tag{2.6}$$

where the external potential Φ is defined by the field as

$$-\nabla\Phi(\vec{r})_{\mathrm{ext}} = \vec{F}_{\mathrm{ext}} \ . \tag{2.7}$$

$n_{\mathrm{i/f}}(\vec{r})$ are the total charge densities before and after the hopping process. In a coarse grained site-based models, the external contribution ΔE_{ext} can be approximated as $\Delta E_{\mathrm{ext}} = e(\vec{F}_{\mathrm{ext}} \cdot \vec{r}_{\mathrm{if}})$, where $\vec{r}_{\mathrm{if}} = \vec{r}_{\mathrm{f}} - \vec{r}_{\mathrm{i}}$ is the vector connecting the two hopping sites. These sites can be approximated as the center of charge of polarons localized on the initial and the final molecule. In many cases, the center of mass or center of geometry of the molecules are used.

The intrinsic contribution ΔE_{int} arises from the disordered geometry of the amorphous system. The two main sources of disorder are electrostatic interactions between the molecules and distortions of the molecular geometry due to intra- and inter-molecular forces acting on the molecules. More details will be given in Chapter 2.2.2.

REORGANIZATION ENERGY

When in the semi-classical Marcus picture an electron is transferred from one molecule to another, thermal fluctuations and vibrations lead to states of the molecular system, in which transitions of electrons between molecules become possible. The energy barrier of this transition state is given in Eq. 2.3. It involves the energy difference ΔE_{if} between initial and final states as well as the reorganization energy λ_{if} of the system. This reorganization energy is strongly related to the different time scales on which electronic and ionic processes are occurring, a principle which is also used in the Born-Oppenheimer approximation (see Section 2.3).

For the calculation of the reorganization energy, the charge transfer is partitioned into a sequence of processes which decouple the fast electronic processes from the much slower ionic responses of the system. This procedure is called Nelsen's four-point-procedure [64] and can be described using the following steps

(see Fig. 2.5). Prior to the hopping process, the system is in its electronic and ionic ground state where the charged donor molecule is relaxed in its charged ionic state and the acceptor is in its neutral ionic state (E_i in Fig. 2.5a). A charge transfer between the two molecules including the electronic response but without changing the geometry of the system is represented by a vertical excitation of the system from the first to the second parabola (E_i^*). This vertical charge transfer is followed by the ionic relaxation of the system after which the charged acceptor molecule reaches its charged-state geometry and the donor relaxes into its neutral-state geometry (E_f). The energy difference between E_i^* and E_f is the reorganization energy λ.

The reorganization energy is usually separated into an inner part λ_{inner} including relaxation of the donor and the acceptor molecule and an outer part λ_{outer} including the relaxation of the environment. In condensed molecular systems, the outer part is assumed to be much smaller than the inner part because the additional charge will cause much stronger conformational changes to the charged molecule than to molecules in its environment. Thus, the outer part of the reorganization energy was neglected in this work. If the charge transfer is taking place in dilute systems, *e.g.* in liquid or gas-phase, the reaction of the surrounding molecules cannot be neglected. To account for this effect, methods were developed to estimate the outer part of the reorganization energy using electrostatic calculations [65], polarizable force fields [66] and hybrid methods combining quantum mechanical calculations with molecular dynamics calculations [67].

The calculation of the inner part of the reorganization energy is illustrated in Fig. 2.5b. Acceptor and donor molecules are treated separately. The electronic and ionic ground state of the neutral acceptor molecule is calculated (E_1). A charge is added to the molecule and an ionic relaxation is performed ($E_2 \rightarrow E_3$). This yields the acceptor part of the inner reorganization energy ($\lambda_{i,acceptor} = E_2 - E_3$). The opposite process happens on the donor molecule. Here, the electronically and ionically relaxed ground state of the charged donor molecule is calculated (E_1'). The charge is removed from the donor molecule and it relaxes ($E_2' \rightarrow E_3'$). The energy difference $E_2' - E_3'$ is the donor part $\lambda_{i,donor}$ of the reorganization energy associated with the charge transfer process. Summation of acceptor and donor part yields the inner part of the reorganization energy:

$$\lambda_{inner} = (E_2 - E_3) \ + \ (E_2' - E_3') \ . \tag{2.8}$$

In general, the acceptor and donor can be different types of molecules and each of them is embedded into its individual and unique environment in the amorphous morphology. Therefore, the reorganization energy λ will be different for each pair of
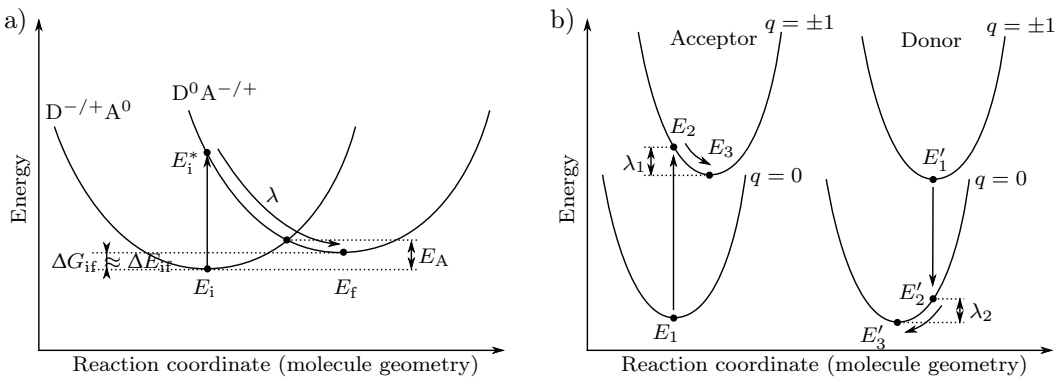
Figure 2.5: a) Marcus parabolas representing the total system in the states where the donor is charged (left, $D^{-/+}A^0$) and the acceptor is charged (right, $D^0A^{-/+}$) b) Illustration of the two Nelsen four-point-procedure (see text) to calculate the inner part λ_i of the reorganization energy. This inner part is split into two contributions coming from relaxation of the acceptor and donor molecule, respectively.

hopping sites in the system. Simulations of hopping transport as found in literature take only the inner part of the vacuum reorganization energy of each molecule into account. In this work, extensions of this will be discussed and tested. Here, a confinement of the molecules in their local environment is used to limit their degrees of freedom for ionic relaxation (methods are explained in Chapter 3.1.3 and results are shown in Chapter 4.4). This method can in general be extended to also explicitly calculate the order of magnitude of λ_{outer}.

2.2.2 ENERGY DISORDER

This section will give an introduction into methods for the definition and calculation of energy disorder which is in many disordered materials the main and limiting contribution of Marcus rates and charge carrier mobility. In this work, the Quantum Patch method will be used to quantitatively calculate the energy disorder of amorphous systems. It is based on a self-consistent evaluation of site energies using quantum mechanical DFT calculations [68]. The Quantum Patch method was developed in my master's thesis [69] and extended in this work. It will be presented in detail in Chapter 3.2.

DEFINITION OF ENERGY DISORDER

The density of states (DOS) in disordered organic systems is assumed to approximately follow a Gaussian distribution [14, 52, 53, 70–72]. Spatial correlations arising from electrostatic interaction of molecules exist to a certain extend in many systems and lead to deviations from Gaussian disorder [73–75]. In some materials,

experiments show deviations from a Gaussian shape in the tails of the density of states arising from different effects such as traps and interface states [76–78]. Despite these effects, the main determinant of charge mobility is the width of the (Gaussian) density of states, called energy disorder σ. Several different formal definitions exists for this quantity. If site energies in a molecular system are uncorrelated with respect to their position and distance, the resulting density of states can be characterized as the standard deviation σ of the site energy distribution. A Gaussian distribution of N_{sites} energies E_i with mean energy $\langle E_i \rangle$ has a standard deviation of

$$\sigma(E) = \sqrt{\frac{1}{N_{\text{sites}} - 1} \sum_i (E_i - \langle E_i \rangle)^2} \ . \tag{2.9}$$

In case there exist (long-range) correlations between the site energies which arise from *e.g.* dipole induced disorder, there is a difference in local and global energy disorder σ. This effect can be quantified by calculating the distribution width of site energy differences $\sigma(\Delta E_{ij})$ for molecular pairs below a certain distance threshold $d_{ij} \leq d_{\text{max}}$:

$$\sigma(\Delta E) = \sqrt{\frac{1}{2N_{\text{pairs}} - 2} \sum_{i,j \neq i} \Delta E_{ij}^2} \ . \tag{2.10}$$

Double counting of all pairs i, j makes $\langle \Delta E_{ij} \rangle = 0$ and leads to the factor 2 in the denominator. If the site energies E_i are Gaussian distributed and there are no (spatial) correlations between them, it can be shown that the relation between $\sigma(E)$ and $\sigma(\Delta E)$ is

$$\sigma(\Delta E) = \sqrt{2} \ \sigma(E) \ . \tag{2.11}$$

Spatial correlations usually lead to a decrease in local disorder: $\sigma(\Delta E) \leq \sqrt{2} \ \sigma(E)$ (see Appendix F) The reason for this is that sites which are close to each other feel a similar long-range electrostatic field of the surrounding bulk material. Thus, energy differences between sites with low distances d_{ij} in a correlated system are on average smaller than energy differences between arbitrary pairs of molecules in the system. As electronic coupling elements decay exponentially with increasing intermolecular distance, hopping transport is a rather local process. Therefore, the local energy disorder $\sigma_{\text{loc}} = \sigma(\Delta E)\sqrt{2}$ is decisive for the calculation and prediction of charge carrier mobility.

STRUCTURAL DISORDER AND ELECTROSTATIC DISORDER

In a crystalline system with a given number of molecules per unit-cell N_0, there

exists a finite number (N_0) of site energies. Disorder only arises due to thermal broadening of the energy levels which is caused by molecular vibrations. Apart from that, all molecules which are equivalent with respect to their position within the unit cell have the same molecular conformation and feel the same electrostatic potential. Depending on the ratio of electronic couplings and reorganization energy, charge transport occurs in form of hopping of localized polarons or by a dispersive transport due to intermolecular hybridization leading to delocalized states and band formation.

Energy disorder in amorphous materials arises from two different effects. On source are intermolecular forces in amorphous structures that bend and deform molecules. Weak intramolecular degrees of freedom like the rotation of dihedral angles can be influenced by this effect. As shown in Chapter 4.5, this does not necessarily influence charge transport in the system. Energy disorder for electrons and holes only arises from changes in the on-site energy which can be calculated in terms of ionization potential (IP) and electron affinity (EA) of the molecules. IP and EA can be approximated with more easily accessible HOMO and LUMO energies. The conformational disorder can then be estimated using the range of HOMO and LUMO energies as a function of the intramolecular degrees of freedom or vibrational modes around their minima in the equilibrium conformation of the molecule. This procedure is presented in Chapter 4.5.

The second source of energy disorder are intermolecular interactions. Each molecule is embedded into its individual environment created by all other molecules. The interaction energy consists of contributions from Pauli repulsion, van der Waals' interaction and electrostatic interaction. The strongest contribution of this energy is the long range of Coulomb interaction between charges and the dipole moments of surrounding molecules. The additional charges furthermore polarize their environment which feeds back on the site energies of the respective polarons and the energy disorder. This polarization effect due to additional charges is implicitly taken into account in the self-consistent Quantum Patch method presented in Chapter 3.2.1.

Calculation of energy disorder

To calculate the conformational and electrostatic contributions of energy disorder, atomistically resolved morphologies are required. This section will introduce various established ways to estimate or explicitly calculate the energy disorder of an amorphous molecular system. In this work, the Quantum Patch method (see

Table 2.1: Values of the energy disorder of Alq$_3$ based on Eq. 2.12. Different assumptions from literature about the dipole moment, the dielectric constant and molecular density of Alq$_3$ were used for the two values.

Dipole moment $|\vec{d}|$ [Debye]	Lattice constant a [Å]	Relative permittivity ε	Energy disorder $\sigma(E)$ [eV]	Source
5.5	9.9	3.0	0.15	[79]
4.9	8.3	3.5	0.13	[80]

Chapter 3.2) will be used for the calculation of energy disorder.

One very basic approach for the calculation of energy disorder caused by electrostatic effects is described in Young *et al.* [72]. Here, an analytic expression for the energy disorder in a system of arbitrary directed dipoles on a cubic lattice with lattice constant a is derived:

$$\sigma(E) = \frac{2.35|\vec{d}|e}{4\pi\varepsilon_0\varepsilon a^2} \tag{2.12}$$

In this equation, $\vec{d}$ is the dipole moment of the molecules, $-e$ is the charge of an electron, ε is the relative permittivity of the amorphous material and ε_0 is the vacuum permittivity. The energy disorder of Alq$_3$ (see Fig. 4.1) derived with this formula is shown in Tab. 2.1.

The dipole model can only serve as a rough estimate of energy disorder and strongly depends on the reliability of the input parameters *i.e.* the dipole moment and the dielectric constant. Its applicability for a detailed analysis of different systems is limited. For a more accurate calculation of the energy disorder, the influence of conformational disorder as well as of a more realistic representation of the electrostatic interaction have to be taken into account. These two requirements lead to practical problems: Calculation of conformation and polarization effects on a quantum mechanical level can in principle be achieved in a single evaluation of the electronic structure of the entire system. Due to cubic scaling of the computational cost of *e.g.* DFT calculations with the number of electrons in the system, the evaluation of systems with more than a few molecules becomes unfeasible. Furthermore, these calculations will only predict the ground state of the total system. An additional charge will not be confined to the molecule of interest but rather be localized on the energetically lowest hopping site. This makes

it impossible to straightforwardly evaluate the full density of states of a system.

In literature, two general approaches to this problem are proposed. The first one takes all molecules of the environment explicitly into account and at the same time confines the additional charge to the required hopping site via an additional external potential. This method is called constrained density functional theory (cDFT) [81–84]. It describes polarization effects on a fully quantum mechanical level. Major disadvantage of this method is the computational effort which scales at least with $\mathcal{O}(N_{\mathrm{electrons}}^3)$, making the method unfeasible for realistic system sizes.

Another class of approaches treats only the charged molecule on a quantum mechanical level while including interaction effects with the environment in a classical way via static or polarizable point charges. Examples are polarizable continuum models (PCM) [85], polarizable force field methods [57, 86] like the AMOEBA method [87–89] as well as QM/MM [90–92] approaches. In QM/MM approaches, the molecular system is divided into a quantum mechanical region (QM) and one or more surrounding shells which are treated in a classical (molecular mechanics, MM) way. In these shells, force field based methods are used in a way similar to molecular dynamics simulations (see Chapter 2.4.1). Disadvantages of these methods are the loss of accuracy in the outer shells as well as the need for parameterization of $e.g.$ the molecular polarizability tensor and its mapping on polarizable point charges. Force field parametrization can be obtained using theoretical methods or obtained phenomenologically by tuning the force field parameters in order to reproduce experimental results for known materials. The mapping of not necessarily linear quantum mechanical polarization effects of different molecular orbitals to mostly linear polarizable force fields does not necessarily cover all relevant effects.

Therefore, a more reliable and predictive model based on *ab initio* methods is required for the calculation and prediction of energy disorder in yet unknown systems. Such a method was developed in my Master's thesis [69] and extended in this work. It will be presented in Chapter 3.2.

2.2.3 Charge carrier mobility and conductivity

One connection between microscopic quantities like electronic couplings or molecular reorganization energies and the macroscopic measurable conductivity σ is the mobility μ. The conductivity is defined using the Ohm's law

$$\vec{j} = \sigma \, \vec{F}_{\mathrm{ext}} \tag{2.13}$$

with current density $\vec{j}$ and external electric field $\vec{F}_{\text{ext}}$. Taking into account that the current is proportional to the charge carrier density n, one obtains

$$\vec{j} = n\,e\,\mu\,\vec{F} \tag{2.14}$$

with $\sigma = n\,e\,\mu$. In general, the mobility μ itself is a function of the charge carrier density n, the temperature T and the electric field $F = |\vec{F}_{\text{ext}}|$:

$$\mu = \mu(n, T, F) \ . \tag{2.15}$$

In disordered semiconductors, Poole-Frenkel behavior [93] is observed. Here, the current density is proportional to $F \exp\left(\sqrt{\beta_{\text{PF}}F}\right)$, leading to a charge carrier mobility of the form:

$$\mu(n, T, F) = \mu_0(n, T) \exp\left(\sqrt{\beta_{\text{PF}}F}\right) \ . \tag{2.16}$$

The zero-field mobility μ_0 is obtained from extrapolation of the experimental field-dependent charge carrier mobility $\mu(\vec{F})$ to $F = 0$. β_{PF} is a factor depending on material properties. According to Hall *et al.* [94], this constant is $\beta_{\text{PF}} = e^3/(4\pi\varepsilon\varepsilon_0 k_{\text{B}}T)$ with permittivity $\varepsilon\varepsilon_0$, electron charge $-e$ and temperature T. In theoretical approaches, the charge carrier mobility can be obtained from numerical or approximative analytical solutions of the master equation.

ANALYTIC MODELS

Several analytic models to determine charge carrier mobility were developed over the past decades, starting with the work of Bässler *et al.* [52, 53]. These models were tested and refined by many other groups [51, 95, 96]. Nonetheless, most of the models depend on parameters which cannot be directly connected to molecular properties. Examples are the wave function decay length similar to the parameter α in the Miller-Abrahams rate (Eq. 2.2) or a correlation strength determining the extend of spatial correlations in the site energies. Main reason for the introduction of these parameters is that microscopic properties were simply neither measurable nor computationally accessible. Growing computer power throughout the recent years made quantum mechanical calculations of large systems possible. This enables to close the gap between microscopic molecular properties and macroscopic thin film properties such as charge mobility.

One parameter-free model effective medium model to estimate an upper bound for the charge carrier mobility of disordered systems is presented in the next section. It is used in this work to estimate and analyze charge carrier mobility of different organic materials.

Generalized effective-medium model (GEMM)

The generalized mean effective-medium model (GEMM) [14] to estimate charge carrier mobility was developed in a cooperation between AG Wenzel at KIT and the Materials Science Laboratory (MSL) of Sony, Stuttgart. This approach estimates the charge carrier mobility by approximately solving the master equation. It assumes a Gaussian density of states and averages over all possible Marcus hopping rates in the system. As an effective medium approach, it neglects percolation effects [97, 98]. Thus, it yields an upper bound for the charge mobility in disordered systems.

The mobility in this generalized mean effective medium (GEMM) model is a function of averaged microscopic parameters *e.g.* electronic couplings and the width of the density of states.

$$\mu = \frac{e\sqrt{\pi}\beta^2}{6\hbar} \frac{1}{\sqrt{\beta\left(\frac{\lambda}{4} + \frac{\beta\sigma^2}{4}\right)}} M \left\langle J^2 r^2 \right\rangle \exp\left[-\beta\left(\frac{\lambda}{4} + \frac{\beta\sigma^2}{4}\right)\right] \qquad (2.17)$$

The parameters in this formula are the inverse temperature $\beta = (k_B T)^{-1}$, the local energy disorder $\sigma = \sqrt{1/(2N_{\text{pairs}} - 2)\sum_{i,j\neq i}\Delta E_{ij}^2}$, the mean number of hopping possibilities $M = 2N_{\text{pairs}}/N_{\text{sites}}$ for each charge carrier and the averaged electronic couplings $\left\langle J^2 r^2 \right\rangle = 1/(2N_{\text{pairs}})\sum_{i,j\neq i}(J_{ij}^2 r_{ij}^2)$. Eq. 2.17 is used in Chapter 4 to estimate the charge carrier mobility or organic materials.

The dependence of the Marcus rate (Eq. 2.4) on the energy difference leads to an exponential dependence of the mobility on the energy disorder σ of the material, *i.e.* $\mu \propto \exp(-C\beta^2\sigma^2)$. The C-factor which in many other models describes the strength of percolation effects is $1/4$ in the effective medium limit. Models which incorporate percolation effects [52, 70, 95–97, 99, 100] use C-factors derived from experimental observations of the temperature and field dependence of the charge mobility or from fits to appropriate numerical methods such as kinetic Monte Carlo approaches. The C-dependence of the charge carrier mobility for different materials is discussed in Chapter 4.4.

Numerical methods

Apart from approximative analytic models, charge transport can also be explicitly simulated in kinetic Monte Carlo simulations. Analytic models for the calculation of charge mobility are in many cases restricted to relatively simple systems such as

single-layer devices consisting of only one material. Kinetic Monte Carlo models on the other hand can have a much higher complexity. This ranges from single carrier type and single layer simulations as described by the analytic models to device simulations of organic solar cells or OLEDs including positive and negative polarons, excitons and all interactions and processes related to these quasi-particles. Simulations of that kind will be described in the Master's thesis of Jana Holland-Cunz [101] and the PhD thesis of Franz Symalla [102].

2.3 ELECTRONIC STRUCTURE CALCULATIONS

All calculations of charge carrier mobility in this work require information about quantum mechanical properties, *e.g.* molecular orbitals, energy levels, partial charges and molecular dipole moments. These quantities can be calculated using methods such as density functional theory (DFT). The basic principles of this method are outlined in this chapter.

Density functional theory solves the stationary electronic Schrödinger equation for a system of interacting electrons and nuclei in an approximative way. One of the fundamental underlying approximations is the Born-Oppenheimer approximation. Furthermore, the real interacting electrons are replaced by a set of artificial non-interacting quasi particles in an effective potential caused by the other electrons and the nuclei. This mean field approximation and other assumptions lead to systematic errors which can in some cases be corrected but still have to be kept in mind when interpreting the results of DFT calculations.

2.3.1 BORN-OPPENHEIMER APPROXIMATION

The Hamiltonian of a system of n electrons and N nuclei consists of the kinetic energy operator of the electrons i, the kinetic energy of the cores I and the Coulomb interaction between electrons e and cores N with charge Z_I.

$$\hat{H} = \hat{T}_\mathrm{e} + \hat{T}_\mathrm{N} + \hat{V}_\mathrm{ee} + \hat{V}_\mathrm{eN} + \hat{V}_\mathrm{NN} \tag{2.18}$$

Using atomics units, the Hamiltonian can be written as

$$\hat{H} = \underbrace{-\sum_i^n \frac{1}{2}\nabla_i^2 - \sum_I^N \frac{1}{2m_I/m_\mathrm{e}}\nabla_I^2}_{\text{Kinetic energy}} + \underbrace{\sum_{i<j}^n \frac{1}{|\vec{r}_i - \vec{r}_j|} - \sum_{i,I}^{n,N} \frac{Z_I}{|\vec{r}_i - \vec{R}_I|} + \sum_{I<J}^N \frac{Z_I Z_J}{|\vec{R}_I - \vec{R}_J|}}_{\text{Coulomb interaction}} \; . \tag{2.19}$$

The kinetic energy of the nuclei is proportional to the ratio of electron mass m_e and the proton mass m_p, which is $m_\mathrm{e}/m_\mathrm{p}$ is $\approx 1/1\,836.15$. Thus, the motion of electrons happens on a time scale which is several orders of magnitude smaller than the movement of nuclei. The approximation of immediate equilibration of the electronic part of the wave function after changes of ionic degrees of freedom is called Born-Oppenheimer approximation. The electrons are considered as particles in an static electrostatic background potential created by the cores. Using this approximation, the electronic part of the full Schrödinger equation can be decoupled from ionic degrees of freedom. The total wave function factorizes into an

ionic part and an electronic part. The electronic part $\hat{H}_{\mathrm{e}}$ of the full Hamiltonian depends on the coordinates $\vec{R}_I$ of the nuclei in a parametric way:

$$
\begin{aligned}
\hat{H}_{\mathrm{e}} &= \hat{T}_{\mathrm{e}} + \hat{V}_{\mathrm{ee}} + \hat{V}_{\mathrm{eN}} + (\hat{V}_{\mathrm{NN}}) \\
&= -\sum_i^n \frac{1}{2}\nabla_i^2 + \sum_{i<j}^n \frac{1}{|\vec{r}_i - \vec{r}_j|} - \sum_{i,I}^{n,N} \frac{Z_I}{|\vec{r}_i - \vec{R}_I|} + \left(\sum_{I<J}^N \frac{Z_I Z_J}{|\vec{R}_I - \vec{R}_J|}\right) .
\end{aligned} \tag{2.20}
$$

The Coulomb potential $\hat{V}_{\mathrm{NN}}$ between nuclei leads to an additive constant E_{NN} in the eigenenergies and will be omitted in the following paragraphs. The remaining part of the Hamiltonian describes interacting electrons in the potential of fixed nuclei. The solution of the electronic Schrödinger equation using density functional theory will be presented in the next section.

2.3.2 DENSITY FUNCTIONAL THEORY

Density functional theory (DFT) was developed in the 1960s' and 70s' initiated by work of Pierre Hohenberg, Walter Kohn and Lu Jeu Sham based on the Thomas Fermi model [103]. Similar to the Hartree-Fock method derived in the previous Chapter, DFT provides a solution for the electronic wave function in the static potential of nuclei. Therefore, one starts with the electronic part of the Schrödinger equation in Born-Oppenheimer approximation:

$$
\left(\hat{T}_{\mathrm{e}} + \hat{V}_{\mathrm{ee}} + \hat{V}_{\mathrm{eN}}\right) \Psi(\{\vec{r}_i\}) = E\Psi(\{\vec{r}_i\}) \tag{2.21}
$$

Hohenberg and Kohn showed [104] that each non-degenerate ground-state $\Psi(\{\vec{r}_i\})$ of the electronic part of the Schrödinger equation is connected in a bijective way to a unique charge density $n(\vec{r})$. Similar to the Hartree-Fock method, the system of interacting electrons in an external potential can be expressed as a system of non-interacting particles in an effective potential. This effective potential is not a result of a mean-field approach equal to the Hartree potential but it includes and corrects all errors coming from the missing explicit correlation between the non-interacting particles. This leads to a Schrödinger equation in the form

$$
\left(-\frac{1}{2}\nabla^2 + v_{\mathrm{eff}}[n(\vec{r})] - \epsilon_i\right) \varphi_i(\vec{r}) = 0 . \tag{2.22}
$$

where the functions $\varphi_i(\vec{r})$ are called Kohn-Sham orbitals. This set of coupled equations is called Kohn-Sham equations [105]. The effective potential $v_{\text{eff}}[n(\vec{r})]$ is a functional of the electron density

$$n(\vec{r}) = \sum_i^n |\varphi_i(\vec{r})|^2 \; . \tag{2.23}$$

It is possible to split the effective potential into different parts.

$$v_{\text{eff}}[n(\vec{r})] = v_{\text{ext}}(\{\vec{R}_I\}) + \int_V \frac{n(\vec{r})}{|\vec{r} - \vec{r}\,'|} \mathrm{d}\vec{r}\,'^{\,3} + v_{\text{xc}}[n(\vec{r})] \tag{2.24}$$

The first part describes the potential caused by the nuclei and external electric fields. The second part describes the interaction of the respective electron with the Coulomb potential caused by the charge density of all electrons. This is similar to the Hartree-potential but includes an unphysical self-interaction of the particles with their own effective charge density. The third part formally contains all exchange and correlation effects. The exact knowledge of the exchange-correlation functional $v_{\text{xc}}[n(\vec{r})]$ would lead to exact solutions of the electronic Schrödinger equation. As the explicit form of this functional is unknown, it is necessary to find approximate exchange-correlation functionals. There exists a large variety of different functionals which were developed throughout the last decades for different systems and purposes. Two approaches for the development of exchange-correlation functionals and two important functionals for organic molecules will be described in the next section.

The Kohn-Sham equations (Eq. 2.22) can be solved numerically in a self-consistent way, namely with the self-consistent field method (SCF). In this method, the wave-functions (molecular orbitals, MOs) $\varphi_i(\vec{r})$ can be expressed as a linear combination of Gaussian- or Slater-type basis-functions (atomic orbitals) or as plane waves.

$$\varphi_i = \sum_j C_{ij} \phi_j \tag{2.25}$$

Possible basis-functions ϕ_j will be presented in more detail in section 2.3.2. In the SCF procedure, an initial set of coefficients C_{ij} is chosen and the Hamiltonian based on this choice is calculated. A numerical solution of the Kohn-Sham equations yields a new set of coefficients C_{ij} and therefore a new set of molecular orbitals φ_i. Iteration of this procedure leads to self consistent molecular orbitals φ_i and therefore a self-consistent solution of the Kohn-Sham equations.

There exists a large variety of different exchange-correlation functionals for DFT calculations. Two commonly used approximations for the construction of functionals are the local-density approximation (LDA) and the generalized gradient approximation (GGA). In LDA, the exchange-correlation functional only depends on the local charge density $n(\vec{r}_0)$ and therefore can be treated as a exchange-correlation potential:

$$v_{xc}[n(\vec{r})] \rightarrow v_{xc}(n(\vec{r}_0)) \ . \tag{2.26}$$

GGA functionals are constructed in a way that the exchange-correlation functional depends on the local charge density and its first spatial derivative:

$$v_{xc}[n(\vec{r})] \rightarrow v_{xc}(n(\vec{r}_0), n'(\vec{r}_0)) \ . \tag{2.27}$$

As known from literature [106], DFT calculations tend to underestimate the HOMO-LUMO gap of semiconductors. Especially for charged molecules which intrinsically may have a small band gap, this can lead to numerical convergence problems. Therefore, hybrid functionals were developed which contain parts of the explicit exchange energy from Hartree-Fock theory. This procedure leads to more realistic HOMO-LUMO gaps especially for organic molecules. Two functionals which are mainly used throughout this work are the BP86 functional and the hybrid B3LYP functional. BP86 is a combination of Becke's exchange functional from 1988 [107] and the Perdew 86 correlation functional [108]. B3LYP is a hybrid functional of the following form:

$$\begin{aligned} E_{xc} = 0.2 \cdot E_x(\text{HF}) + 0.72 \cdot E_x(\text{GGA}) + 0.08 \cdot E_x(\text{LDA}) \\ + 0.81 \cdot E_c(\text{GGA}) + 0.19 \cdot E_c(\text{LDA}) \end{aligned} \tag{2.28}$$

$E_x(\text{HF})$ is explicit Hartree-Fock exchange, $E_x(\text{GGA})$ is the a exchange functional derived by Becke *et al.* in 1988 [107], $E_c(\text{GGA})$ is a correlation functional derived by Lee, Yang and Parr [109] and $E_c(\text{LDA})$ is a LDA functional by Vosko *et al.* [110].

BASIS SETS

In Hartree-Fock and DFT calculations, the wave functions of quasiparticles are constructed as linear combinations of basis functions. One possible choice of basis functions are Slater functions [111]. These are the envelope functions of the hydrogen wave functions and thus a natural choice of atomic orbitals. As it is computationally expensive to numerically or analytically integrate Slater-type functions,

Table 2.2: Different basis-sets used in this work.

SV(P)	Split-valence basis set with polarization functions for all atoms expect hydrogen [23]. Default basis set in TURBOMOLE.
SVP	Split-valence basis set with polarization functions [23].
TZVP	Split-valence triple-ζ basis set with polarization functions [117].

they are commonly approximate by a certain number of Gaussian functions [112] which are easier to integrate [113].

In fast semi-empirical calculation, a minimal basis set such as the STO-nG basis [114] is used. The n represents the number of Gaussian functions which are used to approximate one Slater-type orbital. Each core and valence orbital is described by one Slater-type orbital.

More sophisticated basis sets are split-valence basis sets such as X-YZg [115] or X-YZWg. X is the number of Gaussian functions which are used to approximate the Slater-type orbital which is used for core orbitals. Valence orbitals are constructed of 2 (X-YZg), 3 (X-YZWg) or even more Slater-type orbitals. These are called double-ζ, triple-ζ, *etc.* basis sets, respectively. The number of Gaussian functions used to approximate the Slater-functions in these basis sets is denoted by Y, Z, W, ... Furthermore, additional basis functions are used to model polarization effects [116]. This is denoted with X-YZg* or X-YZWg*. The basis sets used in this work are shown in Tab. 2.2.

2.4 FORCE FIELD BASED MORPHOLOGY GENERATION

For the calculation of charge carrier mobility in disordered amorphous systems, atomistically resolved morphologies of sufficient size are required. Several different methods and approaches are used for this task. Most of them are based on parametrized classical force fields which describe intra- and intermolecular interactions. Molecules are represented by N point-like atoms, N_{b} bonds between these atoms, N_{a} angles between these bonds and N_{d} dihedral angles between planes defined by the angles. Deformation of the molecular geometry as well as interaction energies are modeled using these force fields. They consist of different terms describing several possible interactions between atoms. These are often divided into bonded and non-bonded terms.

$$
\begin{aligned}
V_{\mathrm{bonded}} = \ & \sum_{i}^{N_{\mathrm{b}}} k_{\mathrm{b},i}(r_i - r_{i,0})^2 \\
& + \sum_{i}^{N_{\mathrm{a}}} k_{\mathrm{a},i}(\theta_i - \theta_{i,0})^2 \\
& + \sum_{i}^{N_{\mathrm{d}}} V_{\mathrm{d},i}(\phi_i)
\end{aligned}
\tag{2.29}
$$

$$
\begin{aligned}
V_{\mathrm{non\text{-}bonded}} = \ & \sum_{i}^{N} \sum_{j>i}^{N} \frac{q_i q_j}{4\pi\varepsilon\varepsilon_0 r_{ij}} \\
& + \sum_{i}^{N} \sum_{j>i}^{N} V_{\mathrm{LJ}}(r_{ij})
\end{aligned}
\tag{2.30}
$$

Equation 2.29 describes the bonded interaction and has three terms. The first term is the energy of bond stretching in quadratic approximation. r_i is the bond length of bond i and $r_{i,0}$ is the equilibrium bond length of this bond. $k_{\mathrm{b},i}$ describes the force constant of the bond and depends on the atoms forming the bond and their chemical environment. The second term, also in quadratic approximation, describes the bending of angles between bonds. θ_i, $\theta_{i,0}$ and $k_{\mathrm{a},i}$ are defined analogously to the bond stretching term. The third and last bonded term describes the energy contributions $V_{\mathrm{d},i}(\phi_i)$ from dihedral angles ϕ_i. In many standardized force fields [118, 119], this term is approximated as a periodic cosine-like function with a certain periodicity and amplitude. As described in Chapter 3.1.1 and by MacKerell *et al.* [120] and Lukyanov *et al.* [121], molecule specific force fields are

required for a realistic description of dihedral potentials.

The non-bonded interaction is described in Eq. 2.30. The first term represents the Coulomb interaction between partial charges which are assigned to each atom. $\varepsilon\varepsilon_0$ is the permittivity of the material and r_{ij} is the distance $|\vec{r}_i - \vec{r}_j|$ between atoms i and j. The partial charges q_i and q_j represent the net charge density of each atom. These point charges are evaluated for each molecule individually using different methods, such as the projection of the charge density on the position of atoms (Mullikan charges [122]) or as a fit to reproduce the electrostatic potential of a molecule (ESP charges [123, 124]). The second non-bonded term is the classical Lennard-Jones (LJ) interaction between all pairs of atoms. It includes a repulsive term modeling the Pauli repulsion between the orbitals of different molecules and a term describing the van der Waals' interaction (attraction) due to correlated fluctuations of the charge density. The leading term in van der Waals' attraction is interaction between the fluctuating dipole moments which scales with the power of r_{ij}^{-6}. For numerical reasons, the Pauli repulsion is modeled using a r_{ij}^{-12} term. One possible definition of the Lennard-Jones interaction is given in Eq. 2.31.

$$V_{\mathrm{LJ}}(r) = 4\epsilon \left[\left(\frac{\sigma}{r}\right)^{12} - \left(\frac{\sigma}{r}\right)^{6} \right] \tag{2.31}$$

The energy ϵ is the depth of the LJ-potential while the length σ is defined via $V_{\mathrm{LJ}}(r = \sigma) = 0$. Other definitions of the Lennard-Jones potential use an exponential function or other distance dependencies to describe the Pauli repulsion.

2.4.1 MOLECULAR DYNAMICS (MD)

Molecular dynamics (MD) is a method which can be used for the simulation of the movements of molecules in an amorphous condensed state. In this method, Newtons equations of motion are solved for a system of atoms and molecules in an iterative way using the force fields derived in the last section. Changes of atom positions within one molecule lead to changes of bond lengths as well as angles between these bonds and dihedral angles. Non-bonded interaction is described via Coulomb interaction between the partial charges of atoms and Lennard-Jones interaction. Starting from an initial state of the system $(\{\vec{r}_i(t_0), \dot{\vec{r}}_i(t_0)\})$, the total energy as a function of the atom coordinates is calculated. Forces acting on the atoms are computed using the derivative of the total energy $V(\{\vec{r}_i(t_0)\})$ with respect to the atom coordinates.

$$m_i \ddot{\vec{r}}_i = \nabla_{\vec{r}_i} V\left(\{\vec{r}_i(t_0)\}\right) \tag{2.32}$$

New atom positions and velocities are then evaluated using a numerical integration with a time step Δt. Using the new coordinates and velocities $\{\vec{r}_i(t_0 + \Delta t), \dot{\vec{r}}_i(t_0 + \Delta t)\}$, the energy $V(\{\vec{r}_i(t_0 + \Delta t)\})$ can be re-evaluated. Kinetic energies are rescaled according to a given distribution in order to adjust the temperature of the system (thermostat). The pressure of the system and therefore the volume can be controlled via scaling of the atom positions (barostat). Iteration of this procedure leads to a time evolution (trajectory) of the system. Snapshots of this simulation after a certain equilibration time can be used as input for quantum mechanical analysis.

2.4.2 Monte Carlo based methods (MC)

Monte Carlo based methods for morphology generation like the Deposit protocol developed by Tobias Neumann [12] also start with a set of initial coordinates $\{\vec{r}_i\}_0$ and make use of random moves of single atoms to obtain new coordinates $\{\vec{r}_i\}_1$. The total energy E_1 of the new system is evaluated in a similar way as in MD methods and compared to the initial total energy E_0. The proposed step is accepted with a probability according to the Metropolis criterion shown in Eq. 2.33.

$$\omega(0 \rightarrow 1) = \begin{cases} 1 & \text{if } E_1 \leq E_0 \\ \exp\left(-\frac{E_1 - E_0}{k_\mathrm{B} T}\right) & \text{if } E_1 > E_0 \end{cases} \tag{2.33}$$

$$p(i)\omega(i \rightarrow j) = p(j)\omega(j \rightarrow i) \tag{2.34}$$

The acceptance criterion in in Eq. 2.33 fulfills the detailed balance given in Eq. 2.34. The detailed balance can be derived using the condition of a stationary microscopic state without net flux. $p(i)$ is the probability of the system to be in state i and $\omega(i \rightarrow j)$ it the transition probability for the transition from state i to state j.

$$\underbrace{p(i) \sum_{j \neq i} \omega(i \rightarrow j)}_{\text{flux out of state } i} = \underbrace{\sum_{j \neq i} p(j)\omega(j \rightarrow i)}_{\text{flux into state } i} \tag{2.35}$$

For a steady state, each single transition has to be in equilibrium, leading to

$$p(i)\,\omega(i \rightarrow j) = p(j)\,\omega(j \rightarrow i)\ . \tag{2.36}$$

Boltzmann statistics yield an occupation probability $p(i) \propto \exp\left(-E_i/(k_\mathrm{B}T)\right)$ of a state i with energy E_i. Thus, the ratio of $\omega(j \to i)$ and $\omega(i \to j)$ can be written as

$$\frac{\omega(i \to j)}{\omega(j \to i)} = \exp\left(-\frac{E_j - E_i}{k_\mathrm{B}T}\right) . \tag{2.37}$$

One way to fulfill this condition is the Metropolis criterion presented in Eq. 2.33.

In the Deposit algorithm, molecules are added to the simulation box sequentially. The energy of the system is evaluated using the force fields defined in Eq. 2.29 and 2.30. For each molecule, a certain number of Monte Carlo steps is performed in order to explore the potential energy surface and to find a position according to a Boltzmann distribution of energies at a temperature T. Several simulated annealing (SA) cycles are performed and accepted according to the Metropolis criterion. In each simulated annealing cycle, the temperature of the system is reduced from an initial temperature above room temperature to the desired end temperature of the system. The grid-based energy evaluation used in the Deposit method is independent of the number of molecules in the system. Therefore, the method scales linearly with the system size. This allows the generation of atomistic morphologies of sizes up to 10 000 molecules and more. Periodic boundary conditions perpendicular to the growth direction allow for further expansion of the morphologies.

3

Development of multiscale methods

Research on amorphous organic semiconductors throughout the past decades solved many fundamental aspects of charge transport. The charge transport mechanism and various properties determining the charge mobility and conductivity of organic semiconductors are now well understood (see Chapter 2.1.4). Examples for such properties are molecular dipole moments and distortions in the condensed state [90, 125–128]).

Despite the aforementioned research, methods which quantify charge carrier mobility and details of its molecular origin are presently lacking [90, 126]. Growing computational resources enable to close the gap between atomistic quantum mechanical calculations on the molecular level and continuum theories on the length scale of amorphous layers and devices. Such an approach requires many ingredients, such as an accurate description of the morphology and the electronic structure of the system as well as reliable models for the description of charge transport. This work presents the development and application of a simulation method which is capable of reliable and quantitative prediction of the charge mobility of organic semiconductors.

The simulation methods which were developed and used in this work will be introduced in this chapter. It is based on the theoretical background introduced in Chapter 2 and will be applied to problems concerning properties of amorphous organic materials in Chapter 4. The first part of this chapter introduces the concept of multiscale modeling for charge transport simulations in organic electronics. Due to the various different length scales determining charge transport properties of disordered materials, this modeling technique is an essential tool to capture all

relevant effects contributing to charge transport.

In Chapter 3.2, the central part of this multiscale workflow, namely the Quantum Patch method, is introduced. Using the Quantum Patch method, site energies, transfer integrals and other microscopic properties of amorphous systems can be calculated. It requires atomistically resolved morphologies and takes electrostatic interaction between molecules into account in a self-consistent way. This method was developed in my Master's thesis [69] and extended in this work. Chapter 3.4 introduces a mesoscopic demixing algorithm, which is used for the generation of 3D coarse grained morphologies of bulk heterojunctions used in organic solar cells. Parts of this chapter are based on Friederich *et al.* [68, 129–131], Rodin *et al.* [14] and Mönch *et al.* [132, 133].

3.1 MULTISCALE MODELING OF CHARGE TRANSPORT

As described in Chapter 2.1.4, charge transport in disordered organic materials can be described as a sequence of hopping processes between states which are localized on single molecules. The Marcus hopping rate (Eq. 2.4) can be used to quantify the dynamics of the hopping processes. It depends on several material specific parameters such as intermolecular electronic couplings, energy differences between initial and final states of the hopping processes and molecular reorganization energies. All of these microscopic quantities depend on the molecules and their electronic structure as well as their relative alignment and packing in amorphous molecular films. In strongly disordered materials, percolation effects on the $10 - 100\,\mathrm{nm}$ range start to play a role and determine charge mobility [51, 97, 134]. Therefore, charge transport properties such as charge mobility and conductivity can only be reliably calculated and predicted when all relevant length scales are taken into account. This can be achieved in a multiscale modeling approach, in which different length scales are modeled using different simulation techniques. Each of the tightly coupled models describes the relevant effects of the respective length scale. This procedure spans all length scales from single molecules (Å) to amorphous thin films and devices (nm−µm).

The entire multiscale workflow for the calculation of charge carrier mobility is depicted in Fig. 3.1. It starts with the parameterization of a single molecule. The ground state geometry, atomic partial charges representing the electrostatic potential created by the charge density of the molecule and soft internal degrees of freedom, in particular dihedral angles, are parameterized using DFT and semi-empirical methods (see Chapter 3.1.1). These parameters are used in the following morphology generation step. Atomistically resolved systems with a size of up to
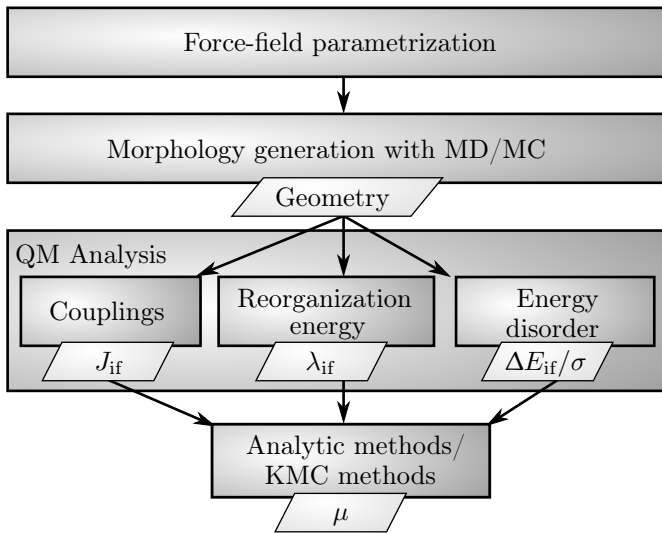
Figure 3.1: Schematic description of the multiscale workflow including molecule specific force field parameterization, followed by morphology generation and extraction of quantum mechanical parameters. The workflow ends with either approximative estimate of the charge carrier mobility or a numerical charge transport simulations using *e.g.* kinetic Monte Carlo (KMC) methods.

several thousand molecules are generated using classical force field based molecular mechanics (MD) or Monte Carlo (MC) methods (see Chapter 3.1.2). These classical methods model the interaction between the tightly coupled molecules using electrostatic point charges and standardized atom-specific Lenard-Jones potentials. In MD methods, hard internal degrees of freedom like bond lengths and angles are also treated on a standardized force field level [135, 136]. In the Monte Carlo based simulated annealing protocol Deposit [12] used in this work, bond lengths and angles are kept frozen. The atomistic morphologies obtained in this step are used in the next step to identify and characterize the electronic structure (see Chapter 3.1.3). This is done using the Quantum Patch approach [68] presented in Chapter 3.2 or with similar methods. In this method, site energies for localized polarons (electrons and holes including their polarization cloud), the energy disorder, electronic couplings between the states as well as reorganization energies including embedding effects are calculated. These are transfered to the next step, where macroscopic properties, such as charge mobility, are obtained using either approximative analytic approaches, *e.g.* the GEMM approach [14], or numerical methods such as kinetic Monte Carlo simulations. The latter are capable of simulating mixed materials, multilayer structures and full devices. Details on the single steps of the multiscale approach will be given in the next sections.

3.1.1 Molecule parameterization

The multiscale approach for calculation of the charge mobility of amorphous organic semiconductors starts with the analysis and parameterization of isolated molecules in vacuum. In this step, the gas phase geometry as well as electrostatic properties of the molecule are obtained in DFT calculations. The electrostatic potential created by the molecular charge density is analyzed and atom centered partial charges are fitted in order to reproduce a similar electrostatic potential. This procedure is called Merz-Singh-Kollman fit and the partial charges obtained are called ESP charges [123, 124]. For the generation of atomistic morphologies, the ground state geometry as well as molecular partial charges are used as input parameters for the classical force fields. Intermolecular interaction is described using molecule specific partial charges and general, element-specific Lennard-Jones parameters (see Chapter 2.4).

Intra-molecular degrees of freedom can be separated in two groups. Vibrational degrees of freedom such as the stretching of covalent bonds and bending of angles between them usually have excitation energies above room temperature and therefore do not play a relevant role. Additionally, local bond and angle deformations have only minor impact on the global geometry of the molecule in comparison to most dihedral angles. In molecular dynamics simulations, these degrees of freedom are modeled using a harmonic approximation using atom- and bond-specific parameters. In the Metropolis Monte Carlo based Deposit simulations used in this work, molecular bond lengths and angles are extracted from DFT optimizations and kept frozen during morphology generation.

The second group of internal degrees of freedom include the rotation of groups around single bonds. The angle between two planes defined by two molecular fragments is called dihedral angle. The dihedral potential and more specifically its energy minima and the energy barriers between these minima are molecule specific and can in most cases not be generalized as universal force fields. Therefore, the dihedral force field requires a molecule specific parameterization.

During this work, two methods for the parameterization of dihedral angles were developed and used. Both methods start from the optimized molecular structure and independently rotate the two molecular fragments connected by a dihedral angle with respect to each other. In the first method, the SIMONA package [137] is used for a stepwise rotation of a specific dihedral angle. The rotation is accomplished using a strong bias potential. In each rotation step, all other dihedral angles are relaxed to avoid steric clashes between other groups of the molecule. The final states of the stepwise rotation is then analyzed in DFT single-point cal-

culations. The total energies obtained in these calculations are used to generate the dihedral potential for the respective dihedral angle. This method has several drawbacks: Firstly, the dihedral potentials obtained with this method can be very noisy due to the MC-based relaxation of the molecule in each rotation step. This specifically applies for large molecules with many internal degrees of freedom. Secondly, the force field based relaxation itself requires dihedral potentials. This makes the use of generic dihedral potentials necessary. These, as mentioned above, are often inaccurate and might lead to systematic errors.

Therefore, a second method for the parameterization of dihedral potentials was developed, which only depends on quantum mechanical methods. Similar to the first method, each dihedral angle is rotated stepwise, followed by a relaxation of the rest of the molecule. In contrast to the first method, the rotation is forced in this case which might lead to clashes between molecular groups. This can be avoided by using a small step size. The relaxation of the rest of the molecule is performed using quantum mechanical methods, which do not require pre-parameterized dihedral potentials. To conserve and limit he required computation time, semi-empirical methods are used in this work. In general, more accurate DFT calculations are also possible. The full rotation of each dihedral angle is sampled in both rotation directions. At each angle, the minimum of the two energies from both rotation directions is chosen. This procedure avoids artificial, asymmetric potentials caused by steric tension between groups of the molecule, which may abruptly relax at some point during the rotation.

One remaining source of error in both methods lies in the initial structure of the molecule. In some molecules, the single bond connecting two groups via a dihedral angle is not symmetric but slightly bent in one direction. A rotation around this dihedral angle leads to an artificially asymmetric dihedral potential. The energy minimum of the DFT-optimized initial structure (dihedral angle of θ_0) should, for symmetric molecules, be equal to the energy minimum at $-\theta_0$. The bending of the angle in the initial structure lifts the symmetry, which reflects itself in different potential minima at θ_0 and $-\theta_0$. For many molecules, the influence of this asymmetry in the dihedral potential on the morphology is rather weak, which can have different reasons. In one scenario, the energy barriers of the dihedral potential between different minima are much smaller than the thermal energy at room temperature. This is the case for the rotation of single methyl side groups. In such examples, all dihedral angles are thermally accessible during the morphology generation and slight asymmetries do not play a role. In other cases, the energy barrier between θ_0 and $-\theta_0$ is so large that it is very unlikely for the molecule to overcome the barrier at room temperature. Thus, the conformation will stay in

the initial minimum and only sample the energy landscape around this dihedral minimum. The depth of the second minimum around $-\theta_0$ again does not play a role. Nonetheless, a solution to the problem of asymmetric dihedral potentials is part of ongoing work.

Another method for the parameterization of internal degrees of freedom uses the vibrational spectrum of a molecule, which can be obtained from diagonalization of the Hessian matrix. This method solves the issue of asymmetry. At the same time, it is independent of the arbitrary choice of hard and soft degrees of freedom. The vibrational eigenmodes are linear combinations of all possible changes of bond lengths, angles and dihedral rotations. The corresponding eigenfrequencies permit a quantitative classification of vibrations allowed at room temperature and vibrations which are very unlikely to be excited at room temperature. The analysis of the vibrational spectrum of molecules with respect to HOMO/LUMO levels and electrostatic properties was implemented in this work as a fast pre-screening tool for the internal degrees of freedom of single molecules. The potential energies obtained with this eigenmode analysis can, for technical reasons, not be used in most MD or MC packages for morphology generation as complex collective movements of multiple degrees of freedom would have to be taken into account.

3.1.2 Morphology generation

The second part of the multiscale modeling approach is the generation of atomistically resolved morphologies using classical methods. The force fields used in these molecular dynamics (MD) or Monte Carlo (MC) methods (see Chapter 2.4) are parameterized using the quantum mechanical molecular properties obtained in the first step of the workflow.

In this work, Monte Carlo based simulations using the Deposit package [12] as well as molecular dynamics [138, 139] based GROMACS simulations [140] were performed. Depending on the application, these two methods have advantageous or limiting inherent differences. The Deposit package mimics a vacuum deposition process in which a spatial anisotropy in growth direction can be observed. Molecular dynamics simulations on the other hand yield isotropic molecular orientations. At the same time, the intramolecular degrees of freedom in Deposit are restricted to dihedral movements, while in MD all molecular distortions are allowed. The restriction to dihedral movements in the Deposit method is artificial but in many cases necessary due to the lack of realistic force fields which often lead to artificially distorted molecules. Moreover, vibrations including the stretching of bonds and the bending of bond angles have high excitation energies which are unlikely to occur at room temperature.

Molecular dynamics

In the GROMACS-based [140] MD simulations presented in Chapter 4.4 and in Friederich *et al.* [131], the following algorithm was used: The molecules were parameterized according to the general AMBER force field (GAFF) [136]. Partial charges were obtained using semi-empirical AM1-BCC calculations [141, 142]. The performance in the prediction of thermodynamic properties of the general AMBER force field was shown in two benchmark studies on a wide range of small organic molecules [143, 144]. In the molecular dynamics simulation, periodic boundary conditions (PBC) were used in all spatial directions.

The simulation itself incorporates three steps: sample preparation, simulation of the liquid phase and annealing to the solid phase. Initially, a cubic box is filled with disordered molecules with a density of $0.9\,\text{g/cm}^3$, where unphysical close contacts are removed. Velocities of the atoms are distributed according to a temperature of $800\,\text{K}$. The simulation starts with a $10\,\text{ps}$ run in the NVT ensemble, which means that the number of molecules, volume and temperature are kept constant are kept constant. This relaxation equilibrates the initial velocity distribution. After this sample preparation step, a longer equilibration is performed for $1\,\text{ns}$ at a temperature of $800\,\text{K}$ using a NPT ensemble at constant number of molecules, pressure and temperature. During this second step, the mean squared displacements of the centers of mass of all molecules have to be larger than the characteristic size of one molecule. This ensures that the system is in a liquid state. At the same time, the density of the system is equilibrated at a pressure of $1\,\text{bar}$. In the third and last step, the system is annealed from a temperature of $800\,\text{K}$ to a temperature of $300\,\text{K}$ with a cooling rate $100\,\text{K/ns}$ during a NPT simulation. Afterwards, a final $2\,\text{ns}$ NPT equilibration is performed at $300\,\text{K}$ to generate a trajectory of the solid amorphous system at room temperature. The solid state is characterized by a mean squared displacement of molecules which is smaller than the typical molecule size. In this state, the molecular motion is constrained by the neighboring molecules and only thermal vibrations occur.

Deposit

In Deposit simulations [12] (see Chapter 2.4.2), morphologies are generated in a sequential way by depositing one molecule after another. The deposition process of each molecule consists of N_{SA} simulated annealing cycles (SA). In each cycle, N_{MC} Metropolis Monte Carlo steps are performed while the temperature is decreased from T_{high} to T_{low} using a geometrical cooling schedule. After each SA cycle, the final state of the cycle is accepted using the Metropolis Monte Carlo acceptance

criterion at a temperature of T_{acc}. Details of the Metropolis criterion can be found in Chapter 2.4.2. Typical Deposit simulations performed in this work use 10 to 20 SA-cycles with 10^4-10^5 Monte Carlo steps each. The number of Monte Carlo steps required for a converged molecular density depends on the number of internal degrees of freedom of the molecules. Large molecules with many dihedral angles require up to $\mathcal{O}(10^5)$ MC steps, while for rigid molecules, $\mathcal{O}(10^4)$ MC steps are sufficient. Due to technical improvements, the maximum system size in Deposit simulations grew to more than 10 000 molecules. Typical Deposit morphologies used in Chapter 4.6 include 1000 molecules which were periodically extended in x- and y-direction (perpendicular to growth direction).

Beyond force field based morphology generation

In MD as well as MC based methods for morphology generation, two fundamental approximations exist which can lead to inaccuracies and systematic errors. The first approximation lies in the parametrization of the aforementioned force field. Especially for complex molecules such as large conjugated systems, the parametrization may be inaccurate due to the generic nature of the force field. Various quantum mechanical effects are neglected, as they cannot be mapped to the functional form of the force field. This makes molecule specific force fields necessary

A second issue arises from the calculation of electrostatic interactions between molecules. In force field based methods, the charge density is mapped on atom-centered partial charges and the electrostatic interaction between these point charges is evaluated. In most force field based MD and MC methods, these partial charges are calculated in advance. During the simulation, the molecular geometry changes upon internal distortions of the molecules, while the partial charge associated with each atom is kept constant. This static model is a rough approximation to real changes of the charge density within a molecule. A more realistic model requires re-evaluation of the partial charges after each molecular distortion on a quantum mechanical level. Even on semi-empirical level, this is very expensive in terms of computational cost.

To get more physical morphologies, these two issues have to be solved. As one possible solution, a hybrid QM/MM method using an algorithm similar to the Deposit method is possible. Here, the explicit relaxation of each new molecule is done in a quantum mechanical or semi-empirical structure optimization. All molecules within a certain cut-off distance to the new molecule are explicitly taken into account. Long range electrostatic interaction with molecules further

apart can still be described using partial charges. The atom positions of already deposited and relaxed molecules at the interface between the explicit neighbors and the point charge embedding have to be fixed. In this way, it is possible to treat the internal degrees of freedom of each molecule in a quantum mechanical way. At the same time, more accurate point charges are used, which reproduce the electrostatic potential of the individual charge density of each molecule in the classical force field step.

3.1.3 ELECTRONIC CHARACTERIZATION

In the third step of the multiscale workflow shown in Fig. 3.1, the atomistic morphologies generated in the second step are analyzed in a quantum mechanical model. All parameters necessary for the calculation of Marcus hopping rates are computed in this step (see chapter 2.2.1). These parameters include the on-site energies for electrons and holes in the system, reorganization energies and electronic couplings.

SITE ENERGIES

In this work, the site energies are calculated using the Quantum Patch method, which will be described in detail in Chapter 3.2. In this method, additional charges (electrons and holes) are assigned to certain molecules in the system and the ionization potential (IP) and electron affinity (EA) as well as other molecular properties are calculated. Effects of intermolecular interactions such as polarization are intrinsically included in a self-consistent way.

REORGANIZATION ENERGIES

The calculation of reorganization energies is based on Nelsen's four-point-pro ce dure [64] (see Chapter 2.2.1). In this work, three different techniques are applied, from which two are newly developed. In many publication, the reorganization energy is assumed to be a molecular property, which does not depend on the specific individual environment in which a molecule in an amorphous structure is embedded. All steps of the four-point-procedure (neutral relaxation, charging, charged relaxation, discharging, neutral relaxation) are evaluated in vacuum in this approximation.

An extension to this procedure is the incorporation of embedding effects. These restrict the full relaxation of the molecule during the geometry optimizations of the four-point-procedure. In the frozen-dihedral approximation, the intramolecu-

45

lar degrees of freedom leading to the largest changes in molecular conformation, namely the dihedral rotations, are kept frozen in the state of the molecule in the amorphous morphology. All relaxations of bond lengths and angles are allowed, making conformational changes along breathing modes possible. The relaxation of these breathing modes often occurs during the charging and discharging process of a molecule.

In a third method for the computation of reorganization energies, embedding effects are taken into account in an intrinsic way. Instead of an explicit restriction of the molecular reorganization, the Pauli repulsion of neighboring molecules acts as a limitation for the molecular reorganization. This is done using a density embedding approach where the atoms and the electron density of the neighboring molecules are modeled as effective potentials which interact with the charge density of the central molecule. For practical reasons, effective core potentials (ECPs) are used in this work. These are fitted to reproduce the repulsive potential of the closed electronic shells of each atom.

ELECTRONIC COUPLINGS

The third group of parameters necessary for the calculation of Marcus rates are the intermolecular electronic couplings. In this work, they are calculated using molecular frontier orbitals obtained in a self-consistent equilibration of the electronic structure of amorphous systems. The formalism for the calculation of electronic couplings is described in Chapter 2.2.1. Fock and overlap matrices ($\mathbf{F}$ and $\mathbf{S}$) for molecular pairs are obtained from DFT single-point calculations of dimer systems. Electrostatic embedding effects are taken into account in the Quantum Patch formalism (see Chapter 3.2). The Fock and overlap matrices can be calculated using the coefficient matrix $\mathbf{c}$ and the diagonal matrix of orbital energies $\mathbf{E}$.

$$\mathbf{S} = \mathbf{c}^{-1} \cdot (\mathbf{c}^{-1})^{\dagger} \tag{3.1}$$

$$\mathbf{F} = \mathbf{c}^{-1} \cdot \mathbf{E} \cdot (\mathbf{c}^{-1})^{\dagger} \tag{3.2}$$

Electronic coupling elements between the frontier orbitals of molecules i and j extended on the dimer basis are then calculated using Eq. 3.3 (see also chapter 2.2.1).

$$J_{ij} = \frac{\langle i| F |j\rangle - \frac{1}{2} \left(\langle i| F |i\rangle + \langle j| F |j\rangle \right) \langle i| S |j\rangle}{1 - \langle i| S |j\rangle^2} \tag{3.3}$$

3.1.4   Charge carrier mobility

Charge transport based on the microscopic parameters and systems obtained in the previous steps of the multiscale workflow can be simulated in various different ways (see Chapter 2.2.3). In this work, an effective medium model is used to estimate an upper bound of the charge carrier mobility. This model is based on an approximative solution of the master equation using Marcus hopping rates. The so-called generalized effective medium model (GEMM) and is described in Chapter 2.2.3. Its functional form of the charge mobility is shown in Eq. 2.17. The advantage of this effective medium model compared to numerical simulations is the possibility to analyze its different microscopic contributions. This helps to determine and understand molecular properties which influence the charge carrier mobility or organic materials. This analysis will be shown in Chapter 4.5.

3.2 Quantum Patch method

This chapter will revisit the Quantum Patch approach, a method originally developed during my master's thesis in 2013 [69]. The Quantum Patch approach was extended and extensively used throughout this work [68, 129, 130, 145]. The aim of the Quantum Patch method is the calculation of the electronic structure of large amorphous systems consisting of weakly coupled molecules. The method is based on the self-consistent evaluation of the electronic state of each molecule while taking intermolecular electrostatic interaction into account in a self-consistent way. In this way, large system sizes of up to several thousand molecules can be analyzed. Such system sizes are impossible to calculate using *e.g.* standard DFT. At the same time, the Quantum Patch method can confine charges, excitations or charge transfer states to certain parts of the system. This opens the possibility for detailed analysis of non-equilibrium states of the system.

The first part of this chapter will give a brief introduction into the methodology of the Quantum Patch method. The other parts explain the application of the Quantum Patch method on neutral systems as well as on the treatment of additional charges, excitations and charge transfer processes.

3.2.1 Methodology

In this section, an approach for the self-consistent evaluation of the electronic states of an amorphous system of weakly coupled molecules will be derived. Starting point of the derivation is the electronic part of the interacting many-body Hamiltonian of a molecular system (see Chapter 2.3). Using the principles of frozen density embedding in DFT [146, 147], the system is partitioned into a number of sub-systems. Formally, this cannot be done exactly due to missing contributions to the kinetic energy functional in the Kohn-Sham formalism. A detailed discussion can be found in my Master's thesis [69]. In the regime of weakly coupled molecules, the error due to this approximation becomes negligible.

The second part of the derivation goes beyond frozen density embedding. Here, only Coulomb interaction between electrons of different parts of the system is taken into account while correlation and exchange effects are neglected. The motivation of this is again the weakly coupled nature of small molecule systems. This additional approximation leads to a formal description of the system of electrostatically interacting single molecules as a block diagonal Hamiltonian. The electronic state of this system can be obtained using a self-consistent solution of the system of coupled single-molecule Schrödinger equations. Partial charges of

each molecule in the system are re-evaluated in each step of the self-consistency loop. These point charges are used to model the electrostatic interaction of the molecules, which couples the single Schrödinger equations.

Wesolowski *et al.* [146, 147] describe another approach, in which the weak exchange and correlation effects between electrons of different molecules are taken into account in an effective way. Such density embedding approaches lead to exact results in systems of weakly coupled molecules in the sense of Marcus-theory but require development of effective exchange-correlation functionals.

The derivation of the Quantum Patch method starts with the total energy functional of DFT which can be derived from the electronic Hamiltonian in Born-Oppenheimer approximation (see Chapter 2.3).

$$
\begin{aligned}
E[n(\vec{r})] =& \hat{V}_{\mathrm{NN}} + \int n(\vec{r}) v_{\mathrm{nuc}}(\vec{r}) \mathrm{d}\vec{r} \\
&+ \frac{1}{2} \int \frac{n(\vec{r})n(\vec{r}')}{|\vec{r} - \vec{r}'|} \mathrm{d}\vec{r}^3 \mathrm{d}\vec{r}'^3 \\
&+ \hat{T}_{\mathrm{e}}[n(\vec{r})] + \hat{E}_{\mathrm{xc}}[n(\vec{r})] \ .
\end{aligned}
\tag{3.4}
$$

In this equation, $\hat{V}_{\mathrm{NN}}$ describes the constant Coulomb interaction between the nuclei at positions $\{\vec{R}_I\}$. It is constant and will be set to zero from now on. The second term is the potential energy of the electron density in the electrostatic potential $v_{\mathrm{nuc}}(\vec{r}) = \sum_I^N Z_I/(|\vec{r} - \vec{R}_I|)$ caused by the nuclei. The third term is a mean field Coulomb interaction similar to the Hartree term describing the interaction of the electron density with itself. The kinetic energy functional $\hat{T}$ evaluates the kinetic energy of the non-interacting quasiparticles. $\hat{E}_{\mathrm{XC}}$ is the exchange-correlation functional, which corrects errors of the mean-field approximation in the Hartree term and errors due to the non-interacting particles in the kinetic energy functional. Formally, the energy functional in Eq. 3.4 leads to a correct evaluation of the total energy of a system. Nonetheless, the exact form of the exchange-correlation functional is not known which leads to systematic errors in DFT.

The M molecules in amorphous systems investigated in this work are only weakly coupled. This enables the partitioning of the system into M fragments. The total density n therefore splits up into different parts n_i.

$$
n(\vec{r}) = \sum_i^M n_i(\vec{r})
\tag{3.5}
$$

The Hamilton operator for a system of M weakly coupled molecules with electron densities $n_i(\vec{r})$ that only interact with each other via electrostatic interaction is expressed in Eq. (3.6).

$$\hat{H} = \begin{pmatrix} \hat{H}_1 \left[\sum_{i=1}^{M} n_i(\vec{r}) \right] & 0 & \cdots \\ 0 & \hat{H}_2 \left[\sum_{i=1}^{M} n_i(\vec{r}) \right] & \cdots \\ \vdots & \vdots & \ddots \end{pmatrix} \tag{3.6}$$

$$\equiv \hat{H}_1 \oplus \hat{H}_2 \oplus ... \oplus \hat{H}_M$$

As indicated by the sum notation, the Hamilton operators of different molecules act on different subspaces of the Hilbert-space. They only influence each other via the electrostatic potential caused by their electron density and their cores. Therefore, each single molecule Hamiltonian is a functional of the total charge density. As explained above, one can neglect exchange and correlation effects between the different weakly coupled molecules. A consequence of this is that the Hamiltonian in Eq. 3.6 has no eigenstate (orbital), which is delocalized over more than one molecule. Thus, no hybridization between molecules takes place. This approximation is in agreement with the charge transport model describing localized states, which move through the system in a sequence of hopping processes.

The Schrödinger equation of the system can now be written as a system of coupled differential equations.

$$\hat{H}_i \left[n_i(\vec{r}) + \sum_{j=1, j \neq i}^{M} n_j(\vec{r}) \right] |\varphi_i\rangle = E_i |\varphi_i\rangle \tag{3.7}$$

The full charge density is intentionally split into the charge density $n_i(\vec{r})$ of molecule i and the charge densities $n_j(\vec{r})$ of the environment molecules. This splitting will be used further below. The dependency of the charge densities $n_j(\vec{r}) = |\langle \varphi_j(\vec{r}) | \varphi_j(\vec{r}) \rangle|^2$ on the wave functions $|\varphi_j\rangle$ of all other molecules leads to a coupling of the single equations. Assuming that partial charges q, which are fitted in the scheme of Merz, Singh and Kollman [123, 124], can approximately reproduce the electrostatic potential created by the charge density of a molecule, one can substitute the electron density of a molecule j in the environment by the sum of its partial charges $q_{j,k}$.

$$n_j(\vec{r}) \rightarrow \tilde{n}_j(\vec{r}) = \sum_k q_{j,k} \cdot \delta(\vec{r} - \vec{R}_{j,k}) \tag{3.8}$$

The system of coupled Schrödinger equations (3.7) decouples for the case that the partial charges for all surrounding molecules are known. This leads to a system of M uncoupled equations (3.9) that explicitly include the electrons and cores of only one molecule.

$$\tilde{H}_i \left[n_i(\vec{r}) + \sum_{j \neq i,k} q_{j,k} \left[\tilde{n}_j(\vec{r}) \right] \cdot \delta(\vec{r} - \vec{R}_{j,k}) \right] |\tilde{\varphi}_i\rangle = \tilde{E}_i |\tilde{\varphi}_i\rangle \qquad (3.9)$$

Here, the partial charges $q_{j,k}$ implicitly depend on the charge density $\tilde{n}_j(\vec{r})$ of molecule j. By guessing initial partial charges of all molecules, one can self-consistently solve this set of equations. In each iteration of the self-consistency loop, the system of decoupled Schrödinger equations (3.9) is solved using numerical methods similar to those applied for the solution of the Kohn-Sham equations of density functional theory (DFT) (see Chapter 2.3). New wave-functions for the molecules are obtained, which yield new electron densities $\tilde{n}_i(\vec{r}) = |\langle \tilde{\varphi}_i(\vec{r}) | \tilde{\varphi}_i(\vec{r}) \rangle|^2$ and new partial charges. These charges enter the single molecule Hamiltonians of the next step. Iteration of this procedure will lead to a convergence of the charge densities $\tilde{n}_i(\vec{r})$, the Hamiltonians $\tilde{H}_i[n_i(\vec{r})]$ and finally the energies $\tilde{E}_i$.

To calculate the Marcus hopping rates of electrons and holes (Eq. 2.4), the site energy differences ΔE between charged hopping sites is needed as an input. The site energy of each molecule can be approximated as electron affinity and ionization potential of the molecule. These energies depend on the chemical structure of the molecule, its individual conformation and its unique (electrostatic) environment. These site energies can be calculated for each molecule in the system using the Quantum Patch method presented above.

3.2.2 Neutral systems

Within the Quantum Patch method, it is possible to equilibrate neutral molecular systems. This procedure is described in my Master's thesis [69] and in Friederich *et al.* [68, 129, 130]. The scheme of the neutral Quantum Patch method is illustrated in Fig. 3.2. After an initial step in which the partial charges of each molecule are obtained in vacuum calculations, the self-consistent iterations begin. The partial charges of all molecules are used as electrostatic embedding for the calculation of new partial charges of each molecule. These calculations can be performed independently from one another in parallel. The embedding charges are updated after each iteration step until convergence is reached. After that, molecular properties such as HOMO and LUMO levels of each molecule in the system can be extracted.

Neutral system including disorder and
polarization effects
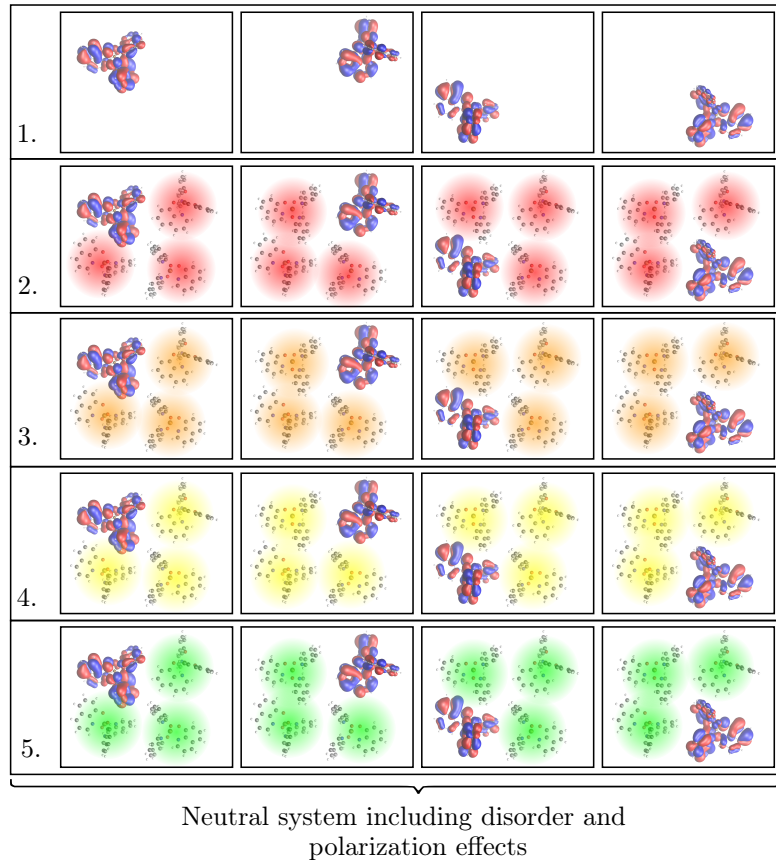
Figure 3.2: Pictorial description of the algorithm used for the calculation of energy disorder in a system of 4 neutral Alq_3 molecules. In the first step (first row), vacuum partial charges of each molecule are calculated. Afterwards, the partial charges of the molecules are re-evaluated within a cloud of explicit point charges until convergence of the total energies of all molecules is reached (rows 2-5). Energy disorder can be estimated from the distribution of orbital energies of the molecules. The width of the distributions of HOMO and LUMO orbitals can be interpreted as the energy disorder for hole and electron transport, respectively.
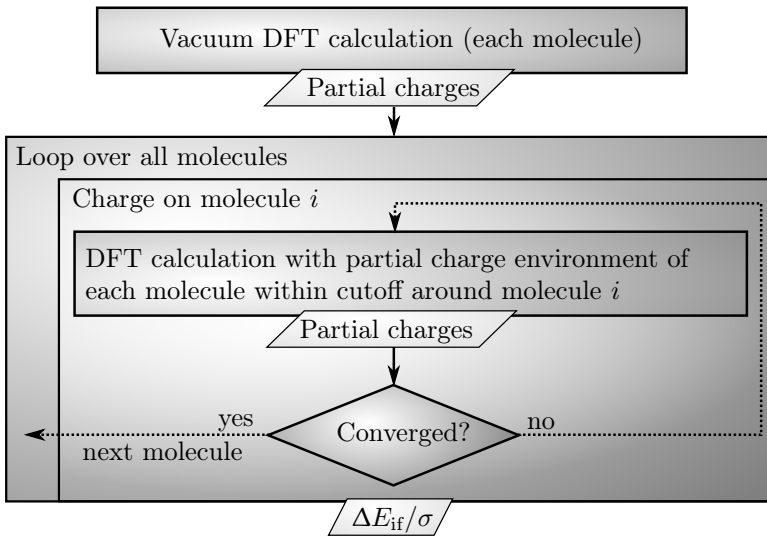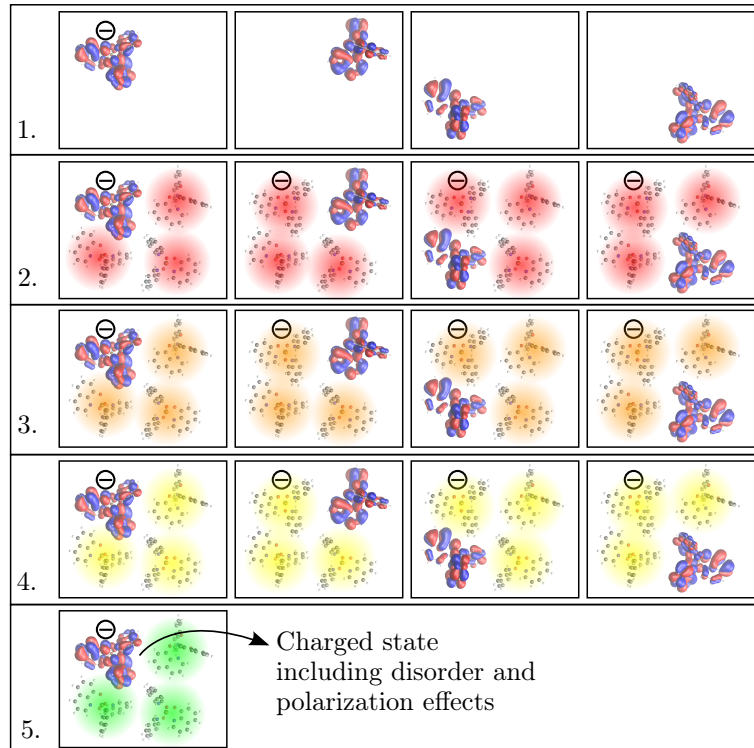
Figure 3.3: Schematic description of the algorithm used for the calculation of energy disorder within the charged Quantum Patch method. In a first step, vacuum partial charges of each molecule are calculated. Afterwards, an additional charge is assigned to a certain molecule. Partial charges of this molecule and of each of its neighbors within a certain cut-off distance are re-evaluated. The self-consistent iterations are repeated until convergence of the total energy of the charged molecule is reached. This procedure is repeated for positive and negative additional charges on each molecule in the system.

3.2.3 Modeling of additional charges, excitations and charge transfers

In addition to the analysis of neutral systems, additional charges can be assigned to certain molecules in the system. The algorithm for this extension of the neutral Quantum Patch method is shown in Fig. 3.3. In this algorithm, an additional charge is assigned to molecule i and its vacuum partial charges are calculated. These and the vacuum partial charges of the surrounding (neutral) molecules j enter as initial parameters into the self consistent calculation of new states $|\varphi_i^{-/+}\rangle$ of the charged molecule and $|\varphi_{j\neq i}\rangle$ of the uncharged molecules. In the next step, the partial charges $q_{i,k}^{-/+}$ of the charged molecule i and the partial charges $q_{j\neq i,k}^0$ of the now polarized molecules j are calculated. Iterations are performed until the energies $E_{\mathrm{tot},i}^{-/+}$ of charged molecule i within the polarized environment converge. This scheme is depicted in Fig. 3.3 and Fig. 3.4 and has to be repeated with positive and negative charges on each molecule in the system.

To study polarization effects due to explicit additional charges and in order to calculate ionization potentials (IP) and electron affinities (EA), a reference calculation without additional charges is required. This reference calculation can

Figure 3.4: Pictorial description of the algorithm used for the calculation of energy disorder in a system of 4 Alq$_3$ molecules with one additional electron on the upper left molecule. In the first step (first row), vacuum partial charges of each molecule are calculated. During the following self-consistent iteration, partial charges of the charged molecules and of each of its neighbors are re-evaluated until convergence of the total energy of the charged molecule is reached (rows 2-5). This procedure is repeated for positive and negative additional charges on each molecule in the system (not shown in the figure).

be done using the neutral Quantum Patch method described in Section 3.2.2. Using this data, one can calculate the ionization potential of molecule i as

$$\text{IP}_i = E_{\text{tot},i}^{\text{env},+} - E_{\text{tot},i}^{\text{env},0} \ . \tag{3.10}$$

The index "tot" denotes that total molecular energies are used and "env" means that the electrostatic environment of the positively charged ("+") or neutral ("0") state is taken into account. The electron affinity can be estimated using

$$\text{EA}_i = E_{\text{tot},i}^{\text{env},-} - E_{\text{tot},i}^{\text{env},0} \ . \tag{3.11}$$

This procedure can be used to calculate the energy difference ΔE_{ij} between two molecules i and j for the Marcus hopping rate of electrons ("$-$") and holes ("+").

$$\Delta E_{ij} = \left(E_{\text{tot},j}^{\text{env},-/+} - E_{\text{tot},j}^{\text{env},0} \right) - \left(E_{\text{tot},i}^{\text{env},-/+} - E_{\text{tot},i}^{\text{env},0} \right) \tag{3.12}$$

Rearrangement of these terms leads to

$$\Delta E_{ij} = \left(E_{\text{tot},j}^{\text{env},-/+} + E_{\text{tot},i}^{\text{env},0} \right) - \left(E_{\text{tot},i}^{\text{env},-/+} + E_{\text{tot},j}^{\text{env},0} \right) \tag{3.13}$$

The first of the two terms can be interpreted as total energy of the dimer system after the hopping process, while the second term describes the total energy of the system before the hopping process. This is in agreement with the Marcus formalism shown in Fig. 2.5a. It is necessary to keep in mind that each of the total energy terms E_{tot} includes the full electrostatic interaction with the environment. Therefore, $E_{\text{tot},j}^{\text{env},-/+}$ includes the Coulomb interaction with molecule j in the uncharged state. This Coulomb contribution is also included in $E_{\text{tot},i}^{\text{env},0}$, which leads to a double counting of this interaction energy. The same double counting of Coulomb interaction is included in the second state where molecule j is neutral and molecule i is charged. Thus, the double counting partially cancels out. To correct this double counting error, it is possible to reduce the environment of the uncharged molecules by contributions coming from the charged molecules (denoted with "env*").

$$\Delta E_{ij} = \left(E_{\text{tot},j}^{\text{env},-/+} + E_{\text{tot},i}^{\text{env*},0} \right) - \left(E_{\text{tot},i}^{\text{env},-/+} + E_{\text{tot},j}^{\text{env*},0} \right) \tag{3.14}$$

As indicated in the name of this section, the Quantum Patch method is not only restricted to the analysis of additional charges in a molecular system. Excitations, charge transfer states and combinations of all can also be modeled within the framework of the method. If, as an example, charge transfer complexes between donor and acceptor molecules have to be analyzed, it is possible to either treat these complexes as one single fragment of the system or to enforce an integer charge transfer by treating the charge transfer dimer as two oppositely charged

molecules.

The same principle can be applied for the analysis of excited molecules. The coupling of the different molecules via point charges makes it possible to treat the central, excited molecule with another method than the polarized molecules in its environment. Using such a hybrid approach, different methods for the description of the electronic structure can be combined. In particular, higher level methods such as coupled cluster approaches or the GW method for the more accurate description of excited states can be combined with standard DFT methods for the evaluation of the polarization effect. The implementation of such a hybrid method will be presented in the next chapter.

3.2.4 HYBRID QUANTUM PATCH METHOD

The Quantum Patch method introduced in this chapter is computationally demanding. As described in Chapter 3.2.3, the modeling of additional charges and excitations leads to high computation times. Nonetheless, the method scales linearly with the number of molecules in the system. This is achieved by partitioning of the system into single molecules which are only coupled via their electrostatic interaction.

For each charged or excited molecule which is analyzed, the electrostatic interaction between the neighboring molecules in a shell of about 25 Å (approximately 100 molecules) around the central molecule needs to be calculated in a self-consistent way. In addition, the electrostatic background potential of all molecules within a cutoff distance of 60 Å (up to 3000 molecules) enters the calculation in a static way. This segmentation is based on the slowly decaying electrostatic interaction between charges and molecular dipole moments which requires the consideration of a large number of molecules for a converged electrostatic embedding. The polarization effect of additional charges on the other hand decays relatively fast, making a smaller polarization shell around the central site possible.

In general, the Quantum Patch is not limited to treat all molecules in all shells on the same level of accuracy. As only the properties of one central molecule are analyzed, it is possible increase the accuracy of computations of this molecule. This also allows the analysis of excited states of this molecule with methods which go beyond standard DFT or Hartree-Fock. Furthermore, it becomes possible to reduce the computational cost of the Quantum Patch calculation by using more approximate methods for molecules which only indirectly enter the calculation. A possible approach for the implementation of hybrid methods will be explained in

the next section. Results of the hybrid Quantum Patch approach will be presented in Chapter 4.3.

Methodology

In the hybrid QM/QM Quantum Patch approach, fast semi-empirical DFTB [148] calculations for remote shells around a central molecule are combined with more accurate DFT calculations for the charged central site and its direct neighbors. In the Quantum Patch method, the interaction between molecules is mapped onto clouds of molecular partial charges. These point charges are fitted to mimic the static and induced dipole moment and higher electrostatic moments of the molecules. Usually, the charge-dipole interaction between the charged central site and its neighboring molecules is the leading contribution to the electrostatic interaction.

If the molecular dipole moments calculated using the DFTB method are comparable to their DFT counterparts, replacements of expensive DFT calculations at least for remote parts of the system are possible without loss of accuracy. To investigate the potential and limitation of this DFT/DFTB combination, the molecular morphology is partitioned into a number of regions as shown in Fig. 4.4 of Chapter 4.3. Different segmentation schemes are then compared to the result and performance of the standard Quantum Patch method where explicit additional charges are considered.

The first approximation to the charged Quantum Patch method is the treatment of polarized and unpolarized molecules in remote areas with the faster semi-empirical DFTB2 method. This will be referred to as the "hybrid large" method. The next approximation is the replacement of the DFT calculations in direct neighborhood to the central molecule with DFTB calculations (the "hybrid small"). In this case, all molecules except the charged molecule will be treated with DFTB. A full DFTB treatment of all molecules including the charged molecule completes the comparison of the calculations with the full Quantum Patch method ("semi-empirical").
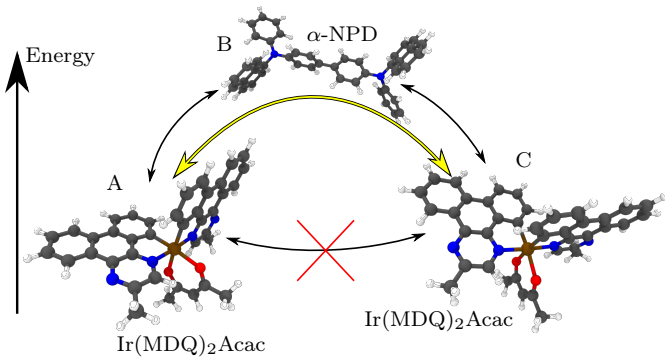
Figure 3.5: In a superexchange process, a charge hops from molecule A to molecule C via a virtual state localized on molecule B.

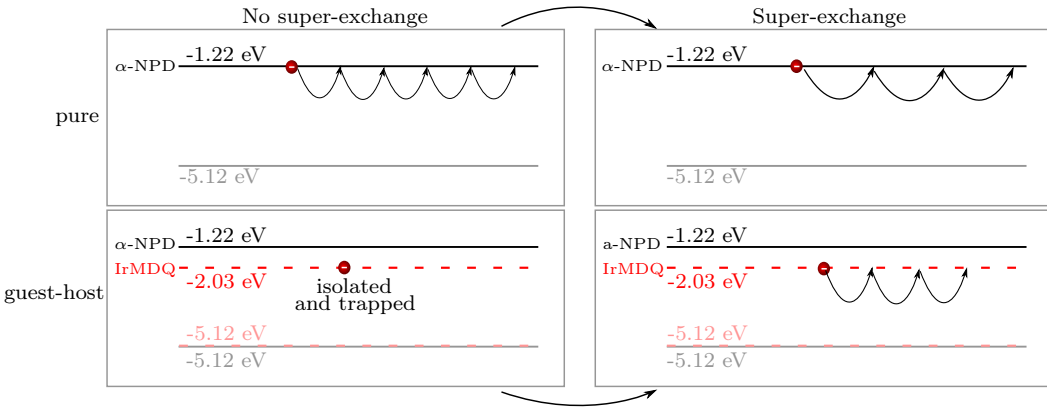## 3.3 SUPEREXCHANGE MECHANISM IN HOPPING TRANSPORT

Direct hopping processes involving two molecules as initial and final states are the most important contribution to charge transport in many disordered systems. Nonetheless, higher-order processes exist, which also contribute to the charge mobility. These higher-order processes involve states on more than two molecules, where only the states on the initial and final molecule are real, whereas the states on intermediate molecules are virtual. This process is depicted in Fig. 3.5 for one intermediate state. Besides systems such as loaded metal-organic frameworks [18], it plays a role in mixed guest host systems as used in emissive layers of OLEDs. Such a system is depicted in Fig. 3.6. The hopping rate for the superexchange process can be expressed as a Marcus rate (see Eq. 3.15) with a modified electronic coupling, which can be derived using first order perturbation theory (Eq. 3.16).

$$k_{\mathrm{AC}} = \frac{2\pi}{\hbar} \left| J_{\mathrm{sx}} \right|^2 \frac{1}{\sqrt{4\pi\lambda_{\mathrm{AC}}k_{\mathrm{B}}T}} \exp\left(-\frac{(\lambda + \Delta E_{\mathrm{AC}})^2}{4\lambda_{\mathrm{AC}}k_{\mathrm{B}}T} \right) \qquad (3.15)$$

The transfer integrals J_{sx} for charge hopping processes including a virtual state on the bridging molecule are calculated using first order perturbation theory. In agreement with literature [149, 150], this yields a hopping matrix element

$$J_{\mathrm{sx,AC}} = \frac{J_{\mathrm{AB}}J_{\mathrm{BC}}}{\Delta E_{\mathrm{sx}}} \ , \qquad (3.16)$$

where A is the initial molecule, C the final molecule and B the virtual transition state molecule. ΔE_{sx} is the vertical energy difference between the virtual state and the A-C-transition state in the transition state geometry (see Fig. 3.7a). As the transition state geometry is not known, one can use the formalism of the Marcus

Figure 3.6: The superexchange mechanism plays an important role in guest-host systems with a low guest concentration, where the guest molecules act as traps for charge carriers. Superexchange facilitates guest-to-guest hopping via virtual host states.

theory to derive an expression for the energy difference ΔE_{sx}. In general, it is possible to separate ΔE_{sx} in three contributions:

$$\Delta E_{\mathrm{sx}} = \Delta E_{\mathrm{rel}} - \Delta E_1^* + \Delta E_2^* \tag{3.17}$$

The first contribution E_{rel} depends only on the two ground states of an additional charge localized on one of the two molecules. These ground state energies can be predicted in microscopic simulations. The last two contributions incorporate energies of transition state geometries, which are not accessible in a straight-forward way. Nonetheless, using the assumption of harmonic potential energy surfaces from Marcus theory, it is possible to calculate the contributions ΔE_1^* and ΔE_2^*. The derivation in Section 3.3.1 yields the following expression for ΔE_{sx}.

$$\Delta E_{\mathrm{sx}} = E_{\mathrm{B}} - \frac{E_{\mathrm{A}} - E_{\mathrm{C}}}{2} + \frac{\lambda_{\mathrm{B}}}{2} \tag{3.18}$$

In principle, the superexchange coupling element from Eq. 3.16 is reduced by a factor of $J/\Delta E_{\mathrm{sx}}$ compared to a non-superexchange coupling. Typical electronic couplings are in the order of $1 \cdot 10^{-3}\,\mathrm{eV}$, whereas typical energy differences are in the order of $0.1\,\mathrm{eV}$, leading to a reduction in electronic coupling by a factor of 10^2 and a reduction of the rate by a factor of 10^4.

3.3.1 ENERGY DENOMINATOR

Using the harmonic potential energy approximation shown in Fig. 3.7, one can calculate the three components given in Eq. 3.17 for the energy denominator ΔE_{sx} required in Eq. 3.16 to calculate the superexchange coupling element J_{sx}. The

first component is the difference between the state where the additional charge is localized on the initial molecule and the state, where it is localized on the bridging molecule:

$$\Delta E_{\text{rel}} = E(A_{\text{N}}B_{\text{C}}^{*}C_{\text{N}}) - E(A_{\text{C}}^{*}B_{\text{N}}C_{\text{N}}) = E_{\text{B}} - E_{\text{A}} \tag{3.19}$$

The calculation of ΔE_{1}^{*} uses the assumption of Marcus theory that the potential energy surface of a molecule can be approximated as a harmonic function of a multi-dimensional reaction coordinate centered around the ground state geometry. This yields:

$$\begin{aligned}
\Delta E_{1}^{*} &= E(A_{\text{T}}^{*}B_{\text{N}}C_{\text{T}}) - E(A_{\text{C}}^{*}B_{\text{N}}C_{\text{N}}) \\
&= E(A_{\text{T}}^{*}C_{\text{T}}) - E(A_{\text{C}}^{*}C_{\text{N}}) \\
&= \frac{1}{4\lambda_{\text{AC}}}(\Delta E_{\text{AC}} + \lambda_{\text{AC}})^{2}
\end{aligned} \tag{3.20}$$

To estimate ΔE_{2}^{*}, it is helpful to consider the single-molecule picture as shown in Fig. 3.7b. Under the assumption of equal curvatures of the charged and uncharged potential energy surfaces of molecules A and C, one can split ΔE_{2}^{*} in two contributions.

$$\begin{aligned}
\Delta E_{2}^{*} &= E(A_{\text{T}}B_{\text{N}}^{*}C_{\text{T}}) - E(A_{\text{N}}B_{\text{C}}^{*}C_{\text{N}}) \\
&= (E(A_{\text{T}}C_{\text{T}}) - E(A_{\text{N}}C_{\text{N}})) + \frac{\lambda_{\text{B}}}{2}
\end{aligned} \tag{3.21}$$

In the second step, the definition of the reorganization energy for molecule B was used:

$$\frac{\lambda_{\text{B}}}{2} = E(B_{\text{N}}^{*}) - E(B_{\text{C}}^{*}) \ . \tag{3.22}$$

One can now partition $E(A_{\text{T}}C_{\text{T}}) - E(A_{\text{N}}C_{\text{N}})$ in two single molecule contributions and again use Marcus theory to obtain

$$E(A_{\text{T}}) - E(A_{\text{N}}) = \frac{1}{2}\frac{1}{4\lambda_{\text{CA}}}(\Delta E_{\text{CA}} + \lambda_{\text{CA}})^{2} \tag{3.23}$$

and

$$E(C_{\text{T}}) - E(C_{\text{N}}) = \frac{1}{2}\frac{1}{4\lambda_{\text{AC}}}(\Delta E_{\text{AC}} - \lambda_{\text{AC}})^{2} \ . \tag{3.24}$$

Combining everything above yields:

$$\Delta E_{\text{sx}} = E_{\text{B}} - \frac{1}{2}(E_{\text{A}} + E_{\text{C}}) + \frac{\lambda_{\text{B}}}{2} \ . \tag{3.25}$$
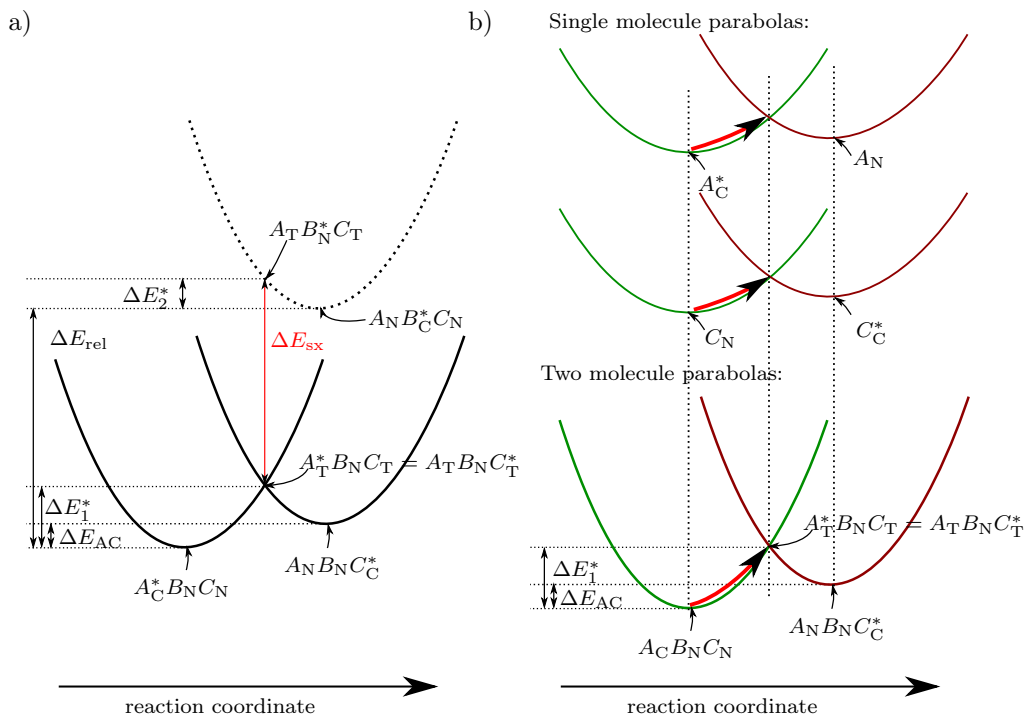
Figure 3.7: a) Three molecule parabolas showing the contributions of the energy denominator E. b) Single molecule parabolas and combined two-molecule parabolas for the charge transfer process from molecule A to molecule C. The geometry of molecule B remains in its neutral state.

This is a symmetric expression which can be interpreted as the difference between the energy of the virtual transition state and the mean energy of the initial and the final states. An additional contribution of $\lambda_B/2$ of the transition molecule is added to this energy difference. The reason for this is that the virtual transition molecule was only virtually occupied and could not respond to the occupation.

61

3.4 Monte Carlo based demixing algorithms

Amorphous thin films consisting of two or even more phase-separated components as used in in organic solar cells. The phase-separated morphology is called bulk heterojunction. It can be produced by co-deposition of two materials in a vacuum deposition process. Alternatively, it can be printed from a solution of the different components followed by an annealing process. The demixing process usually happens at temperatures well above room temperature on a seconds to minutes time scale. Demixing is drastically decelerated when the thin film is cooled to room temperature, leading to a meta stable, glassy state of the thin film. The domain size of the phase separated structure depends on the annealing temperature and duration. In case of solution processed films, the concentration and solubility of the materials in the solvent as well as the processing technique, post-treatment of the films and the evaporation temperature of the solvent play an important role in domain formation.

As explained in Chapter 2.1.2, efficient exciton separation requires small material domains in the bulk heterojunction, while for efficient charge extraction, larger domains are desirable. These two opposed requirements have to be balanced in order to maximize the power conversion efficiency. Typical domain sizes of efficient solar cells are in the order of $10\,\mathrm{nm}$ (several thousand molecules), while demixing times are in the order of seconds or more. This renders atomistic simulations impossible. Molecule based coarse grained MD or MC simulations [151–153] including several thousand molecules offer a possible solution, but are still computationally highly demanding. An alternative to these simulations are thermodynamics based phase field approaches.

In this chapter, an efficient model for the simulation of phase separated multi-component bulk heterojunctions will be presented. Acceleration techniques for this method are presented in Appendix C. All presented methods are based on the quantization of space in a cubic lattice with lattice constant a. General phase-field approaches assign a certain phase to each of the cubes i, which can for example be the material concentration φ_i of one of the materials of a binary mixture. The approaches described in this chapter only considers completely demixed materials and therefore only use φ_i values of 0 or 1. Thus, each voxel only contains either material A or material B of a binary A-B-mixture (see Fig. 3.8).

During the Metropolis Monte Carlo simulation, random exchanges of neighboring voxels are proposed and accepted with a certain probability. This probability is calculated using the Metropolis Monte Carlo criterion (Eq. 3.26, see also Chap-

ter 2.4.2). It depends on the difference between the total energy of the system before and after the exchange process.

$$\omega(0 \to 1) = \begin{cases} 1 & \text{if } E_\text{f} \leq E_\text{i} \\ \exp\left(-\frac{E_\text{f} - E_\text{i}}{k_\text{B} T}\right) & \text{if } E_\text{f} > E_\text{i} \end{cases} \tag{3.26}$$

In this equation, ω is the acceptance probability, T is the temperature and k_B the Boltzmann constant. The energies E_i and E_f are calculated based on the interaction energy between the voxels. The energy model can be based on molecule specific *ab initio* calculations as shown in Chapter 3.4.2). As an alternative, one can also use an *ad hoc* energy model as shown in Mönch *et al.* [132]. This energy model assigns interaction energies to each voxel interface, which depend on the content of the two connected voxels. In a realistic energy model, energy densities of interfaces between different materials are pre-calculated. In such a model, the interaction energy also depends on the interface area a^2.

In case the Metropolis criterion for a proposed move with a initial energy E_i and a final energy E_f is fulfilled, the move is accepted and the system is updated. Afterwards, a new move is proposed. The initial configuration is a random configuration with desired concentrations of all materials.

3.4.1 DEMIXING WITH AND WITHOUT EXTERNAL CONSTRAINTS

In case of free demixing, exchange moves between all neighboring voxels are proposed independent of the direction of interchange. External constraints can be introduced, if required by the purpose of the simulation. These constraints can *e.g.* restrict proposed moves to certain directions in order to fix local concentrations. To compare simulations to experimental measurements and in order to generate realistic three-dimensional representations of two-dimensional experimental data (as shown in Chapter 4.7.5), an algorithm is useful which constrains exchange of voxels in vertical direction (z-direction). In this way, the projection of the three-dimensional structure in z-direction is kept frozen.

By appropriate choice of the initial three-dimensional voxel distribution, the system can be generated in a way that the z-projection is equal to a two-dimensional experimental input. As an example, this input can be obtained from STEM-EDX measurements, as explained in Chapter 4.7.5. The element specific STEM-EDX measurements yield the integrated amount of a certain element or material as a function of the lateral position within a thin film. In this way, these measurements give quantitative results about the lateral material distribution and can be used as input for the constraining algorithm mentioned above. In Fig. 3.8, only moves
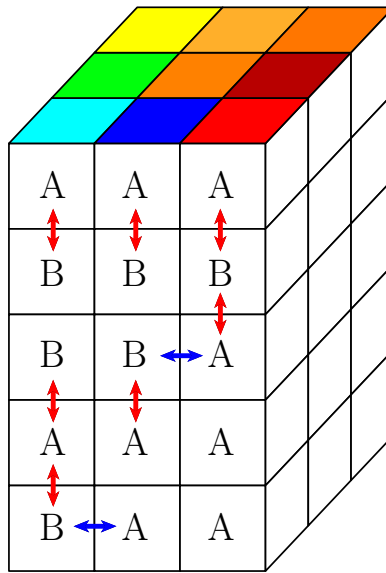
Figure 3.8: A system of voxels containing two materials A and B. The arrows indicate the possible moves of the system. The colormap on top of the box represents the projection of the content of one of the materials in z-direction. In case of demixing with two-dimensional constraints, only moves in z-direction are allowed (red arrows).

marked with red arrows are allowed. The (experimental) projection in z-direction is indicated using the colormap on top of the system.

3.4.2 Parameterization of interaction energies

For the methods presented in Chapter 3.4.1, an energy model is required. More specifically, the evaluation of the Metropolis criterion presented in Eq. 3.26 requires energy terms for interface energies of homointerfaces (A-A or B-B) or heterointerfaces (A-B).

One way to obtain these interface energies is by generating atomistically resolved morphologies (for example using the Deposit method as described in Chapter 3.1.2) including either one material or a junction of two materials in a layer-on-layer structure. Based on this morphology, interface pairs are identified using distance criteria on the pair distance and the maximum distance of each molecule to the (local) interface. Using these pairs, the interaction energy density can be extracted in two ways. In a first approach, the classical intermolecular Lennard-Jones and Coulomb energies of each pair are calculated and added up to a total interaction energy. The interface energy density can be obtained by dividing this total energy by the area of the morphology which was generated and analyzed. Edge effects can be avoided using periodic boundary conditions during the mor-
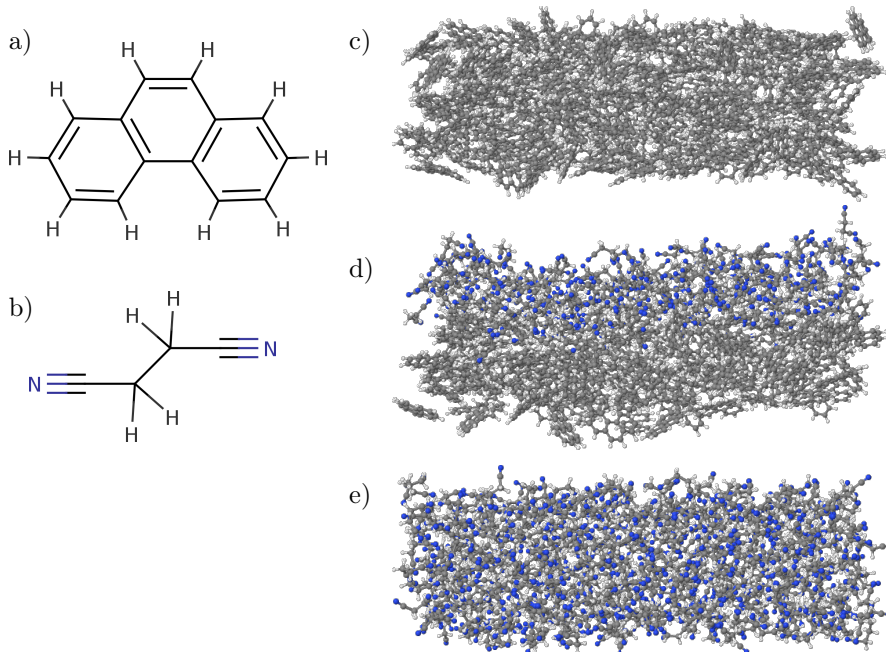
Figure 3.9: In a) and b), the molecular structure of phenanthrene and succinonitrile is shown. The images in c)-e) show atomistically resolved (bilayer) systems of c) phenanthrene, d) phenanthrene on succinonitrile and e) succinonitrile. These systems are used for the parameterization of interaction energies for the Monte Carlo based demixing simulation.

phology generation and energy extraction. In a second, quantum mechanical approach, pair energies are obtained from DFT calculations of molecular pairs as defined above. Here, the total energy of a pair is calculated and the total energies of the single molecules are subtracted. In this way, the Coulomb energy is calculated more accurately than in the first method and repulsive Pauli interaction is included. Dispersion corrections accounting for attractive van der Waals interaction have to be explicitly added to correct the missing electron correlation in DFT.

Fig. 3.9 shows two molecules, namely phenanthrene (PHEN) shown in Fig. 3.9a and succinonitrile (SUC) shown in Fig. 3.9b, which are discussed in Singh *et al.* [154]. To simulate the phase separation of these two molecules, atomistic morphologies were generated and used to parameterize the interaction energy as explained above (Fig. 3.9c-e). This calculation using classical Lennard-Jones energies yields interface energy densities of $E_{\mathrm{PHEN,PHEN}} = -0.42\,\mathrm{eV/nm^2}$, $E_{\mathrm{PHEN,SUC}} = -0.65\,\mathrm{eV/nm^2}$ and $E_{\mathrm{SUC,SUC}} = -1.00\,\mathrm{eV/nm^2}$. A further discussion and usage of these parameters will be found in the Master's thesis by Manuel Konrad [155].

4
Method application, results and discussion

4.1 INTRODUCTION

Amorphous organic semiconductors based on small molecules are used in a wide spectrum of applications (see Chapter 2.1), *e.g.* in organic light emitting diodes or in organic solar cells. Disordered organic materials possess a low charge carrier mobility ($\mu \approx 10^{-10} - 10^1 \, \text{cm}^2/(\text{Vs})$ [156]) compared to typical inorganic semiconductors ($\mu \approx 10^2 - 10^4 \, \text{cm}^2/(\text{Vs})$) [157–159]. This limits the efficiency of devices as well as the range of possible applications, *e.g.* in large area devices. The low charge mobility is mainly determined by the mechanism of charge transport in disordered systems itself, *i.e.* hopping transport (see Chapter 2.1.4). The aim of this work is the identification of factors determining and potentially limiting the charge mobility of disordered organic materials. Relations between microscopic molecular properties and macroscopic charge carrier mobility are identified and used for the systematic improvement of the electron mobility of a widely used electron transport material (Alq_3). This proof of principle shows that *in silico* screening of numerous chemical compounds for the development of highly efficient opto-electronic devices is useful and promising.

In Chapter 4.3 and 4.4, the multiscale method outlined in Chapter 3.1 is applied to calculate energy disorder and hole mobility of the materials presented in Chapter 4.2. Different approaches for the calculation of energy disorder of electrons and holes are tested and benchmarked in Chapter 4.3. Microscopic molecular properties and macroscopic hole mobility of different compounds are presented and discussed in Chapter 4.4. To understand the molecular origin of charge mobil-

ity, several molecular properties which influence the hole mobility of thin films are identified and explained in Chapter 4.5. Such structure-property relationships enable the postulation of design rules for high mobility materials. A proof of principle of these design rules is given in Chapter 4.6, where new compounds based on Alq$_3$ are investigated theoretically. A promising candidate showing a high electron mobility is identified, synthesized and electronically characterized. Measurements show a three orders of magnitude increase in electron mobility of the *in silico* designed molecule compared to the reference material.

4.2 MATERIALS

To test and validate the multiscale methods presented in Chapter 3, the following widely studied small molecule organic semiconductors were used: Tris(8-hydroxyquinolinato)aluminum (Alq$_3$), N4,N4'-di(biphenyl-3-yl)-N4,N4'-diphenyl-biphenyl-4,4'-diamine (mBPD), N1,N4-di(naphthalen-1-yl)-N1,N4-diphenylbenzene -1,4-diamine (NNP), 1,1-bis-(4,4'-diethylaminophenyl)-4,4-diphenyl-1,3,butadinene (DEPB), N,N'-bis(1-naphthyl)- N,N'-diphenyl-1,1'-biphenyl-4,4'-diamine (α-NPD), N,N'-diphenyl-N,N'-bis-(3-methylphenylene)-1,10-diphenyl-4,40-diamine (TPD), N,N'-bis-[9,9-dimethyl-2-fluorenyl]-N,N'-diphenyl-9,9-dimethylfluorene-2,7-diamine (pFFA), tetracene (TET) and pentacene (PEN).

These compounds are shown in Fig. 4.1. They represent a wide range of experimentally investigated organic semiconductors. Alq$_3$ is an example of a commonly used material in electron transport layers (ETL) of OLEDs, whereas α-NPD is an established hole transport layer (HTL) material. The first seven materials (Alq$_3$ to TPD) form disordered films, whereas tetracene and pentacene are mainly used in their crystalline phase. The hole mobility of these materials spans a range of more than ten orders of magnitude, which represents a challenge for any modeling approach. Furthermore, α-NPD, Tris(4-carbazoyl-9-ylphenyl)amine (TCTA) and Spiro-4,4'-Bis(2,2-diphenylvinyl)-1,1'-biphenyl (Spiro-DPVBi) (see Fig. 4.2) are used for the investigation of correlations presented in Appendix E and F. An analysis of their orbital structure and degeneracy is presented in Appendix D. For the active layer of the solar cells discussed in Chapter 4.7.5, the C$_{60}$ Fullerene and the dicyanovinyl-substituted oligothiophene derivative DCV5T-Me were used (see Fig. 4.3).
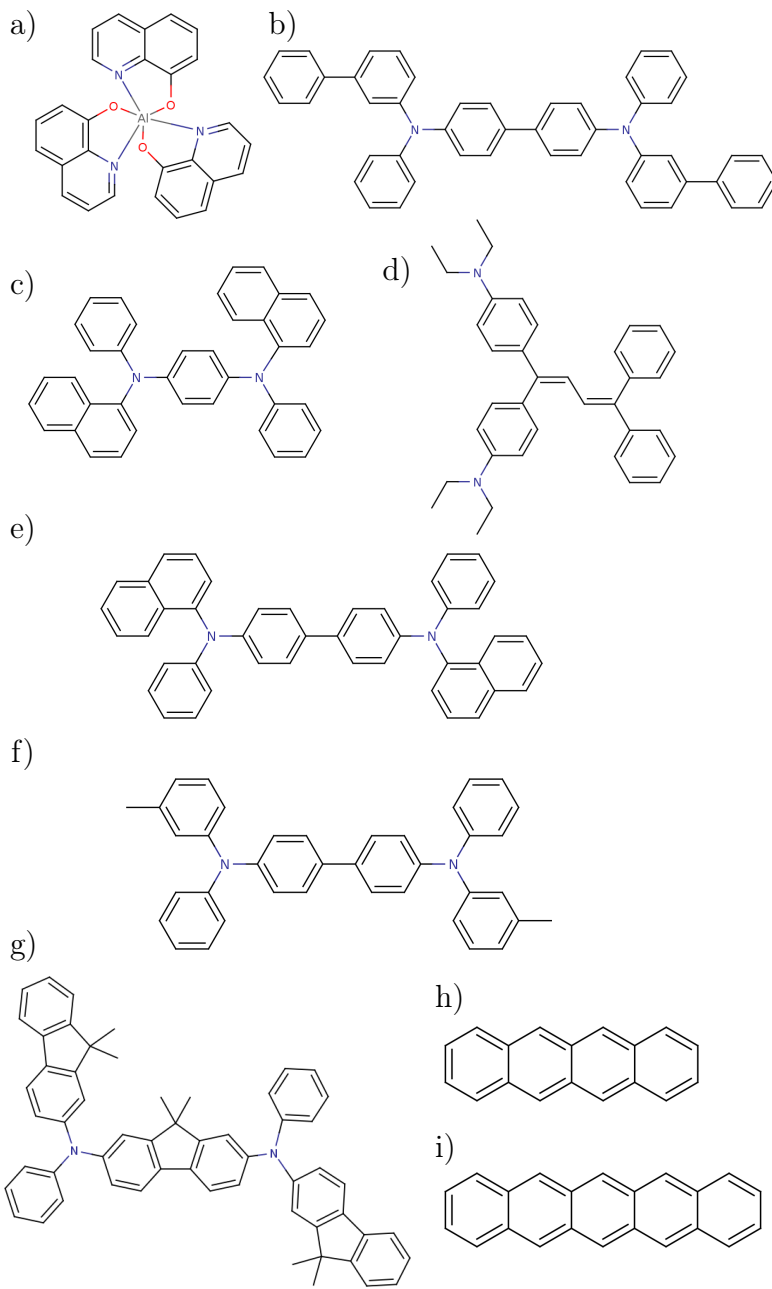
Figure 4.1: a) Alq$_3$, b) mBPD , c) NNP, d) DEPB, e) α-NPD, f) TPD, g) pFFA, h) tetracene, i) pentacene. The energy disorder and hole mobility of these experimentally widely studied materials is analyzed in Chapter 4.3 and 4.4. While Alq$_3$ us usually used as an electron conducting material, all other materials are mainly used in hole transport layers of organic light emitting diodes or organic solar cells.
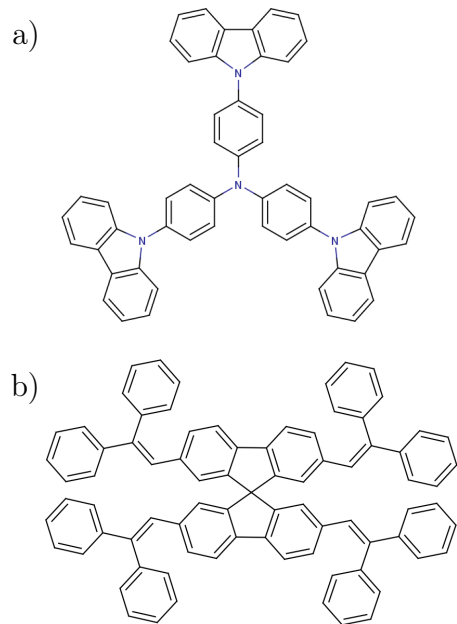
Figure 4.2: a) TCTA, b) Spiro-DPVBi. The correlations between energy levels of these two materials (and α-NPD shown in Fig. 4.1e) are analyzed in Appendix E and F.
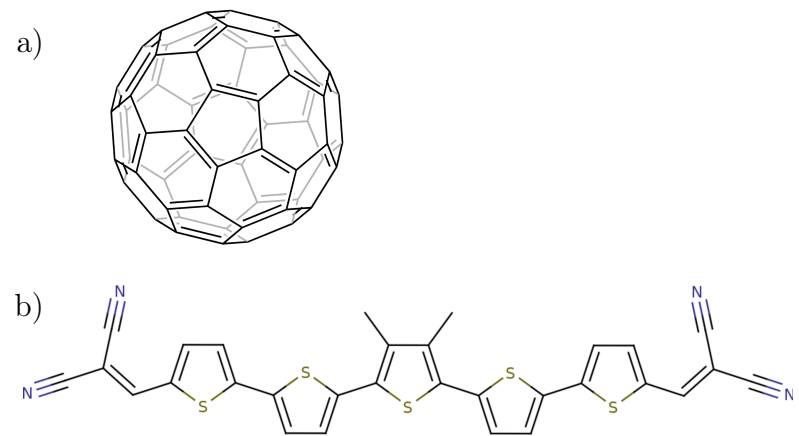
Figure 4.3: a) C_{60} (Fullerene), b) DCV5T-Me. These two materials are studied in Chapter 4.7.5, where they are applied in an active bulk heterojunction layer of an organic solar cell.

4.3 APPLICATION AND VALIDATION OF THE QUANTUM PATCH METHOD

To test and validate the quantum patch method presented in Chapter 3.2 and its hybrid extension presented in Chapter 3.2.4), different protocols for the calculation of energy disorder in organic semi-conductors are tested in this chapter. The protocols are defined in Tab. 4.1 and apply for the partitioning scheme shown in Fig. 4.4. Most of the data and discussion presented in this chapter was published in Friederich *et al.* [129]. For each protocol, the energy disorder of seven widely studied materials is calculated (Alq$_3$, α-NPD, DEPB, mBPD, NNP, pFFA and TPD, see Fig. 4.1). The zero-field mobility of these materials covers a range between $1 \cdot 10^{-10}$ cm^2/(Vs) for Alq$_3$ [160–164] to $7.6 \cdot 10^{-4}$ cm^2/(Vs) for pFFA [165]. The results of the various protocols are shown in Fig. 4.5. A benchmark of the results is shown in Appendix B

The "full QM" calculations are performed using the charged Quantum Patch method as derived in Chapter 3.2.2 and 3.2.3. They are used as reference calculations for the hybrid approach presented in Chapter 3.2.4. In the "QM one shell only" method, one shell of molecules surrounding the charged species is used as embedding in the Quantum Patch method. Full polarization cannot take place (see convergence calculations in Friederich *et al.* [68, 69]), resulting in an overestimation of the energy disorder. At the same time, large parts of the electrostatic background potential are neglected which also influences energy disorder and correlations.

Table 4.1: Five different partitioning schemes for the (hybrid) Quantum Patch method are tested. The different regions (defined in Fig. 4.4 and in the text) are the charged molecule (charged mol.) and different shells which are treated in a self-consistently way (s.-c.) or as static partial charges.

		full QM	QM one shell only	hybrid large	hybrid small	semi-empirical
Charged mol.	s.-c.	DFT	DFT	DFT	DFT	DFTB
12 Å env.	s.-c.	DFT	DFT	DFT	DFTB	DFTB
25 Å env.	s.-c.	DFT		DFTB	DFTB	DFTB
60 Å env.	static	DFT		DFTB	DFTB	DFTB
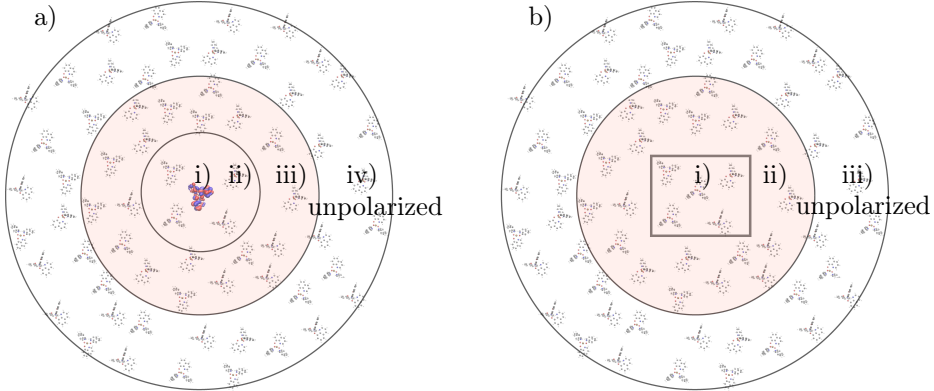
Figure 4.4: a) Cutoff scheme for the full hybrid quantum patch method including explicit polarons. The colored regions are treated in a self-consistent way and contain about 100 molecules. Region i): charged molecule. Region ii): next nearest neighbor molecules within a cutoff distance of 12 Å. Region iii): neighbors within a distance of 25 Å. Region iv): unpolarized molecules within a cutoff distance of 60 Å (approximately 3000 molecules). b) Cutoff scheme for the neutral Quantum Patch method where the system is equilibrated without explicit additional charges. Region ii): molecules within a 25 Å cutoff distance around the central part i) of the morphology. Each molecule in regions i and ii) is treated in a self-consistent way. The energy disorder is only extracted in the central region i) to avoid edge-effects at the border between polarized and unpolarized regions. Region iii) corresponds to region iv) in the charged Quantum Patch method shown in panel a).

To correct these errors, the "hybrid large" method is introduced. In this method, the first coordination shell of molecules around the charged centers are fully calculated using DFT. A second shell of molecules in distances between 12 Å and 25 Å is treated in a self-consistent way using semi-empirical methods. The long-range electrostatic background (distances between 25 Å and 60 Å) is calculated once and kept static. This method leads to very accurate energy disorder parameters compared to the "full QM" method for all tested materials (see Fig. 4.5 and Tab. 4.2 and 4.3). At the same time, it leads to a reduction of CPU-time of about one order of magnitude (see Fig. B.1).

In the "hybrid small" method, only charged molecules are treated on a DFT level. All neighboring molecules in self-consistently evaluated shells as well in the static shell are computed using DFTB. This method yields energy disorder values with deviations of $-10\,\%$ and $+10\,\%$ to the "full QM" results for Alq_3 (electrons) and NNP (holes), respectively. As charge carrier mobility is exponentially dependent on the square of the energy disorder ($\mu \propto \exp(-C(\beta\sigma)^2)$ [14, 49, 53, 166, 167], the "hybrid small" method will lead to considerable errors in mobility. Thus, it is not accurate enough to be used as a predictive tool for the screening of novel

Table 4.2: Energy disorder of holes computed using the protocols introduced in Tab. 4.1

	Energy disorder of holes σ [eV]				
	full QM	QM one shell only	hybrid large	hybrid small	semi-empirical
Alq$_3$	0.240	0.258	0.247	0.246	0.191
α-NPD	0.155	0.198	0.156	0.149	0.090
mBPD	0.133	0.156	0.143	0.142	0.119
DEPB	0.126	0.142	0.130	0.131	0.069
NNP	0.152	0.167	0.161	0.167	0.108
pFFA	0.123	0.141	0.122	0.130	0.083
TPD	0.142	0.159	0.135	0.133	0.082

Table 4.3: Energy disorder of electrons computed using the protocols introduced in Tab. 4.1

	Energy disorder of electrons σ [eV]				
	full QM	QM one shell only	hybrid large	hybrid small	semi-empirical
Alq$_3$	0.220	0.236	0.223	0.197	0.185
α-NPD	0.099	0.120	0.093	0.091	0.094
mBPD	0.140	0.159	0.143	0.151	0.150
DEPB	0.105	0.113	0.096	0.101	0.099
NNP	0.104	0.121	0.098	0.094	0.102
pFFA	0.102	0.133	0.097	0.096	0.091
TPD	0.157	0.177	0.161	0.147	0.108
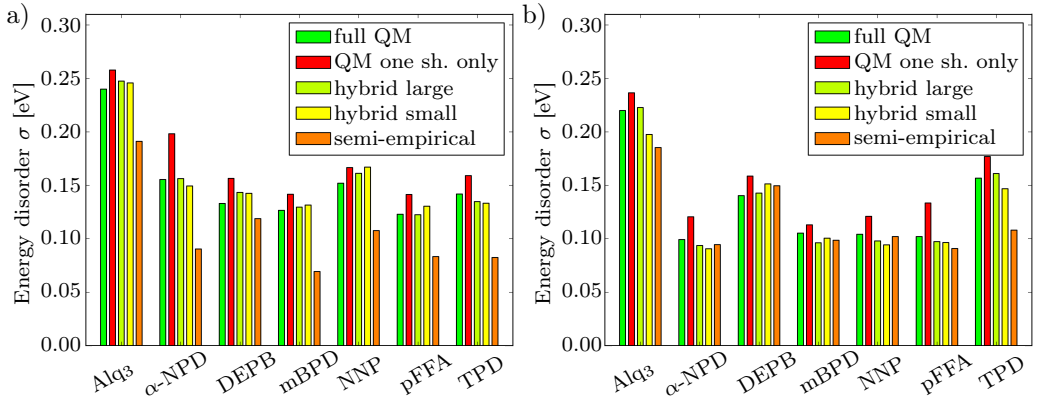
Figure 4.5: Energy disorder of a) holes and b) electrons in seven different materials. The methods used for the calculation of energy disorder are described in the text. To reproduce the results of the full QM reference method, the hybrid large method is found to be most appropriate. The image is taken from Friederich *et al.* [129].

materials.

The "full semi-empirical" algorithm systematically underestimates the energy disorder of holes. For electrons in α-NPD, mBPD, and NNP, it yields results within 6 % of the "full QM" results. A possible source of error in this method is the minimal basis sets used in the semi-empirical DFTB calculations. This might cause underpolarization [168] especially of the charged species and therefore lead to a wrong description of electrostatic effects. This implies that the energies of the charged molecules cannot be reliably predicted with exclusive use of semi-empirical methods. As an example, the deviation of energy differences between DFT and DFTB for 300 Alq$_3$ pairs is ± 0.142 eV for positively charged molecules and ± 0.108 eV for negatively charged molecules. This leads to large discrepancies between the energy disorder calculated with the "full QM" and the "semi-empirical" method.

Tab. 4.2 and 4.3 show values of the energy disorder of all materials and methods tested. For completeness, the results of the charged Quantum Patch method were compared to energy disorder computed with the faster, neutral Quantum Patch method. The results of this study are shown in Tab. 4.4. The purely semi-empirical method yields deviations from the "full QM" methods, which vary between $+12$ % for α-NPD electron disorder and -30 % for TPD hole disorder. In contrast to the charged Quantum Patch method, splitting of the neutral system into DFT and semi-empirical parts is not possible. Therefore, the neutral Quantum Patch

Table 4.4: Comparison of the energy disorder calculated using the neutral Quantum Patch method (see Chapter 3.2.2) performed on a DFT ("full QM") and DFTB ("semi-empirical") level.[a]
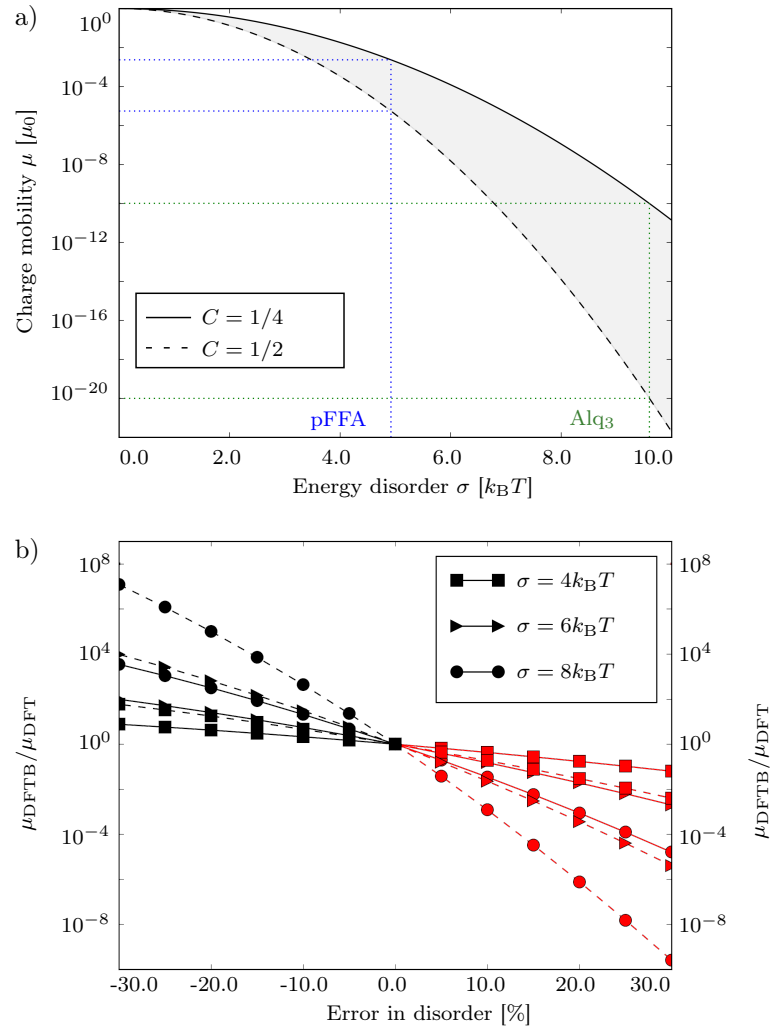
	Energy disorder σ [eV]			
	full QM		semi-empirical	
Alq$_3$	0.224	0.239	0.212	0.204
α-NPD	0.144	0.111	0.107	0.125
mBPD	0.130	0.131	0.140	0.140
DEPB	0.109	0.120	0.083	0.128
NNP	0.135	0.112	0.138	0.116
pFFA	0.112	0.102	0.089	0.109
TPD	0.129	0.157	0.093	0.155

[a] Deviations of up to 30 % in energy disorder depending on the used calculation methods along with no simple way to "hybridize" the polarization approach with obvious CPU-time savings made usage of DFTB within this approach unfavorable.

method does not allow for hybrid implementations.

In order to estimate if the hybrid implementations of the Quantum Patch method are accurate enough to be used for predictive simulations, the influence of deviations of the energy disorder on the charge carrier mobility has to be evaluated. Therefore, the sensitivity of the charge carrier mobility on positive or negative deviations of the energy disorder is shown in Fig. 4.6. The exponential dependence of the mobility on the energy disorder results in order of magnitude changes of mobility even at small errors in energy disorder. Therefore, apart from the "full QM" method, only the "hybrid large" method will be used in in the following chapters.

To better understand the reason of the hybrid approach to work or fail in some cases, a direct comparison between DFT and DFTB calculations for a few relevant quantities was performed. Typical DFT derived dipole moments of neutral Alq$_3$ molecules in vacuum are $d_{\mathrm{DFT}} = (4.9 \pm 0.9)\,\mathrm{Debye}$, whereas the dipole moments in DFTB of the same set of molecules are $d_{\mathrm{DFTB}} = (4.2 \pm 0.8)\,\mathrm{Debye}$. Thus, the energy disorder will slightly be underestimated in the semi-empirical methods. This can explain the deviations of the "hybrid small" and "hybrid large" method but it is not sufficient to understand the deviations of the "semi-empirical" method.

Figure 4.6: a) Exponential dependence of the charge carrier mobility μ on the energy disorder σ for $C = 1/2$ and $C = 1/4$ (see discussion in Appendix E). As an example, the energy disorder of two specific materials (pFFA and Alq$_3$) is shown in the plot. b) Positive and negative shifts of the energy disorder of up to $\pm 30\%$ lead to changes in charge carrier mobility of between 5 and 10 orders of magnitude, depending on the prefactor C. Larger ratios of μ_{DFTB} and μ_{DFT} are observed for the larger C parameter (dashed lines) and for a larger energy disorder σ (circles). The image is taken from Friederich *et al.* [129].

For the positively charged Alq$_3$ molecules in vacuum, the center of charge differs by only 0.36 ± 0.17 Å between DFT and DFTB, indicating a method independent electronic structure. Thus, the differences between DFT and DFTB lie in the evaluation of energies rather than in the charge density itself. Therefore, total energy differences between neighboring molecules were tested. For reliable results, the total energy difference of two molecules is expected to be independent of the calculation method. This corresponds to a small difference of the total energy differences $\delta\Delta E$ calculated using different methods. However, for positively charged Alq$_3$ molecules, this difference is $\delta\Delta E = \pm 0.43$ eV. This indicates that while DFTB seems to captures the charge density itself very well, there are large discrepancies in the evaluation of the molecular energy differences. As the primary interest of hybrid implementations of the Quantum Patch method is the reproduction of the "full DFT" results, these observations justify the "onion" type model of the "hybrid large" method, where a number of radial cutoffs for DFT (especially the inner part where the total energies are relevant) and DFTB (focusing mainly on a realistic long range electrostatic background) is used.

In the next chapter, the energy disorder values obtained in this chapter are combined with other microscopic molecular properties such as electronic couplings and reorganization energies to obtain a quantitative estimate of the charge carrier mobility in different materials. This next step will show the applicability of the multiscale modeling approach for a quantitative and parameter-free prediction of macroscopic properties such as the charge carrier mobility.

4.4 Charge carrier mobility in amorphous organic systems: Prediction and validation

In Chapter 4.3, the energy disorder of a range of materials was calculated using the Quantum Patch method and a hybrid extension to this method. In this chapter, the results of the neutral Quantum Patch method (see Tab. 4.4) will be used for the prediction of the hole mobility of nine different materials. The results are compared to the experimental hole mobility available in literature to validate the applicability and accuracy of the multiscale modeling approach. Chapter 4.4 and 4.5 are based on work reported in Friederich *et al.* [131]. Figures and parts of the discussion are adopted from this publication.

4.4.1 Marcus parameters

The mobility of nine different materials is computed using the multi-scale simulation approach illustrated in Fig. 3.1. Firstly, atomistically resolved morphologies of the materials in an amorphous solid phase are generated. In this step, molecular dynamics simulations are performed to generate amorphous morphologies of the size of 300 molecules. Periodic boundary conditions (see Chapter 3.1.2) allow a periodic extension of the systems in all dimensions. The final morphologies of Alq_3, α-NPD, DEPB, mBPD, NNP, pFFA and TPD (see Fig. 4.1) show a disordered structure without any indications of crystalline domains. Crystalline structures of pentacene and tetracene are obtained from Schiefer *et al.* [169]. After morphology generation, the electronic structure of the molecules in the amorphous system is characterized using the neutral Quantum Patch method on periodically extended structures incorporating approximately 5000 molecules as embedding. Pairwise electron and hole coupling matrix elements (J_{if}) for approximately 600 molecular pairs, reorganization energies (λ_{if}) and site energy differences (ΔE_{if}) including polarization and conformational disorder are computed. The Quantum Patch approach permits an *ab initio* characterization of polarization effects, which are critical to accurately describe the energy disorder of amorphous systems. The inner part of the reorganization energy λ is calculated based on Nelsens four point procedure [64].

The hopping matrix elements J_{if} between each molecule and all of its neighbors are calculated based on the Löwdin orthogonalization procedure [61, 62] using the highest occupied molecular orbitals (HOMO). In this procedure, frontier orbitals as well as Fock- and overlap matrices are extracted from monomer and dimer calculations in a sufficiently large embedding environment. Using this procedure, a distance dependent distribution of hopping matrix elements is obtained using molecular dimers extracted from large disordered morphologies. For completeness, a similar procedure was applied to the lowest unoccupied molecular orbitals (LUMO). These LUMO levels are in first approximation responsible for electron transport while the HOMOs are used to estimate the hole mobility.

Statistical averages of these microscopic material characteristics are used as input for the generalized effective medium model (GEMM) [14] shown in Eq. 2.17. In this model, the mobility is obtained from an approximative solution of the master equation using an effective medium model (see Chapter 2.1.4). According to the GEMM model, the charge carrier mobility depends on the mean number of nearest-neighbor molecules M, averages over the hopping matrix elements and distances ($\langle J^2 r^2 \rangle$) and averaged reorganization energies (λ).

78

4.4.2 Charge carrier mobility and microscopic analysis

Fig. 4.7 shows the comparison between the computed hole mobility and experimental data of the materials presented above. The corresponding microscopic parameters (energy disorder in Fig. 4.8, electronic couplings in Fig. 4.9 and reorganization energies in Fig. 4.10) are summarized in Tab. 4.5. As shown in Fig. 4.8a, the distributions of polaron energies are well described by Gaussian distributions [52, 53]. The width of the distribution of on-site energies crucially influences the Marcus hopping rates. Fig. 4.8a shows the distributions of energy levels of two specific materials, NNP and pFFA. NNP has a 21 % larger energy disorder than pFFA. This corresponds to a decrease in hole mobility of one order of magnitude, even though the remaining microscopic parameters are quite comparable. Fig. 4.9a depicts the distance dependence of the electronic coupling matrix elements of two molecules, namely Alq_3 and pFFA. Alq_3 is a compact "sphere-like" molecule with a narrow distribution of hopping matrix elements, which decays exponentially with distance. pFFA, a more extended and flexible molecule, shows a rather diffuse and wide-spread distribution of coupling matrix elements. This leads to an overall reduction of $\langle J^2 r^2 \rangle$ by an order of magnitude ($\langle J^2 r^2 \rangle = 9.99 \cdot 10^{-3}\,\mathrm{eV}^2\mathrm{Å}^2$ for Alq_3 vs. $\langle J^2 r^2 \rangle = 1.46 \cdot 10^{-3}\,\mathrm{eV}^2\mathrm{Å}^2$ for pFFA, see Tab. 4.5 and Fig. 4.9b). As the mean electronic coupling $\langle J^2 r^2 \rangle$ only enters the calculation of charge carrier mobility in the prefactor (see Eq. 2.17), it only linearly influences the charge mobility. The parameter responsible for the much lower mobility of Alq_3 compared to *e.g.* pFFA is the comparatively large energy disorder σ of Alq_3.

In addition to the microscopic properties required for the calculation of charge carrier mobility, the energy levels of molecules in the disordered system were analyzed. These are of crucial importance for the device architecture as holes and electrons have to be injected or extracted from the respective materials. Fig. 4.11 shows the HOMO levels and the ionization potentials of all tested materials. These energies were calculated for molecules in vacuum as well as for molecules embedded in a self-consistently evaluated electrostatic environment.

### 4.4.3 Frozen-dihedral approximation

In many publications [68, 86, 90], the reorganization energy has been calculated in vacuum, where a full relaxation of the molecule is possible. Such complete conformational freedom is not realistic for condensed systems, where the molecules are confined by their individual confinement. The internal degrees of freedom which are strongly affected by this confinement are dihedral rotations. In order to avoid an overestimation of the internal reorganization energy in the condensed phase, a novel procedure was developed and implemented in this work. In this
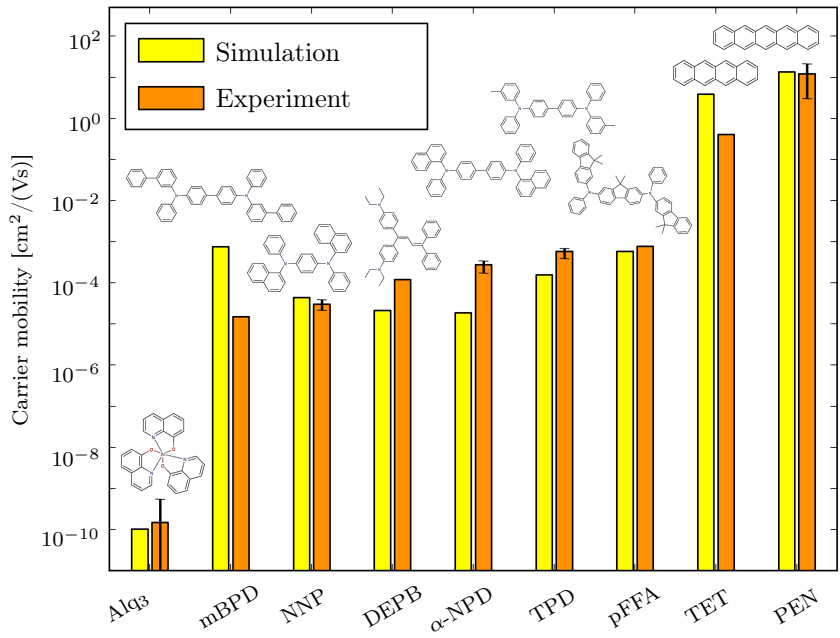
Figure 4.7: a) Comparison of the hole mobility of nine different organic semiconductors (see Chapter 4.2) varying from Alq₃ with a comparatively low hole mobility to highly conducting crystalline materials, such as tetracene and pentacene. Predictions from the multiscale workflow are in agreement with experiment within one order of magnitude for all materials. The image is taken from Friederich *et al.* [131].
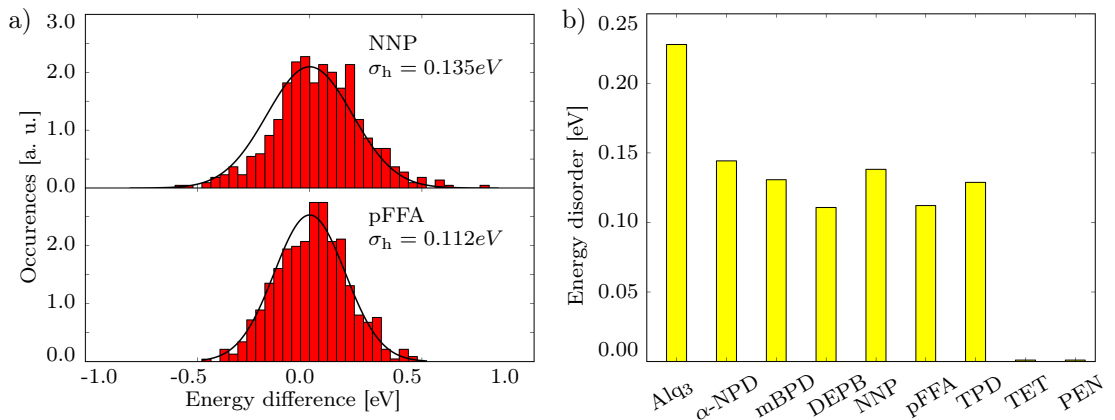
Figure 4.8: Panel a) shows the distribution of energy differences computed with the Quantum Patch method for NNP and pFFA. The widths of the distributions define the energy disorder σ. Panel b) shows the energy disorder of holes in the nine materials. The image is taken from Friederich *et al.* [131].
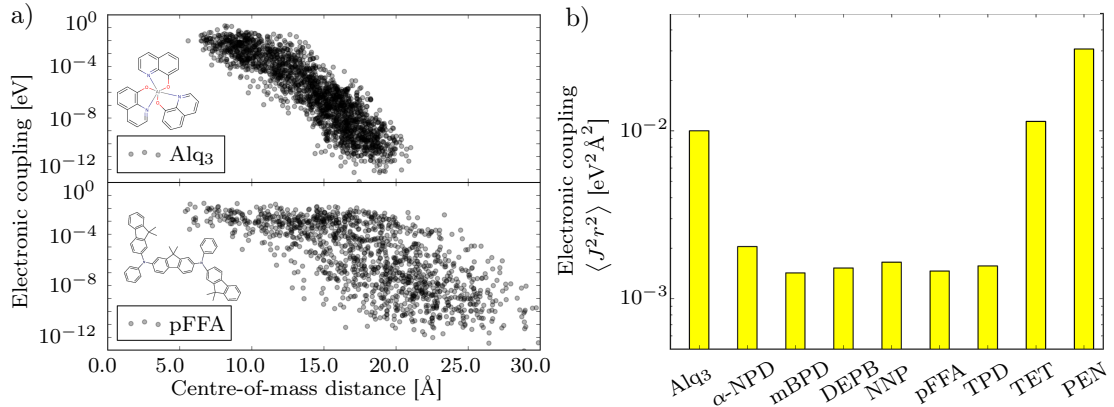
Figure 4.9: Panel a) shows the electronic couplings J as a function of the molecular distance in systems of the compact Alq$_3$ and the more extended pFFA molecule. Panel b) shows the mean of the electronic couplings between HOMO orbitals for all studied materials (see Tab. 4.5). The image is taken from Friederich *et al.* [131].
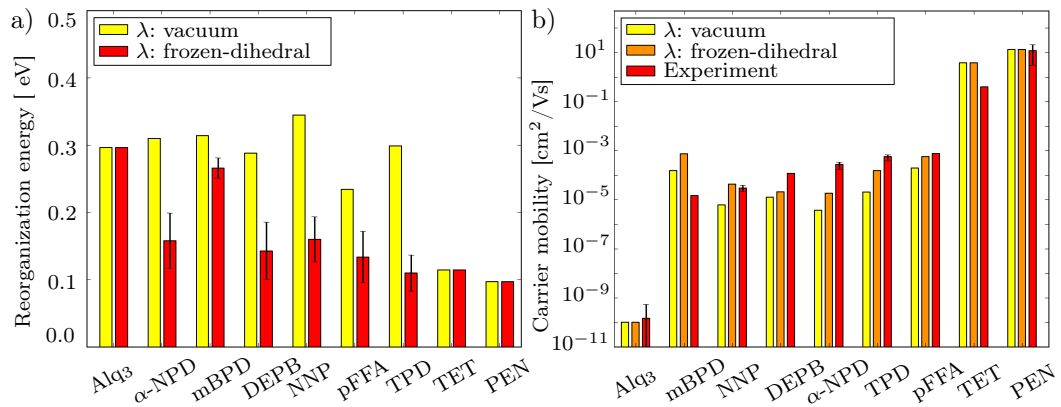

Figure 4.10: Panel a) shows reorganization energies calculated in vacuum (yellow) and using the frozen-dihedral approximation (red). It can be observed that for the molecules with flexible dihedral angles, the mean reorganization energy considerably decreases when the frozen-dihedral approximation is used. The error bars indicate the range of reorganization energies of molecules embedded into their individual matrix. Panel b) shows the impact of the frozen-dihedral approximation on charge carrier mobility. A better agreement with experiment is achieved for the frozen-dihedral approximation compared to the full vacuum relaxed reorganization energies. The image is taken from Friederich *et al.* [131].

Table 4.5: Microscopic input parameters required by the GEMM model to calculate the charge carrier mobility of the different materials. The energy disorder σ is split into two contributions, namely the conformational disorder σ_i and the electrostatic disorder σ_p. This segmentation as well as the quantity $\Delta E_\mathrm{int,HOMO}$ will be explained in the Chapter 4.5.

	σ [eV]	σ_i [eV]	σ_p [eV]	$\Delta E_\mathrm{int,HOMO}$ [eV]	$\langle J^2 r^2 \rangle$ [eV^{2}Å^2]	M	λ [eV]
Alq$_3$	0.224	0.166	0.151	-	$9.99 \cdot 10^{-3}$	7.31	0.296
mBPD	0.110	0.080	0.075	0.186	$1.52 \cdot 10^{-3}$	8.52	0.143
NNP	0.135	0.137	-	0.431	$1.64 \cdot 10^{-3}$	7.65	0.160
DEPB	0.130	0.086	0.098	0.272	$1.42 \cdot 10^{-3}$	8.16	0.266
α-NPD	0.144	0.126	0.070	0.250	$2.04 \cdot 10^{-3}$	7.73	0.158
TPD	0.129	0.097	0.084	0.197	$1.56 \cdot 10^{-3}$	8.49	0.110
pFFA	0.112	0.100	0.049	0.366	$1.46 \cdot 10^{-3}$	7.70	0.134
TET	0.0	0.0	0.0	-	$1.13 \cdot 10^{-2}$	15.8	0.114
PEN	0.0	0.0	0.0	-	$3.07 \cdot 10^{-2}$	15.8	0.097

Table 4.6: The simulated hole mobility in the second column exponentially depends on the disorder strength σ and the frozen-dihedral reorganization energy λ shown in Tab. 4.5. The prefactor is a function of $\langle J^2 r^2 \rangle$ incorporating the hopping matrix elements J and the hopping distance r. The third and fourth columns give literature values and sources of the experimental hole mobility.

	$\mu_\mathrm{sim.}$ [cm^2/(Vs)]	$\mu_\mathrm{exp.}$ [cm^2/(Vs)]	Source
Alq$_3$	$1.01 \cdot 10^{-10}$	$1.46 \cdot 10^{-10}$	[160, 162, 163, 170, 171]
mBPD	$7.38 \cdot 10^{-4}$	$1.49 \cdot 10^{-5}$	[165]
NNP	$4.31 \cdot 10^{-5}$	$2.99 \cdot 10^{-5}$	[172]
DEPB	$2.09 \cdot 10^{-5}$	$1.17 \cdot 10^{-4}$	[173]
α-NPD	$1.84 \cdot 10^{-5}$	$2.70 \cdot 10^{-4}$	[160, 164]
TPD	$1.52 \cdot 10^{-4}$	$5.74 \cdot 10^{-4}$	[160, 163, 173, 174]
pFFA	$5.70 \cdot 10^{-4}$	$7.60 \cdot 10^{-4}$	[165]
TET	3.83	0.4	[175]
PEN	13.35	3.0/21	[176, 177]
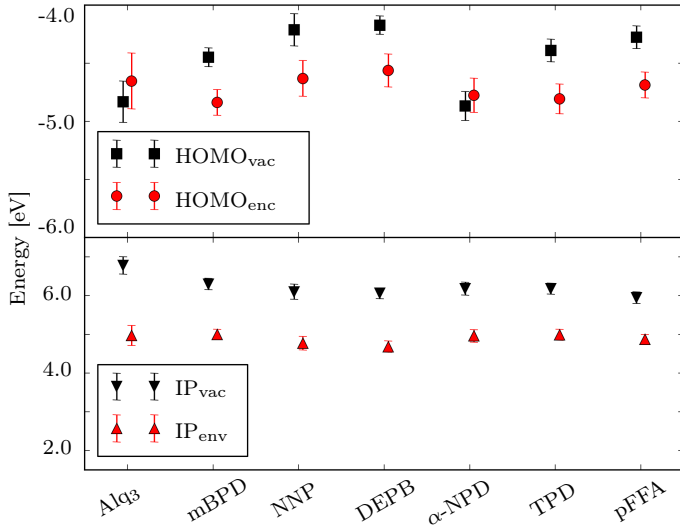
Figure 4.11: HOMO energy levels and ionization potentials in vacuum and environment. The image is taken from Friederich *et al.* [131].

frozen-dihedral approach, reorganization energies in the solid phase are calculated while constraining the dihedral angles of each molecule to the values observed in the disordered morphology. Only relaxation of other degrees of freedom such as breathing modes and angle-relaxations are permitted, which do not result in large-scale conformation changes [178].

The effect of fixed dihedral angles can be observed in the analysis of the hole mobility of different materials in Fig. 4.10a. The reorganization energies systematically decrease up to 55% for NNP. Fixing dihedral angles is still a rough approximation to the relaxation processes, which might lead to an underestimation of the reorganization energy. Considering that the full vacuum relaxation will overestimate the inner part of the reorganization energy, the frozen-dihedral approximation can be considered as a lower limit. The two methods can thus be used as upper and lower bound of reorganization energies. Fig. 4.10b shows that the observed agreement with experimental data can only be achieved if the reorganization energies are evaluated in the frozen-dihedral approximation. More exact reorganization energies can be obtained using full quantum mechanical embedding procedures, where explicit intermolecular exchange and correlation effects are taken into account. QM/MM methods can also elucidate this problem further.

4.5 Molecular origin of the charge carrier mobility

To systematically improve material properties, it is necessary to fully understand the relations between molecular and macroscopic properties. As shown in the last section, the simulation approach used in this work is able to calculate and predict the charge carrier mobility of amorphous materials without parameterization or experimental input. Therefore, it can be used to systematically investigate the molecular origin of charge carrier mobility by identification of causal correlations between molecular properties and charge mobility. The first step in this process is the decomposition of the charge mobility in factors which depend on different molecular properties. This procedure will be presented in Chapter 4.5.1. Afterwards, the factors with strongest influence on charge carrier mobility will be analyzed and related to molecular properties. These factors include the electrostatic disorder, which is mainly determined by molecular dipole moments (see Chapter 4.5.2) and the internal or conformational disorder due to molecular distortions in the amorphous solid state (see Chapter 4.5.3). Using these two quantities, it is possible to derive design rules, which will be applied in Chapter 4.6. Before that, correlations effects will be studied in Appendix F. These correlations can also influence macroscopic transport properties. The figures and parts of the discussion in this chapter are adopted from Friederich *et al.* [131].

4.5.1 Mobility factorization

To analyze the molecular properties which determine the charge carrier mobility, the GEMM model in Eq. 2.17 is decomposed as

$$\log \mu = \log \mu_0 - C\beta\lambda - C\beta^2(\sigma_i^2 + \sigma_p^2) \tag{4.1}$$

where μ_0 is the prefactor and C is the C-factor discussed in Appendix E. The energy disorder σ is decomposed into an intrinsic component σ_i and a polarization component σ_p. The intrinsic contribution σ_i arises from the molecular distortions due to packing, *i.e.* conformational disorder, whereas the polarization part σ_p arises from the individual electrostatic environment of each molecule. The physical nature of these two sources of disorder is fundamentally different. Thus, they can be treated in first approximation as uncorrelated quantities. This means that the square of the width of the full energy disorder σ is the sum of the individual contributions:

$$\sigma^2 = \sigma_i^2 + \sigma_p^2 \tag{4.2}$$

84

The intrinsic component of the energy disorder is directly extracted from Quantum Patch calculations by computing the single molecule energy level variance of molecules without electrostatic environment effects. Based on that, the polarization contribution $\sigma_{\mathrm{p}}^2 = \sigma^2 - \sigma_{\mathrm{i}}^2$ can be computed indirectly. It represents the electronic (polarization) effect of the environment.

Fig. 4.12 shows the decomposition of the molecular contributions of the charge carrier mobility. The mobility μ_0 (blue bars) can be obtained when only the prefactor of Eq. 4.1 is taken into account. It can be interpreted as the mobility of a fictional material comprised of electrostatically non-interacting molecules with equal conformations and reorganization energy. This mobility μ_0 is of the same order of magnitude for all disordered materials studied in this work. The crystalline materials tetracene and pentacene (not shown in the graph) show a value of μ_0 which is approximately one order of magnitude higher compared to the disordered materials. The reason for that are the higher average coupling matrix elements in the crystalline structure of these polycyclic hydrocarbons. The μ_0 values of the amorphous compounds provide an order-of-magnitude estimate of the maximal possible mobility of amorphous small-molecule organic semiconductors. Reorganization and energy disorder due to dipole moments and molecular flexibility lead to values of charge carrier mobility which are orders of magnitude lower.

4.5.2 ELECTROSTATIC DISORDER

A first reduction of the maximum mobility μ_0 arises from the reorganization energy λ. This reorganization-related reduction is to some extend not avoidable in materials with localized polarons. However, the impact of reorganization on the charge mobility (green bars) is smaller than one order of magnitude. Differences in the reorganization energy of the materials therefore only play a minor role. As mentioned above, the most dominant contributions to charge carrier mobility are electrostatic and conformational disorder. As discussed in literature [179], the electrostatic polarization (yellow bars) plays a major role in determining the mobility of amorphous materials. In agreement with arguments made by Bässler and others [75, 179], a correlation between molecular dipole moments, disorder parameters and charge carrier mobility can be observed. This correlation is illustrated in Fig. 4.13a.

Even though the small polaron model might not be fully appropriate to describe charge transport in crystal structures of rigid molecules, it is interesting to consider pentacene and tetracene as low-disorder reference materials in this approach. A consequence of low disorder, charge transport in these materials is dominated by reorganization energy and the electronic coupling elements. The experimental
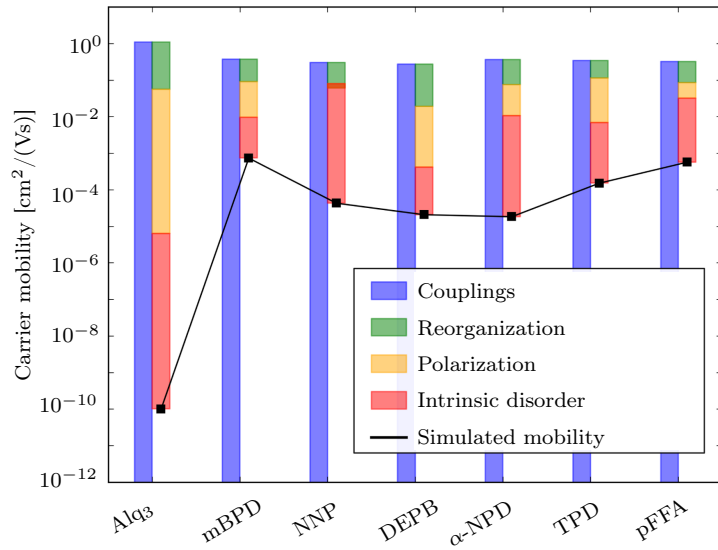
Figure 4.12: Decomposition of the hole mobility in four parts: The disorder and reorganization energy independent part μ_0 is shown as blue bars. This maximum mobility is reduced by the influence of reorganization energy (green) and energy disorder. Disorder contributions are subdivided into electrostatic disorder (yellow) and conformational disorder (red). For most of the amorphous HTL materials (mBPD-pFFA), the largest reduction of μ_0 arises from intrinsic conformational disorder. The image is taken from Friederich *et al.* [131].

Table 4.7: Analysis of the average molecular dipole moments in vacuum ($|\vec{d}_{\mathrm{vac}}|$) and within a self-consistently evaluated amorphous structure ($|\vec{d}_{\mathrm{p}}|$).

	$|\vec{d}_{\mathrm{vac}}|$ [Debye]	$|\vec{d}_{\mathrm{p}}|$ [Debye]
Alq$_3$	4.9 ± 0.9	6.2 ± 1.4
mBPD	1.5 ± 0.7	1.7 ± 0.8
NNP	1.4 ± 0.6	1.7 ± 0.7
DEPB	2.8 ± 0.8	3.3 ± 1.0
α-NPD	1.3 ± 0.7	1.8 ± 1.2
TPD	1.5 ± 0.7	1.7 ± 0.7
pFFA	1.8 ± 0.8	2.0 ± 0.9

hole mobility of pentacene shown in Fig. 4.7a is obtained from experiments using thin-film transistors ($\mu = 3\,\mathrm{cm^2/(Vs)}$ [176]) as well as from THz experiments ($\mu = 21\,\mathrm{cm^2/(Vs)}$ [177]). The simulations used for the calculation of hole mobility are based on an idealized, crystalline system. Therefore, these simulations yield a hole mobility of $\mu = 13\,\mathrm{cm^2/(Vs)}$ which is larger than the thin-film transistor mobility, where grain boundaries play an important role. The calculated charge mobility is closer to the value observed in THz experiments [177]. Nonetheless, it is not possible to judge whether the model of activated hopping transport is fully applicable without analysis of the temperature dependence of the charge carrier mobility. In case of activated transport, mobility increases with temperature while in case of delocalized states or even band transport, the mobility decreases due to increased electron phonon interaction and scattering.

For a rough estimate of the electrostatic energy disorder, it is useful to calculate either molecular dipole moments in vacuum or equilibrated dipole moments in an amorphous system. In Tab. 4.7, the average dipole moments of the molecules both in vacuum and in the morphology are shown. The dipole strength leads to electrostatic interaction and therefore polarization disorder which can be roughly estimated using *e.g.* the work by Young *et al.* [72]. Here, the energy disorder σ_{p} is estimated using a dipole lattice model which requires the average dipole moment, the relative permittivity and the density of the molecules. Alq$_3$ exhibits a large intrinsic dipole moment (approximately 5 Debye). The high polarization disorder caused by these dipole moments leads to the lowest mobility among the materials studied, which indicates that the intrinsic molecular dipole has to be minimized when designing new materials.
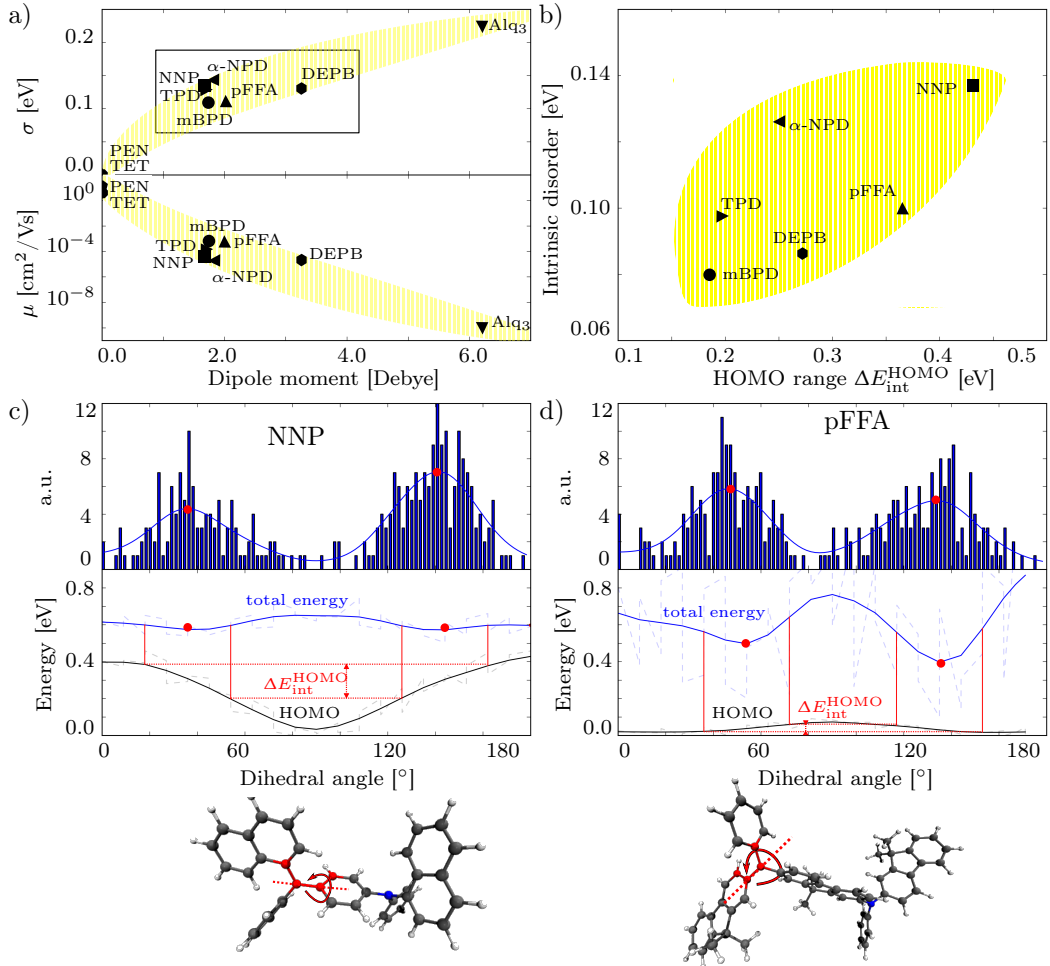
Figure 4.13: Panel a) shows the correlation between energy disorder (upper panel) and hole mobility (lower panel). It uses the equilibrated dipole moments of the molecule in the amorphous structure. The HTL molecules in the frame are analyzed in panel b). This panel depicts the correlation between the intrinsic energy disorder σ_i and the HOMO energy variance $\Delta E_{\mathrm{int,HOMO}}$. Panels c) and d) show the variation of the total energy (blue lines) for NNP (c) and pFFA (d) of the dihedral angles indicated in red. This variance determines the degree of distortion which occur in disordered thin films. The top panels show the degree of distortion found for the specific dihedral angle in the amorphous material. The HOMO energy variance, defined in the bottom panel varies significantly from molecule to molecule. A large HOMO energy variance (see panel b) and text) can lead to a higher degree of intrinsic disorder and hence a lower mobility. The image is taken from Friederich *et al.* [131].

4.5.3 CONFORMATIONAL DISORDER

The molecules mBPD - pFFA (indicated in the frame in Fig. 4.13b) have small intrinsic dipole moments (1.5 to 4 Debye) and therefore only weak electrostatic disorder. Nonetheless, they show large variations in total disorder σ and hole mobility. This variation arises from the second contribution to energy disorder and mobility, which is the intrinsic (conformational) disorder σ_i. This quantity is connected to distortions of molecules in amorphous systems (see Fig. 4.12). The conformational disorder contribution dominates the variation of the hole mobility for all non-crystalline materials with small dipole moment, *i.e.* typical HTL materials as indicated in the frame in Fig. 4.13a.

To investigate the impact of conformational variations on the site-energies and the energy disorder, the geometry of molecules in disordered films was analyzed. The molecular position and conformation in the bulk is the result of a minimization of the molecular total energy including inter-molecular interactions. A trade-off between improved alignment with neighboring molecules and internal distortions leads to energy and conformational variations of the molecules. As already discussed in Chapter 4.4.3, the lowest-energy degrees of freedom of many molecules are rotations of dihedral angles. These significantly change the molecular shape at low excitation energies. Distortions of the molecular geometry almost always lead to changes of ionization potential and hole energy, which can be approximated by changes of the HOMO energies. Panels b-d of Fig. 4.13 illustrate the HOMO energies as well as molecular total energies as functions of single, arbitrarily chosen dihedral angles. HOMO distributions resulting from rotations around other dihedral angles show analogue behavior.

To develop a quantitative and molecule specific model for the origin of the intrinsic disorder contribution in organic materials, the distributions of dihedral angles of the molecules in the amorphous morphologies were analyzed. These distributions are shown in the top panels of Fig. 4.13c and 4.13d for the molecules NNP and pFFA. In the bottom panels, variations of the total energy and the HOMO energy of the corresponding molecules as a function of the dihedral angle are shown. These energies were computed DFT calculations in the gas phase. The maximum of the dihedral angle distribution agrees with the minimum of the total energy profile. The width of the distribution for both molecules is comparable. However, a significant difference in the variance of HOMO energies is observed when comparing NNP and pFFA. While the HOMO energy of pFFA is nearly independent of the specific dihedral angle, the NNP HOMO energy strongly varies as a function of the angle. This difference in orbital energy variation for NNP and pFFA leads to drastic differences in the internal disorder contribution σ_i, (0.14 eV

vs. $0.10\,\text{eV}$) which strongly influences the hole mobility of the respective materials $(0.4 \cdot 10^{-4}\,\text{cm}^2/(\text{Vs})$ vs. $5.7 \cdot 10^{-4}\,\text{cm}^2/(\text{Vs}))$. This effect directly correlates single molecule properties with the macroscopic charge mobility. To quantize its size, $\Delta E_{\text{int,HOMO}}$ is defined as the range of the HOMO energy at dihedral angles close to the total energy minimum ($\Delta E_{\text{int,HOMO}} = 0.43\,\text{eV}$ vs. $0.37\,\text{eV}$ for NNP and pFFA, see Tab. 4.5). The quantity $\Delta E_{\text{int,HOMO}}$ was computed using an evaluation of all dihedral rotations of a molecule in vacuum while relaxing all other dihedral angles. The largest and smallest HOMO energies within an interval of $\pm 20\,°$ around the total energy minima of all dihedral potentials were used as upper and lower bounds for the calculation of $\Delta E_{\text{int,HOMO}}$.

Extending this analysis to all HTL materials (Fig. 4.13b) yields a correlation between $\Delta E_{\text{int,HOMO}}$ and the internal energy disorder. This indicates that the variation of HOMO energies in energetically accessible molecular conformations can be used as an indicator of conformational disorder and therefore charge carrier mobility of common HTL materials. A relationship between molecular conformations and energy disorder was already suggested in literature but could not be fully quantified for realistic systems [100, 180]. While the observations shown in this section do not fully address the differences between experimental and theoretical charge mobility, it is nonetheless a significant step toward *in silico* molecule design. Furthermore, the single molecule indicators of energy disorder, namely dipole moment and HOMO variation $\Delta E_{\text{int,HOMO}}$, can be used as a fast single-molecule based screening and selection technique of the chemical compound space. In Chapter 4.6, an extension of this method will be used for targeted molecule design.

4.6 Improvement of the electron mobility of Alq$_3$ by rational materials design

Attempts to improve the charge mobility of amorphous organic semiconductors to date mainly rely on costly experimental efforts to test and find new materials. This chapter shows a systematic study using the parameter-free multiscale prescreening tool presented in the Chapter 3 on the way to rational design of organic electronics components. The capability of *in silico* molecule design is demonstrated by systematically improving the electron mobility of hydroxyquinoline based aluminum complexes leading to the prediction of a new molecule with increased electron mobility. SCLC measurements confirm this increase of electron mobility of three orders of magnitude compared to the established Alq$_3$ compound. In addition to that, design rules are deduced which can generally be applied to organic semiconductors. These design rules include a controlled modification of energy levels, which are crucial for charge transport across materials interfaces and injection. Secondly, guidelines are provide to systematically decrease intermolecular electrostatic interaction and energy disorder and thus increase charge mobility.

From the very initial stages of development of organic electronics [181], Alq$_3$ (Tris-(8-hydroxyquinoline)aluminum) has established itself as a standard electron transporting layer (ETL), most prominently used in organic light emitting diodes [182, 183]. Alq$_3$'s stability as well as synthetic simplicity have tremendously contributed to its general acceptance. However, its electron mobility of $1.1 \cdot 10^{-10}$ to $3.7 \cdot 10^{-7}\,\mathrm{cm^2/(Vs)}$ [160, 162, 164, 170, 171, 184] is several orders of magnitude lower than typical hole transporting layer, e.g. α-NPD [160, 164]. This has brought improvement attempts to the focus of the organic electronics community rather early on. Improvement of the charge carrier mobility is directly connected to the efficiency of an OLED as higher charge mobility leads to lower resistivity and power consumption of the device. Therefore, several different ideas to improve the conductivity of organic semiconductors have been proposed in the literature. Some of the most prominent attempts comprise doping with small molecule dopants. At the same time, many theories and models were developed describing charge transport in disordered organic semiconductors using various different techniques. These include the early analytical works of Bässler et al. [52, 75], extensions to these models [49, 70, 95, 134, 185], KMC techniques [48] and multiscale modeling approaches [68, 90, 126, 127, 131]. Despite all of this work, so far no systematic example of *in-silico* design of new organic semiconductors has been shown.

4.6.1 Simulation protocol

In order to theoretically predict the charge carrier mobility and other material properties such energy levels, the multiscale simulation approach presented in chapter 3.1 is used. For the calculations presented in this chapter, the following steps were applied. *In silico* morphology generation of thin films using the Deposit method presented in chapter 3.1.2 [12] is followed by density functional theory (DFT) based analysis of the molecules within their unique local environment using the Quantum Patch method presented in chapter 3.2 [68, 129]. The bulk electron mobility is then estimated using the analytical Generalized Effective Medium Model (GEMM) (see chapter 2.2.3) [14].

In more detail, the geometries of the molecules are optimized using DFT calculations. If required, internal dihedral rotations are parameterized for the following force-field based morphology generation. The geometry and partial charges obtained in DFT are required by the simulated annealing Monte Carlo protocol Deposit [12] (see Chapter 3.1.2). With this protocol, atomistic morphologies consisting of 1000 molecules per system were generated. The morphologies are periodically extended in x- and y-direction and used as input for the electronic structure calculations. Here, the energy disorder of the system is calculated by evaluating the site energies for additional electrons and holes in the system explicitly using the charged Quantum Patch method. Polarization effects due to intermolecular interaction and polaron effects are treated self-consistently in a quantum mechanical way. Electronic couplings were calculated using the Löwdin orthogonalization [61, 62] in electrostatically self-consistent, neutral systems. From these systems, the dipole moments of molecules embedded in the morphology are extracted. As shown in Chapter 4.4, they can drastically deviate from ground-state dipole moments of molecules in vacuum. Reorganization energies are estimated using Nelsen's four-point-procedure [64]. Site energies as well as energy disorder, electronic couplings and reorganization energies are used in an effective medium model (Chapter 2.2.3) to estimate the zero-field electron mobility.

4.6.2 Mobility prediction

Using this multiscale approach, the electron mobility of a set of materials (see Fig. 4.14a-e) is calculated, including the well-known Alq_3 and various new aluminum complexes derived from Alq_3. Using the molecules shown in Fig. 4.14a-d, design rules are derived to systematically enhance electron mobility. These rules were applied to develop the materials shown in Fig. 4.14e. The predicted electron mobilities of these compounds outperform the electron mobility of Alq_3 by

up to three orders of magnitude (Fig. 4.14f). To test the theoretical predictions, the most promising candidate Alq_2MHept was synthesized at the Institute of Nanotechnology (INT) at KIT by Dr. Verónica Gómez. Space charge limited current (SCLC) mobility measurements performed at the Light Technology Institute (LTI) at KIT by Michael Jenne and Christian Sprau confirmed the theoretically predicted electron mobility. The design rules as well as the experimental findings will be presented in this chapter.

For the utilization of a material in an *e.g.* OLED device, the on-site energy levels for electrons and holes in the respective material are of crucial importance for charge injection and the required driving voltage. For electron conducting materials, the electron affinity (EA) has to be in close alignment with the Fermi level of the electron injecting electrode. If the EA is lower, injection is hindered by an injection barrier leading to an increase of on-set voltage of the device and a decrease in efficiency. In case of a too high EA, a certain part of the energy is transferred to molecular vibrations leading to a loss in efficiency.

The results for HOMO and LUMO levels as well as ionization potential and electron affinity (IP and EA) obtained in a self-consistently evaluated electrostatic environment are shown in Fig. 4.15. Especially for the IP/EA values, the absolute energy levels are shifted by polarization effects of the local and global environment. Simple vacuum calculations do not capture this effect, making a detailed quantum-mechanical treatment of the polarization effects necessary. All materials having at least one quinoline-ligand as largest conjugated electronic system show similar LUMO levels and IPs as the reference molecule Alq_3 whose HOMO-LUMO gap is indicated as dashed lines. The strongest deviations occur for the molecules Alq_2Op, $AlOp_3$, $AlPopy_3$ and $AlAcac_3$ (see Fig. 4.14a-c). The two materials containing the Op-ligand show lower LUMO energies and higher electron affinities compared to Alq_3. This can be explained by a stronger orbital delocalization on the π-conjugated Op-ligand compared to quinoline with the smaller π-system. The increased delocalization leads to lower orbital energies, larger electron affinities and smaller HOMO-LUMO gaps. The opposite effect can be observed in the very small π-conjugated system of the Acac ligand (5 carbon atoms). This ligand leads to a low electron affinity of $AlAcac_3$ and a high LUMO energy. The slightly larger ligands Popy (2×6 aromatic carbon atoms) and Trop (7 aromatic carbon atoms) still lead to an increased LUMO level and reduced electron affinity compared to Alq_3 with a ligands size of 10 aromatic carbon atoms. This behavior is systematically analyzed for the exchange of quinoline ligands by Acac ligands from Alq_3 over Alq_2Acac and $AlqAcac_2$ to $AlAcac_3$ (indicated in red in Fig. 4.15). The less quinoline ligands are available for additional electrons, the smaller becomes
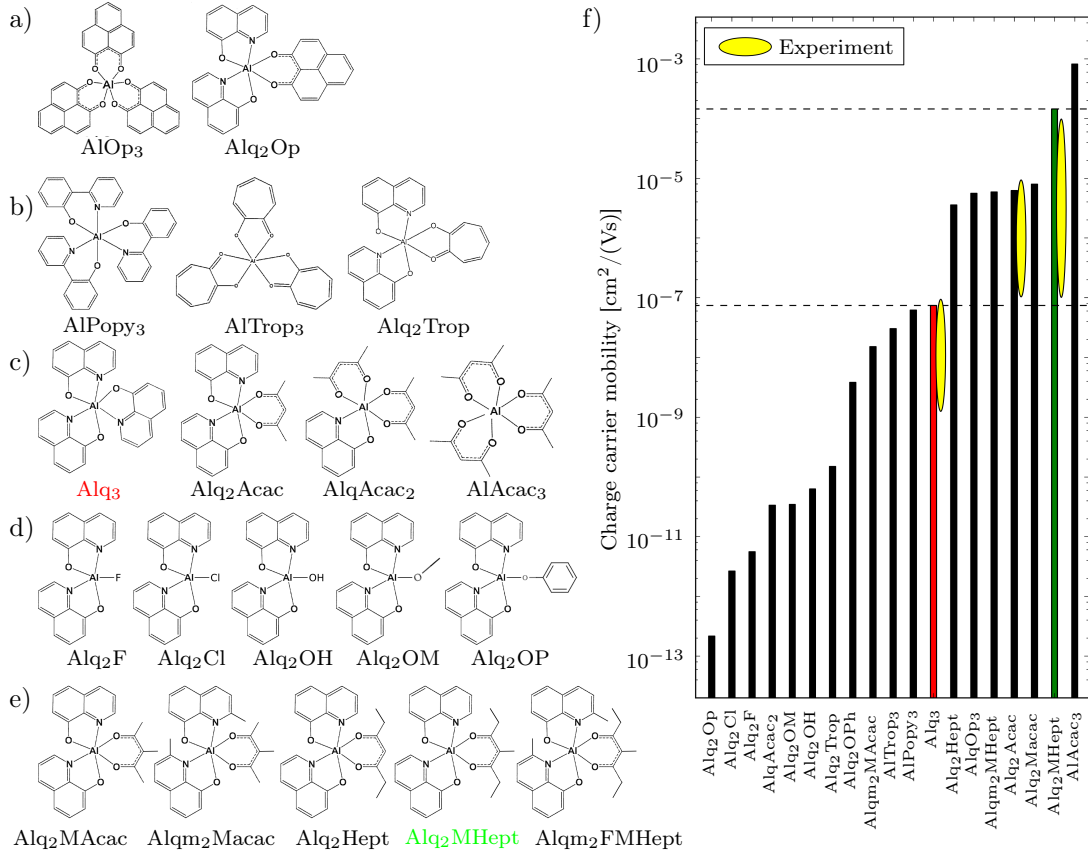
Figure 4.14: The aluminum complexes studied in this work. Panels a) and b) show molecules, in which at least one of the three quinoline ligands of Alq_3 was exchanged by ligands with a) larger and b) smaller conjugated π-systems. c) shows the systematic exchange of quinoline ligands of Alq_3 by Acac ligands. d) Alq_2X molecules where X was chosen in order to minimize the dipole moment of the molecules without having a large conjugated π-system. e) Alq_2X molecules where X was chosen in order to minimize the electrostatic potential created by the molecule. This is achieved by protecting the highly polar core of the molecule. Figure f) shows the predicted electron mobilities of the 19 materials. The reference material Alq_3 is highlighted in red, Alq_2MHept as a promising candidate with improved electron mobility compared to Alq_3 is marked in green. Its calculated (green bar) and measured (yellow circles) electron mobility is more than three orders of magnitude higher than the electron mobility of Alq_3 (red bar).

94
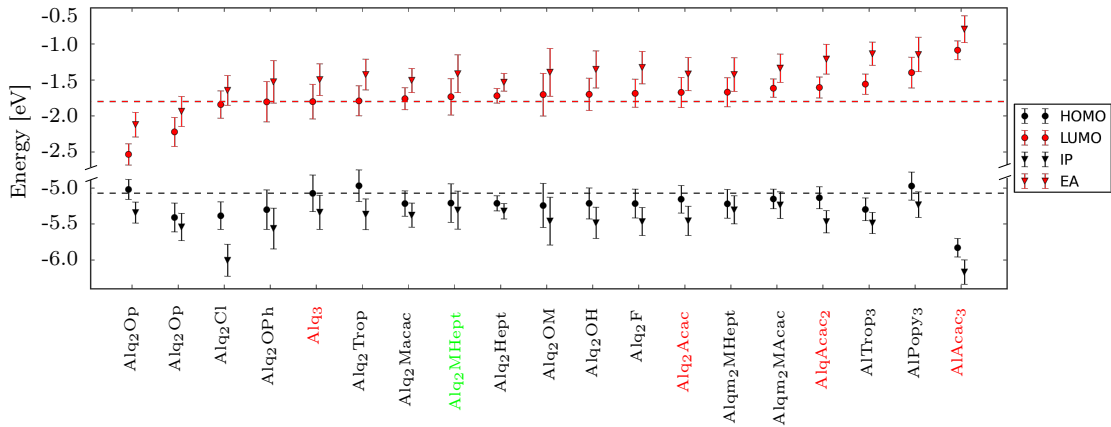
Figure 4.15: a) Energy levels for all tested materials are shown. The order of the materials corresponds to the bulk LUMO levels. The dashed horizontal lines indicate the HOMO/LUMO gap of the reference system Alq_3. The materials Alq_3 to $AlAcac_3$ (see Fig. 4.14) marked in red show the systematic increase of LUMO energy due to systematic exchange of quinoline ligands. Alq_2MHept having the largest simulated electron mobility is marked in green.

the electron affinity and the higher becomes the LUMO level. Replacement of one quinoline ligand shifts the levels less than $0.2\,\text{eV}$ whereas the step from $AlqAcac_2$ to $AlAcac_3$ increases the LUMO level by more than $0.5\,\text{eV}$. Thus, the energy levels of a homoleptic complex are rather insensitive towards replacement of one ligand with another (smaller) ligand because the decisive molecular orbitals stay unaffected on the remaining quinoline ligands. This opens possibility for modifications of other molecular properties by modification of one of the three quinoline ligands of Alq_3. The effect can be summed up as a rule for the design of new electron conducting molecules: The LUMO-level and the electron affinity are mainly determined by the largest conjugated π-system of a molecule.

One of the most decisive quantities for the performance of a molecule in a device is the charge carrier mobility. The charge carrier mobility exponentially depends on the square of the microscopic energy disorder of a material [14, 53]. As shown in the last chapter, apart from internal distortions of the molecules in the amorphous phase, one of the main sources of energy disorder is electrostatic interaction between molecules (see Fig. 4.16). Fig. 4.17a depicts the correlation between molecular dipole moments and energy disorder. This correlation is rather weak due to a group of outliers, which are marked in red. The common feature of these outliers is the uncommon combination of low molecular dipole moments with high values of energy disorder. Examples for such materials are shown in Fig. 4.14d. The reason of this unexpected behavior is strong short-range electrostatic interaction
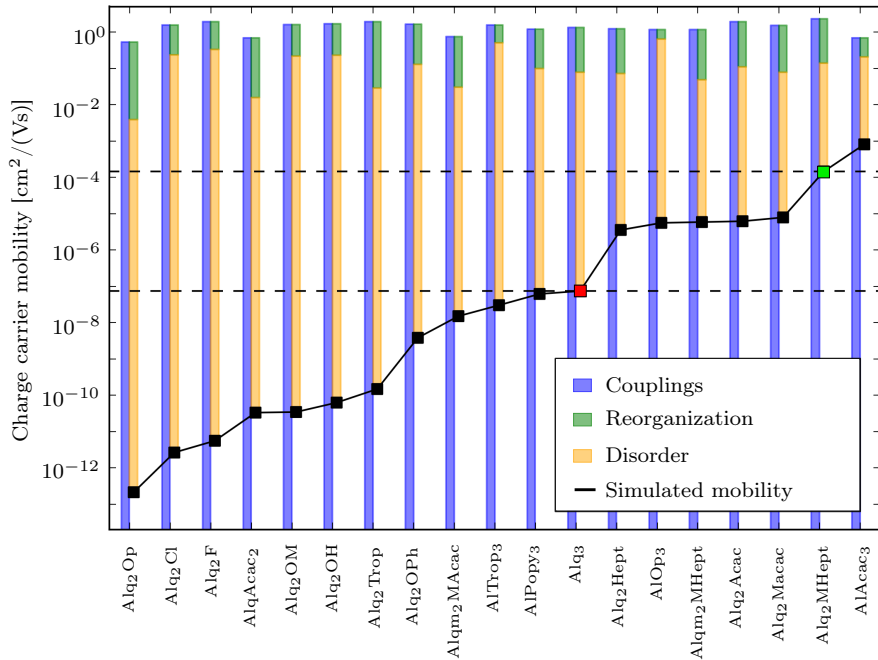
Figure 4.16: Electron mobilities of the set of aluminum complexes shown in Fig. 4.14a-e. Alq_3 and Alq_2MHept are marked as red and green squares. The bars show different contributions to charge carrier mobility. The blue bars depict the prefactor of the charge mobility which mainly depends on electronic couplings. Taking reorganization energies into account (green bars) leads to a spread of mobility of less than two orders of magnitude. The main difference between the different materials is the energy disorder (yellow bars).
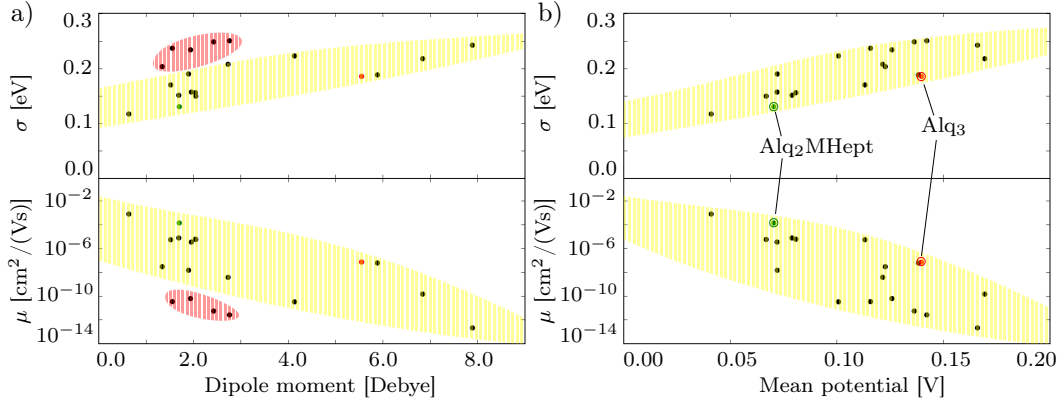
Figure 4.17: Panels a) and b) show the energy disorder σ and electron mobility μ compared to the dipole moment (panel a) and the mean potential (panel b) of the respective molecule. For the calculation of the mean potential, the electrostatic potential is averaged on shells at distances of $3.2\,\text{Å}$ and $4.6\,\text{Å}$ around the molecules.

between the highly polar aluminum core of the molecules. These local electrostatic monopole moments are not included in the long-range dipole moment. A quantity which includes both long-range dipole moment and local electrostatic moments is the mean electrostatic potential in medium proximity of a molecule. As shown in Fig. 4.17b, energy disorder σ and electron mobility μ show a strong correlation with this mean interaction potential. The strongest correlation with a correlation coefficient of $r = 0.80$ is achieved by evaluation of the electrostatic environment on surfaces between $3.2\,\text{Å}$ and $4.6\,\text{Å}$ around the molecules. While keeping the energy levels shown in Fig. 4.15 constant, the mean electrostatic potential can be continuously tuned between $40\,\text{mV}$ and $170\,\text{mV}$ by adjusting only one ligand in order to reduce the energy disorder of a molecule and maximize the charge mobility.

4.6.3 EXPERIMENTAL VALIDATION

Using the materials shown in Fig. 4.14a-d, design criteria were derived in the last chapter. These rules are now applied to systematically increase the charge mobility of Alq_3. For this purpose, the Acac-ligand of Alq_2Acac is systematically adjusted to decrease the mean interaction potential and to improve the screening of the polar core of the compounds (see Fig. 4.14e). An additional Methyl group in the middle of the Acac-ligand reduces the dipole moment while the elongation of the Alkyl chain from five to seven carbon atoms improves the shielding of the aluminum core. With these changes, a predicted electron mobility of more than $1 \cdot 10^{-4}\,\text{cm}^2/(\text{Vs})$ is obtained for the molecule Alq_2MHept.
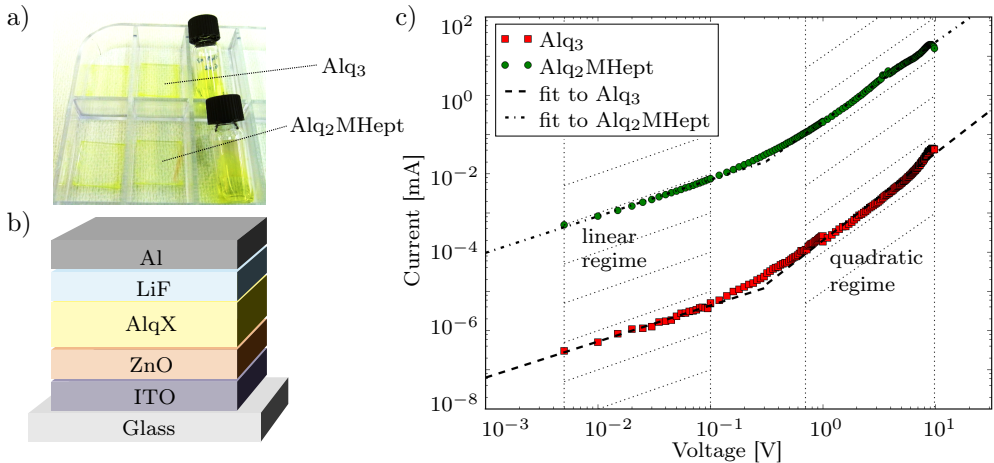
Figure 4.18: Panel a) shows spin-coat layers of Alq_3 and Alq_2MHept. In panel b), the stack design of the devices used for the SCLC measurements is shown. Panel c) shows the current voltage characteristics of the SCLC measurements of Alq_3 and Alq_2MHept. A transition from a linear to the quadratic SCLC regime is observed. The vertical dotted lines indicate the range of data points used for fitting. The dotted lines between them indicate the slopes of $I \propto U$ and $I \propto U^2$ respectively. The dashed and dashed-dotted lines are fits to the experimental data of Alq_3 and Alq_2MHept, respectively. The measurements were performed by Michael Jenne and Christian Sprau at LTI, KIT.

This theoretical prediction was experimentally confirmed by synthesis of the molecule followed by space-charge limited current (SCLC) measurements of spin-coated thin films. The results are shown in Fig. 4.18. The electron mobility is derived from the $I \propto U^2$ regime of the SCLC measurements.

$$I = \frac{9}{8} A \varepsilon \varepsilon_0 \mu \frac{U^2}{d^3} \tag{4.3}$$

In this equation, I is the measured current, $A = 0.035 \, \text{cm}^2$ is the device area, ε_0 is the vacuum permittivity $\varepsilon \approx 3$ the relative permittivity, μ is the charge carrier mobility, U the applied voltage and d the layer thickness obtained in surface profilometer measurements ($d = 150 \, \text{nm}$ for Alq_3 and $d = 250 \, \text{nm}$ for Alq_2MHept). Eq. 4.3 yields electron mobilities of $\mu_e = 6.5 \cdot 10^{-8} \, \text{cm}^2/(\text{Vs})$ for Alq_3, and $\mu_e = 3.3 \cdot 10^{-4} \, \text{cm}^2/(\text{Vs})$ for Alq_2MHept. The experimental electron mobility is indicated by the yellow circles in Fig. 4.14f. The values confirm the theoretical predictions ($\mu_e = 7.4 \cdot 10^{-8} \, \text{cm}^2/(\text{Vs})$ for Alq_3, and $\mu_e = 1.4 \cdot 10^{-4} \, \text{cm}^2/(\text{Vs})$) and show an improvement of electron mobility of three orders of magnitude between Alq_3 and Alq_2MHept.
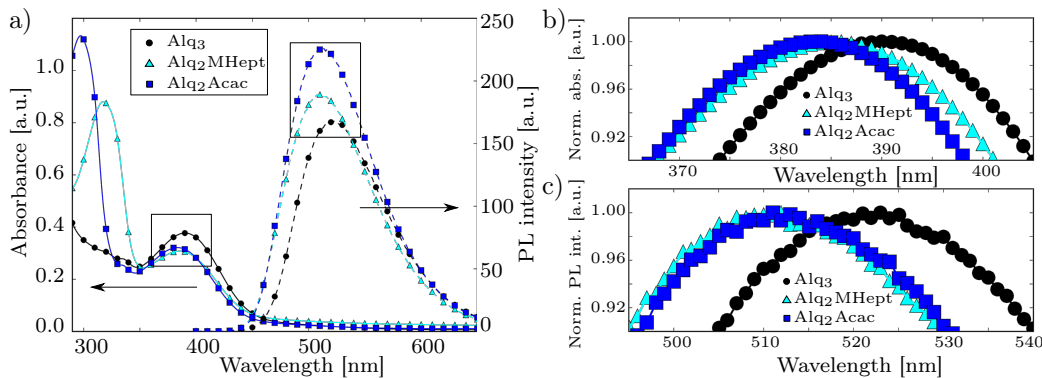
Figure 4.19: a) Absorption spectra of Alq_3, Alq_2Acac and Alq_2MHept show characteristic peaks of the quinoline ligands at a wavelength of $\lambda = 380 - 390\,nm$ and of the Acac ligands at a wavelength of $\lambda = 300 - 320\,nm$. The photoluminescence maxima are at wavelengths of $\lambda = 510 - 530\,nm$. Panels b) and c) show the normalized absorbance and luminescence maxima. Shifts of maximum absorbance and luminescence arise from replacement of one quinoline ligand by MHept and Acac ligands, respectively. The measurements were performed by Michael Jenne and Christian Sprau at LTI, KIT.

4.6.4 ABSORPTION AND PHOTOLUMINESCENCE

In order to investigate further properties of Alq_3, Alq_2Acac and Alq_2MHept, the absorption and photoluminescence spectra of these materials were measured. The results are shown in Fig. 4.19. Analysis of the absorbance and photoluminescence (PL) maxima shows a blueshift from Alq_3 to Alq_2Acac and Alq_2MHept. The absorption maximum of Alq_3 is at a wavelength of $\lambda = 390\,nm$ while Alq_2Acac and Alq_2MHept show maxima of $\lambda = 384\,nm$ and $\lambda = 386\,nm$, respectively (see Fig. 4.19b). This is in agreement with the slightly increased HOMO-LUMO gap due to the smaller conjugated systems of the Acac and MHept ligands compared to the replaced quinoline ligand. The same blueshift can be observed in the PL peaks in see Fig. 4.19c. Here, the shift of the peak is slightly larger, going from $\lambda = 523\,nm$ for Alq_3 to $\lambda = 511\,nm$ for Alq_2Acac and $\lambda = 512\,nm$ for Alq_2MHept. To compare computed ionization potentials to measurements, Photo-Electron Spectroscopy in Air measurements (PESA) were performed by Christian Sprau at LTI, KIT. These show an ionization potential of $IP = 5.85\,eV$ for Alq_3 and ionization potentials of $IP = 5.88\,eV$ and $IP = 5.89\,eV$ for Alq_2Acac and Alq_2MHept, respectively. The shift in experimental ionization potential is in agreement with the calculated HOMO energies of $E_{HOMO} = 5.07\,eV$, $E_{HOMO} = 5.16\,eV$ and $E_{HOMO} = 5.21\,eV$ for Alq_3 to Alq_2Acac and Alq_2MHept, respectively. The computed ionization potentials are $IP = 5.34\,eV$, $IP = 5.46\,eV$ and $IP = 5.31\,eV$.

In this chapter, design rules for the systematic generation of new molecular structures with improved properties such as charge carrier mobility and energy levels were derived. It was shown that the ionization potential and electron affinity are directly linked to the electronic properties of the ligand where additional charges are localized. Since these energy levels are decisive for injection barriers and interface properties, precise adjustment of energy levels is of primary importance for the application of a material in a device. The electrostatic properties of the ligands have a strong impact on the molecular dipole moment and on intermolecular interaction which is a decisive part of energy disorder and charge mobility. Thus, the systematic modification of the Alq_3 ligand system yields insights into the factors that govern charge mobility. Using these results, a new aluminum complex was designed showing a predicted and experimentally confirmed electron mobility which is three orders of magnitude higher than the electron mobility of Alq_3. As these observations are applicable to all organic semiconductors, the design rules established in this work extend well beyond the studied systems.

4.7 FURTHER APPLICATIONS

Apart from the examples presented in this work, many more open scientific questions related to organic electronics are discussed in literature. Examples are material interfaces [186], chemical doping [187] and morphological anisotropy [46]. For many of such topics, the multiscale approach presented in this work can be used to gain further inside into material and system properties. In most of the cases, this insight can be used for targeted material design and to guide experiment in improving device characteristics.

This chapter will present organic materials and applications, in which the simulations methods developed in this work were applied to answer fundamental questions concerning charge transport. Firstly, four topics will be discussed briefly, namely chemically doped organic materials, correlated systems, self-assembled materials with low energy disorder and the simulation of excited states in organic materials. Secondly, the simulation of an organic solar cell will be presented and discussed in Chapter 4.7.5. These simulations cover the generation of three-dimensional coarse grained morphologies as well as an estimate of charge mobility and exciton diffusion length in mixed materials.

4.7.1 DOPED ORGANIC MATERIALS

One way to to increase charge carrier density and thus conductivity of semiconductors is doping of the material. In organic semiconductors, a certain amount of dopant molecules is mixed into the amorphous thin film. The dopant molecules are chosen in a way that they either remove electrons from the occupied states of the host matrix (p-doping) or inject electrons into the unoccupied states of the host matrix (n-doping). This process strongly depends on the differences of ionization potential and electron affinity of the host and the dopant molecules. The presence of dopant molecules and the charge transfer between dopant and host molecules not only increases the charge carrier density but also influences the charge mobility of the host material. I applied the Quantum Patch method to such doped systems in order to analyze the interaction between host and dopant molecules. This analysis can be compared to doping efficiencies and the influence of doping of charge mobility and conductivity. Detailed understanding of these microscopic effects finally helps to improve existing and design new doping materials. In a first work, I theoretically investigated the influence of dopant molecules on the energy levels of host molecules via electrostatic interaction. This effect is discussed in Schneider *et al.* [15] using different experimental and theoretical methods.

4.7.2 Correlated systems

Another important factor influencing charge transport characteristics are correlations. I analyzed different forms of correlations, *e.g.* spatial correlations between energy levels due to long-range electrostatic interaction (see Massé *et al.* [20] and Appendix F), correlations between orbital energies (mainly HOMO and LUMO) which potentially influence exciton transport (see Massé *et al.* [21]) as well as correlations of the molecular orientation leading to an anisotropy of the amorphous material. The latter effect is experimentally known as giant surface potential effect [188]. This effect occurs in many organic semiconductors due to an anisotropic distribution of molecular dipole moments in amorphous thin films. In Friederich *et al.* [16], this effect will be discussed from a microscopic and theoretical point of view. Monte Carlo methods for the generation of atomistically resolved molecular systems as well as the Quantum Patch method will be used to investigate and understand the origin of the giant surface potential which only occurs for certain materials.

4.7.3 Self-assembled materials

Charge transport properties of all materials presented in this work are dominated by structural and energetic disorder. Self-assembled materials such as molecular wires and metal organic frameworks (MOFs) are examples of regularly applied materials, in which disorder is not the dominating property. In contrast to amorphous materials, both material classes show a comparatively low energy disorder, making electronic couplings the dominant contribution to charge transport properties. In Karipidou *et al.* [17], I analyzed the charge transport mechanism in molecular wires, where differences between hopping processes along and between wires play an important role. Charge transport in loaded MOFs on the other hand can be dominated by super-exchange processes between the guest molecules via intermediate virtual states. The super-exchange mechanism and its application to organic guest-host system is presented in Symalla *et al.* [19]. Here, I contributed to an extension of the super-exchange formalism for mixed disordered organic materials. This formalism is used to analyze charge transport in loaded metal organic frameworks in Neumann *et al.* [18], where I calculated the electronic structure and super-exchange hopping rates in MOFs loaded with TCNQ and F_4TCNQ.

4.7.4 Excited states

The flexibility of the Quantum Patch method and the possibility of hybrid implementations (as shown in Friederich *et al.* [129]) makes it furthermore possible to study non-ground-state properties like polarons, charge transfer states and exci-

tons in disordered systems. The latter play a crucial role in organic light emitting diodes as well as in organic solar cell. Thus, the Quantum Patch method has been be extended to analyze the excited states properties of excitons and their interaction with other species like polarons. The results of this work will be presented in Setzer *et al.* [189].

## 4.7.5 Nano- and mesoscale properties of organic solar cells

In this section, some of the methods presented in Chapter 3 are applied to study the influence of meso- and nanoscale morphology on exciton separation and charge transport in the active layer of an organic solar cell. The figures and parts of the discussion are adopted from Mönch *et al.* [132].

In organic solar cells (see Chapter 2.1.2), two competing demands, namely small material domains for exciton separation and large material domains for efficient charge extraction have to be fulfilled [190, 191]. Thus, the grain size of the bulk heterojunction (BHJ) morphology of an organic solar cell has to be optimized. Experimentally, this can be achieved by adjusting the substrate temperature during vacuum deposition of the active layer of the solar cell [192–195]. This section will discuss the influence of the substrate temperature during vapor deposition of the solar cell on nano- and mesoscale properties of the bulk heterojunction. The system analyzed here and in Mönch *et al.* [132] consists of a nip-sandwiched structure with an active layer made of the dicyanovinyl-substituted oligothiophene derivative DCV5T-Me as donor [194, 196–199] and a fullerene C_{60} as acceptor [27] (see Fig. 4.3). With this material system, a power conversion efficiency (PCE) of 8.3 % were reported in literature [200].

Experimental work

In Mönch *et al.* [132], DCV5T-Me:C_{60} solar cells are analyzed which were prepared at different substrate temperatures (room temperature (RT) and 80 °C). The current-voltage $(j - V)$ characteristics of these solar cells are shown in Fig. 4.20 and the respective open circuit voltages V_{OC}. The solar cell deposited at a substrate temperature of 80 °C shows an improved power conversion efficiency (PCE) of $PCE = 6.8$ % compared to the solar cell deposited at room temperature $(PCE = 4.5$ %).

To investigate properties of the bulk heterojunction in the active layer, energy dispersive X-ray (EDX) measurements (STEM-EDX) [201] were performed to in-
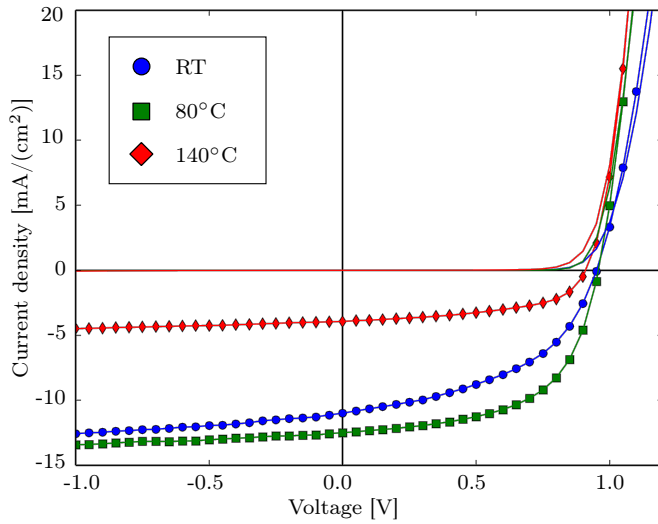
Figure 4.20: $j - V$ curves of solar cells deposited at a substrate temperature of RT (blue circles) and 80 °C (green squares). The solid lines without symbols show the $j - V$ curves without illumination. The data is taken from Mönch *et al.* [132].

vestigate phase separation at the required nanoscale resolution [202]. The EDX signal arises from chemical contrast between DCV5T-Me and C_{60} [203–205]. As sulfur is only present in DCV5T-Me, the STEM-EDX signal quantitatively measures the amount of this material in the layer at a certain point. The resolution of the measurement is limited by the focus of the electron beam, which is on the order of several nanometers. The sulfur sensitive STEM-EDX measurements of samples annealed at room temperature and at 80 °C are shown in Fig. 4.21a and b. Thickness variations were measured using the high-angle annular dark-field imaging technique as a reference to the STEM-EDX measurements.

Fig. 4.21a shows the sulfur sensitive STEM-EDX signal of a DCV5T-Me:C_{60} layer deposited at room temperature. A fine-grained domain structure of DCV5T-Me and C_{60} can be observed. Fig. 4.21b depicts the thin-film morphology of the absorber layer deposited at 80 °C. Here, small carbon-rich islands with a diameter larger than 10 nm can be observed. These are embedded in a well-connected sulfur-rich network. The phase separation of the absorber layer is accompanied by an increased domain purity compared to the sample deposited at room temperature. This observation correlates well with the increased short circuit current density and fill factor of the solar cell.
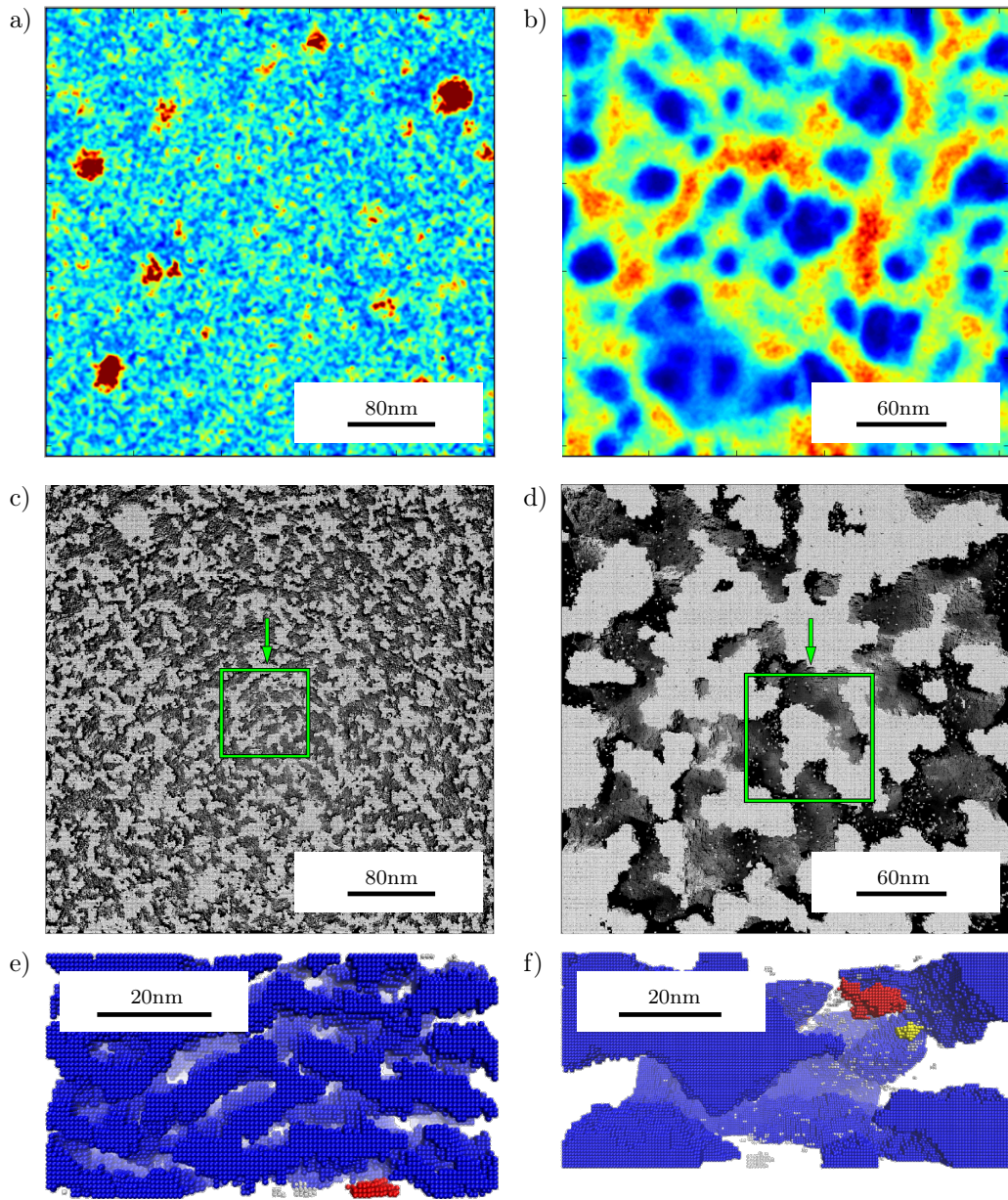
Figure 4.21: Panels a) and b) show the relative amount of DCV5T-Me in the RT and the 80 °C samples. The data is extracted from the experimental STEM-EDX measurements. It is used for the generation of mesoscopic three-dimensional morphologies. Panels c) and d) show top-view images of three-dimensional morphologies generated using the STEM-EDX input. Panels e) and f) show side views of the sections marked in green. The C_{60} domains are transparent. The Figure is taken from Mönch *et al.* [132].

To link microscopic images to macroscopic $j - V$ characteristics, simulations were performed to better understand the microscopic and mesoscopic properties of DCV5T-Me:C_{60} solar cells. As described in Chapter 2.1.2, strongly bound excitons are generated in the bulk heterojunction and migrate until they reach a material interface. At the interface, the excitons dissociate with a certain probability into bound electron-hole pairs in charge transfer states, where the electron is localized on a C_{60} molecule and the hole on a DCV5T-Me molecule. Once the charge transfer states are separated, the resulting free electrons and holes move towards the electrodes in a diffusive process. Since the charge carriers are confined to either donor or acceptor material, closed connections from each point of the donor-acceptor interface to the respective electrodes are required.

The efficiency of the device is, among others, dependent on three factors: 1) exciton diffusion, 2) exciton dissociation and 3) charge carrier collection. In order to dissociate, excitons must reach a material interface within their lifetime and diffusion length. The probability of this process increases if the exciton diffusion length is large compared to the domain size of the absorber material. In this study, the dissociation rate of the exciton, once it has reached an interface, is assumed to be independent of the morphology and therefore sample independent. The third important factor in the model is the degree of connectivity of the different material domains. Considering the exciton diffusion process, the room temperature sample shown in Fig. 4.21a should have a higher internal quantum efficiency in comparison to the 80 °C sample shown in Fig. 4.21b. This assumption contradicts the experimental findings. On the other hand, small domains, as visible in the room temperature sample, might lead to island formation. This would not only reduce the connectivity of material domains but also facilitate charge carrier recombination, which will counterbalance the increased exciton separation probability by decreasing the efficiency of charge extraction.

To quantify the interplay between domain size and island formation, three-dimensional coarse-grained morphologies (see Chapter 3.4) based on the STEM-EDX data for the room temperature and the 80 °C samples were generated. The results are presented in Section 4.7.5. Furthermore, the exciton and charge mobility in both samples was estimated using atomistic morphologies and the Quantum Patch method (results in Section 4.7.5).

To generate three-dimensional morphologies, a Monte Carlo based simulated annealing method as presented in Chapter 3.4 is used [206]. The three-dimensional morphology generation is based on two-dimensional STEM-EDX data obtained from the sulfur-sensitive images shown in Fig. 4.21a and Fig. 4.21b. The STEM-EDX signal allows to quantitatively extract the relative amount of DCV5T-Me in the layer below each pixel of the STEM-EDX image. The three-dimensional morphologies generated in this procedure have the same out-of-plane-projection of the DCV5T-Me content as the experimental STEM-EDX input. Representative illustrations of the morphologies with isotropic domain sizes and interconnectivity in all three dimensions are shown in Fig. 4.21c-f.

Based on these morphologies, the connectivity of each material domain to the respective electrodes was analyzed. In agreement with visual inspection (see Fig. 4.21c-f), the quantitative analysis yields that the $80\,°$C sample consists of two interpenetrating, singly connected C_{60} and DCV5T-Me domains that percolate through the entire sample. Surprisingly, the connectivity of the room temperature sample is equally good, despite its apparent finer grain size of the bulk heterojunction. At both substrate temperatures, more than $99\,\%$ of the material in both domains are connected to the electrodes. This is in agreement with classical percolation theory, as the volume fraction of the two material components (0.44) is larger than the percolation threshold of 0.10 to 0.31, depending on the degree of connectivity [207, 208].

The consequence of this observation is depicted in the side views shown in Fig. 4.21e and f, where the color represents the connectivity of material domains. It is visible that almost all domains are interconnected and build up a complete percolation network (marked in blue). Single isolated islands are highlighted in different colors. This explains the observation of similar currents at high negative voltages in Fig. 4.20. At these voltages, almost all charge carriers in domains with a connection to the electrodes are extracted with negligible recombination losses. Thus, only exciton separation and material connectivity play a role.

Based on the simulated three-dimensional morphologies, the mean distance each exciton has to travel to reach an interface was computed. This was done by mapping the interface distances of the three-dimensional morphology on a model where all domains have a spherical shape. This analysis results in an average interface distances of $R_{\mathrm{RT}} = 3.1\,\mathrm{nm}$ and $2.8\,\mathrm{nm}$ for C_{60} and DCV5T-Me domains, respectively. For the device prepared at $80\,°$C, $R_{80\,°\mathrm{C}} = 10.6\,\mathrm{nm}$ and $9.8\,\mathrm{nm}$ for C_{60} and

DCV5T-Me are obtained, respectively. These average interface distances are in good agreement with visual analysis of the two-dimensional images in Fig. 4.21a and b. Despite an average interface distance of approximately 10 nm in the 80 °C sample, 83 % of the excitons generated are within 4 nm from a donor-acceptor interface. This is still within the limits of typical exciton diffusion lengths of 5−40 nm and matches the value of the comparable molecule DCV-6T (9 ± 3 nm) [209–212]. Those values demonstrate that the phase separation at a substrate temperature of 80 °C does not lead to losses due to exciton recombination. Experimental support for this hypothesis is given by the slightly larger current density at negative voltages in the 80 °C sample compared to the room temperature sample (see Fig. 4.20). As the external electric field does not influence the diffusion process of a neutral exciton, this current density reflects the total amount of electrons and holes being generated in the sample and extracted due to the high field strength.

ATOMISTIC SIMULATIONS

To understand why the sample deposited at room temperature has a smaller efficiency than the 80 °C sample, the influence of the microscopic material composition on the charge carrier mobility and exciton diffusion length is estimated in this section. As discussed in Chapter 4.4, the most significant quantity determining the mobility of charge carriers in disordered organic semiconductors is the width of the distribution of site energies σ [14, 48, 68, 131, 167]. There are two sources of energy disorder (see Chapter 4.5) for charges and excitons. These sources are differences of the molecular geometry (conformational disorder) and polarization effects due to electrostatic interaction between the molecules (electrostatic disorder). As both C_{60} and DCV5T-Me are relatively rigid, the energy disorder mainly arises from electrostatic interactions between the molecules at different sites and their environment [213].

To estimate the energy disorder as a function of the local material composition, the strength of polarization effects and their influence on the local energy levels in mixed and pristine material domains was investigated. Due to the small domain size in the sample annealed at room temperature, almost each molecule is in relatively close proximity to a molecule of the other phase. In the samples annealed at 80 °C, the domain sizes are considerably larger. To account for these differences in interface proximity, atomically resolved morphologies for pure C_{60} and mixed DCV5T-Me:C_{60} morphologies were generated using the Deposit protocol (Chapter 3.1.2) [12]. These two extreme cases are representative for the small, rather intermixed domains in the room temperature sample and the larger and purer domains in the sample deposited at 80 °C. Each morphology contains 700
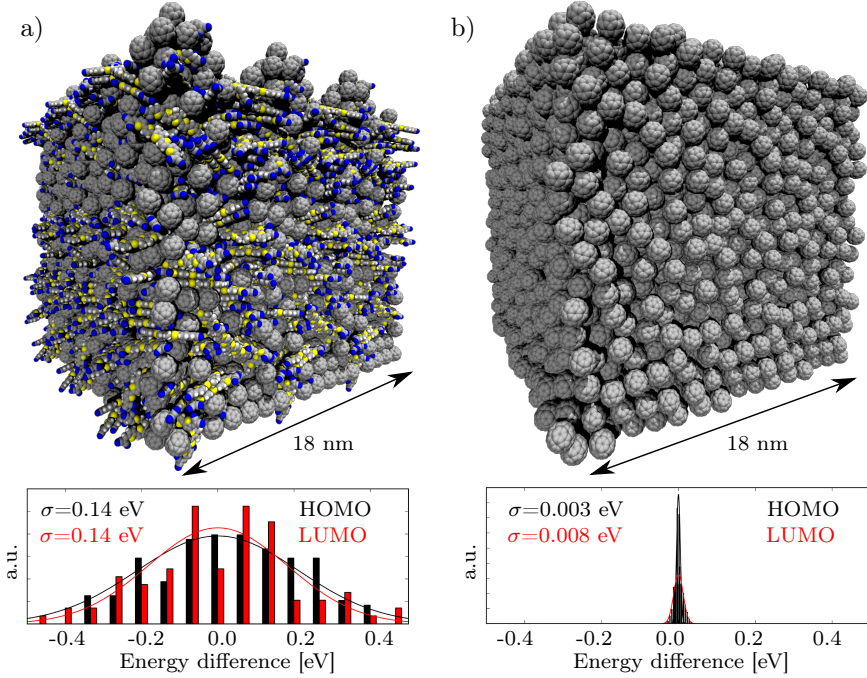
Figure 4.22: Atomistic morphologies and distributions of orbital energy differences of a) pure C_{60} and b) mixed DCV5T-Me:C_{60} morphologies. The distributions show the differences of C_{60} HOMO and LUMO energies (black and red) in the morphologies shown in panels a) and b). The solid lines are fits to the Gaussian distributions. Electrostatic interaction between C_{60} and DCV5T-Me leads to a broadening of the distribution of energy differences. The Figure is taken from Mönch *et al.* [132].

molecules which are periodically extended in x- and y-direction to obtain an electrostatic bulk embedding.

Fig. 4.22 shows the distribution of C_{60} HOMO and LUMO energies calculated using mixed DCV5T-Me:C_{60} (Fig. 4.22a) and pure C_{60} domains (Fig. 4.22b), which correspond to the limiting cases of strongly mixed domains in the RT sample and large, relatively pure domains in the 80 °C sample. The width of the distribution of energy differences is closely related to the local density of states which is calculated using the Quantum Patch method [68] (Chapter 3.2).

Calculations yield a electrostatic energy disorder in the pristine C_{60} system of $\sigma_{\mathrm{e}} = 8\,\mathrm{meV}$ for electrons and $\sigma_{\mathrm{h}} = 3\,\mathrm{meV}$ for holes, respectively. Consideration of thermal fluctuations of the order of $25\,\mathrm{meV}$ leads to values of approximately $26\,\mathrm{meV}$ which is commensurate with literature data for crystalline organic semiconductors [50]. In the mixed morphology shown in Fig. 4.22a, the energy disorder of C_{60} molecules (see Fig. 4.22a)) is drastically increased to $\sigma_{\mathrm{e}} = 158\,\mathrm{meV}$ for elec-

trons and $\sigma_h = 164\,\text{meV}$ for holes. This order of magnitude increase is caused by the random orientation of DCV5T-Me molecules in close proximity to the C_{60} molecules. The intrinsic electrostatic dipole moments of DCV5T-Me molecules (1.0 Debye) generate a unique and strong electrostatic environment for each C_{60} molecule which shifts the C_{60} energy levels. This leads to a two to three orders of magnitude increase in charge carrier mobility in pure domains of the 80 °C sample, compared to the mixed domains of the samples deposited at room temperature (details in Mönch *et al.* [132]).

As the exciton diffusion coefficient and the exciton diffusion length are exponentially dependent on the energy disorder, a similar effect can be expected for excitons. This would largely overcompensate the negative effect of increased domain size on the exciton separation probability in the 80 °C sample [167]. In pristine DCV5T-Me domains, the size of the dipole has a much weaker influence on energy disorder and exciton diffusion length, as these are expected to be highly ordered and, thus, have an energy disorder similar to the low values computed for C_{60} [197].

At the same time, improved charge mobility leads to a faster charge extraction and to a lower series resistance yielding an improved fill factor of the solar cell. These findings are well supported by both theory and experiment and conclusively explain the improved performance of the 80 °C sample. Simultaneously, they give design rules for the development of more efficient organic solar cells. One important factor determining the device efficiency is the formation of either pristine or ordered material domains. As shown in this section, one way of improving domain separation is the adjustment of the substrate temperature during deposition of the bulk heterojunction.

5

Summary and outlook

SUMMARY

Amorphous organic semiconductors are used in applications such as organic light emitting diodes and organic solar cells. Despite technical advances of commercially available organic devices, many material properties and physical processes are to date not well understood. One example is the relation between quantum mechanical properties of single molecules on the angstrom scale and thin film charge carrier mobility on the nanometer to micrometer scale. Better understanding of the basic physical principles of amorphous organic materials can enable rational material development and thus improvement of device efficiencies.

Charge carrier mobility μ of amorphous semiconductors is a strongly varying function of the energy disorder σ and the inverse temperature β: $\mu \propto \exp(-C\beta^2\sigma^2)$. The energy disorder arises from molecular distortion of the disordered molecules as well as from interaction between the molecules and their individual environment. To reliably compute the charge carrier mobility of organic materials, the energy disorder has to be calculated with high precision. This requires the combination of quantum mechanical analysis of the electronic structure of single molecules with meso-scale analysis of the disordered morphology.

In this work, I presented a multiscale simulation method which quantitatively predicts the charge carrier mobility of amorphous organic semiconductors. The *ab-inito*-based method only requires the chemical structure of a molecule as input and can therefore be used for predictive and reliable materials screening and design. The approach consists of several steps, covering all length scales which are relevant to describe the necessary processes determining macroscopic charge

transport properties.

Central and novel ingredient of the method is the Quantum Patch method which analyses the electronic structure of atomistically resolved molecular systems using quantum mechanical methods such as density functional theory (see Friederich *et al.* [68, 69, 129, 130] and Meded *et al.* [145]). The Quantum Patch method provides a self-consistent framework to compute the polaron energy on chosen molecules of the system, incorporating the individual molecular conformation as well as its interaction with the environment. This fulfills both requirements for the calculation of the aforementioned energy disorder. In order to accurately predict the energy disorder, molecular systems including several thousand molecules have to by analyzed. So far, this was only possible with empirically parameterized, molecular mechanics based methods which did not take into account quantum effects. The linearly scaling Quantum Patch method allows the analysis of such large systems and therefore enables the parameter-free prediction of energy disorder in realistic systems.

I have computed the charge carrier mobility of different experimentally known materials to test the capabilities and validate and results of the newly developed methods (see Friederich *et al.* [131]). The tests show a good agreement between theoretically calculated hole mobility and experimental measurements, where the charge mobility of the different materials spans a range of more than ten orders of magnitude. Furthermore, I used the results of these simulations to shed light on the relations between molecular and thin film properties. I could identify different molecular properties which mainly determine macroscopic charge mobility. This is achieved by factorization of the charge carrier mobility obtained with an effective-medium model [14] into different contributions. These contributions include the influence of different sources of energy disorder in amorphous systems as well as of reorganization energy and the electronic coupling between molecules.

The analysis of relations between molecular structure and thin film charge mobility enabled the postulation of design rules for new organic compounds. These rules were then used to systematically improve the widely used electron conducting molecule Alq$_3$ (see Magri *et al* [214] and Friederich *et al.* [215]). Here, I analyzed several novel materials and computed their charge carrier mobility. Targeted modifications of the molecular structures led to an increase in electron mobility of more than two orders of magnitude compared to the reference material Alq$_3$. One of the most promising candidates was synthesized by Verónica Gómez in the group of Mario Ruben at INT, KIT. Measurements of the electron mobility were performed by Michael Jenne and Christian Sprau in the group of Alexander Colsmann at

LTI, KIT. SCLC measurements confirm the simulation results which predict an improvement of the electron mobility of almost three orders of magnitude. This proof of principle of *in-silico* molecule design demonstrates the potential of the multiscale workflow to be applied in targeted material development. Beyond the aluminum complexes shown in this works, it can be used for the improvement of charge mobility in different classes of molecules and material combinations.

Outlook

To extend the range of possible applications of the methods presented in this work and to further improve their capability of tackling open scientific questions in the field of organic electronics, several extensions are planned. One example it the modeling of full devices which includes the explicit simulation of charge and exciton transport using kinetic Monte Carlo approaches. The approximative effective medium model used in this work is useful for the determination of the molecular origin of charge mobility. Due to its restriction to single layers with only one type of charge carrier, this model cannot be used for device simulations, where the interaction between electrons, holes and excitons as well as more complicated device architectures play an important role. This type of systems can be modeled using kinetic Monte Carlo (KMC) approaches, where all processes are simulated explicitly. Similar to the effective medium model, all KMC simulations require process rates, which depend on microscopic material properties such as electronic couplings and reorganization energies of large systems. This challenge can be tackled using a combination of the Quantum Patch method and KMC simulations.

In order to include and analyze excited state properties of organic materials which are relevant in both OLEDs and organic solar cells, improved methods for the generation of atomistic morphologies are required. State of the art molecular dynamics or Monte Carlo simulations use classical force fields to describe the interaction between molecules during the generation of molecular systems. Even molecule specific parameterization of these force-fields, especially for soft intramolecular degrees of freedom, is in many cases not accurate enough to be used in quantum mechanical calculations of excited state properties. Fixed point charges describing the electrostatic interaction between molecules as well as the neglect of correlations between internal degrees of freedom and the neglect of quantum effects due to localization and delocalization of molecular orbitals are approximations, which can be overcome in more sophisticated approaches. Correlations between internal degrees of freedom can be mapped to classical force fields using the quantum mechanical eigenmodes of the molecules instead of bond lengths and

(dihedral) angles as free parameters. Orbital (de)localization and changes of the electron density of individually distorted molecules are much more challenging to map to classical force fields. Here, a full quantum mechanical analysis of molecular structures becomes inevitable. This can be achieved on different levels of accuracy. Errors in electrostatics can be fixed using a re-evaluation of partial charges after each deposition step. Inaccuracies in internal degrees of freedom can either be improved using a quantum mechanical post-relaxation of each newly deposited molecule or using a self-consistent relaxation of the entire molecular structure in a self-consistent procedure similar to the Quantum Patch method.

Last, but not least, the flexibility of the multiscale method and in particular the Quantum Patch method can be used to analyze, understand and improve state-of-the art materials used in highly efficient organic light emitting diodes and organic solar cell. This includes the analysis of the stability of phosphorescent emitter and host molecules and their degradation mechanism, the targeted improvement of highly efficient molecules showing thermally activated delayed-fluorescence, the investigation of charge separation at organic heterointerfaces in solar cells and many more. Furthermore, most of the highly efficient, solution processed organic solar cells use polymers to absorb light and to generate excitons. Extensions of the Quantum Patch method are possible which can be used to study the transport mechanism of partially delocalized states in such high-mobility polymers.

A
Abbreviations

AG	(*german*) Arbeitsgruppe
α-NPD	Organic molecule, see Chapter 4.2
Alq$_3$	Metal-organic complex, see Chapter 4.2
AM1	Austin model 1
AMBER	Assisted model building with energy refinement
AMOEBA	Atomic multipole optimized energetics for biomolecular applications
AO	Atomic orbital
B3LYP	Hybrid DFT functional, see Chapter 2.3.2
BCC	Bond charge corrections
BHJ	Bulk heterojunction
BP86	also b-p, DFT functional, see Chapter 2.3.2
cDFT	Constrained density functional theory
CDM	Correlated disorder model
CIGS	Copper indium gallium selenide
COG	Center of geometry
COM	Center of mass
CPU	Central processing unit
CT	Charge transfer
DCV5T-Me	Organic oligomer, see Chapter 4.2
DEPB	Organic molecule, see Chapter 4.2
DFTB	Density functional based tight binding
DFT	Density functional theory
EA	Electron affinity
ECDM	Extended correlated disorder model
ECP	Effective core potentials

EDX	Energy dispersive X-ray detector
EGDM	Extended Gaussian disorder model
EL	Emissive layer
EQE	External quantum efficiency
ESP	Electrostatic potential
ETL	Electron transport layer
FF	Fill factor
FHJ	Flat heterojunction
F_4TCNQ	Organic molecule
GAFF	General AMBER force field
GDM	Gaussian disorder model
GEMM	Generalized effective-medium model
GGA	Generalized gradient approximation
GPU	Graphics processing unit
GSP	Giant surface potential
HAADF	High-angle annular dark field
HF	Hartree-Fock
HOMO	Highest occupied molecular orbital
HTL	Hole transport layer
INT	Institute of Nanotechnology
IP	Ionization potential
IQE	Internal quantum efficiency
KIT	Karlsruhe Institute of Technology
KMC	Kinetic Monte Carlo
LDA	Local-density approximation
LED	Light emitting diode
LJ	Lennard-Jones
LTI	Light Technology Institute
LUMO	Lowest unoccupied molecular orbital
mBPD	Organic molecule, see Chapter 4.2
MC	Monte Carlo
MD	Molecular dynamics
ME	Master equation
MOF	Metal-organic framework
MO	Molecular orbital
MSL	Materials Science Laboratory Sony, Stuttgart
NNP	Organic molecule, see Chapter 4.2
NPT	Number of particles, pressure, temperature
NVT	Number of particles, volume, temperature
OFET	Organic field effect transistor

OLED	Organic light emitting diode
OPV	Organic photovoltaics
OSC	Organic solar cell
PBC	Periodic boundary conditions
PCBM	Organic molecule, see Chapter 4.2
PCE	Power conversion efficiency
PCM	Polarizable continuum model
pFFA	Organic molecule, see Chapter 4.2
PF	Poole-Frenkel
PHEN	Organic molecule phenanthrene
PL	Photoluminescence
QM/MM	Quantum mechanics/molecular mechanics
RFID	Radio-frequency identification
RT	Room temperature
SA	Simulated annealing
SCF	Self-consistent field method
SCLC	Space charge limited current
sEQE	Sensitive external quantum efficiency
SOMO	Single occupied molecular orbital
STEM	Scanning transmission electron microscope
SUC	Organic molecule succinonitrile
SUMO	Singly unoccupied molecular orbital
SV(P)	Split valence basis-set with polarization, see Chapter 2.3.2
SX	Superexchange
TCNQ	Organic molecule
TPD	Organic molecule, see Chapter 4.2
TZVP	Triple-ζ split valence basis-set with polarization, see Chapter 2.3.2
vdW	van der Waals

B

Benchmark of the Quantum Patch method

To estimate the efficiency of the hybrid methods presented in Chapter 4.3, the computational requirements of the protocols presented above were compared. The results are depicted in Fig. B.1. The calculations were performed on 2.6 GHz Intel Xeon processors E5-2670 (Sandy Bridge). One DFT calculation of a charged molecule takes approximatively 15 min of CPU-time on a including pre- and post-processing of a charged molecule while the effort for an uncharged molecule are 6 min. Here, a B3LYP [22]/SV(P) [23] level of theory was used as implemented in TURBOMOLE [24, 216]. The corresponding calculations using DFTB [148, 217, 218] take on average 4 s per molecule. Typically, seven iteration steps according to the Quantum Patch method are required to reach converged self-consistency. In each step, 100 charged centers are considered, each of them surrounded by approximatively 100 molecules which are self-consistently re-evaluated in each iteration cycle. In the "hybrid large" method, on average 12 of these 100 environment molecules are treated using DFT while the rest is calculated using DFTB. For simplification, all additional preparation steps as well as necessary pre-calculations were not taken into account. In this case, the "full QM" method requires 14210 CPU-h. The "hybrid large" method giving the most accurate results reduces the "full QM" effort to 15.2 % or 2167 CPU-h. The "hybrid small" method reduces the computational effort to 3.6 % or 506 CPU-h, whereas the purely semi-empirical method requires only 156 h, which is 1.1 % of the "full QM" CPU-time.

As a comparison, the last column of Fig. B.1 shows the computational effort of the neutral Quantum Patch method. This method is required as a reference method to calculate ionization potentials and electron affinities (for details, see
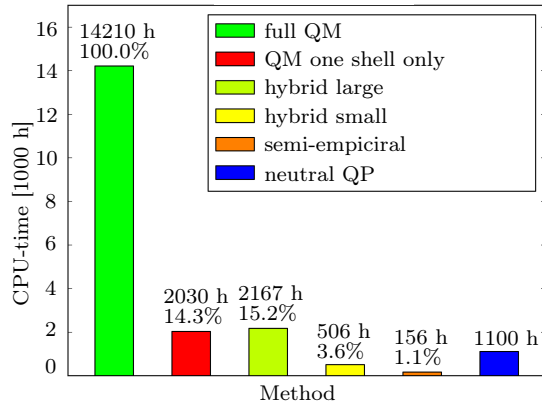
Figure B.1: Computational effort of the methods presented in Tab. 4.1. The most accurate method "hybrid large" (see Fig. 4.5) is reducing the computational cost by over 80 % without significant loss of precision. The image is taken from Friederich *et al.* [129].

Friederich *et al.* [68]). Apart from the reference "full QM" approach, the most accurate method is the "hybrid large" approach, which is less than a factor of two more expensive than the neutral Quantum Patch method. This enables *in silico* materials prescreening with high accuracy and reliability.

C

Accelerated demixing algorithms

Typical STEM-EDX images, such as the ones presented in Chapter 4.7.5 and in Mönch *et al.* [132], have lateral sizes if 512×512 pixels. In z-direction, approximately 70 pixels are required in this example to account for the film thickness. Thus, three dimensional morphologies of these samples contain approximately 18 million voxels. The demixing simulation starts with an initial, random state and converges as soon as the system reaches a isotropic three-dimensional representation of the experimental two-dimensional input. For this procedure, several billion steps are required. Without technical and numerical methods to accelerate the simulation, this system size cannot be simulated within acceptable time scales. Two methods which accelerate the demixing simulations will be presented in this chapter.

Parallelization

The first method is a technical solution using massive parallelization. In the model presented in this chapter, no long range interactions are taken into account. Due to the local energy model, the acceptance criterion for the exchange of neighboring voxels only depends on the first neighbor shell of the respective particles. Therefore, many exchange processes can be evaluated simultaneously and independent of each other in different parts of the system. This allows for parallelization of the Monte Carlo simulation. Fig. C.1 illustrates one possibility of parallelization of moves. In Fig. C.1a, one single exchange process in a conventional Monte Carlo simulation is shown. Using the grid shown in Fig. C.1b, many moves can be evaluated simultaneously. Due to the spacing between the grid cells, the evaluations of all acceptance criteria are independent from one another. Using *e.g.* GPU-based parallelization techniques, the Monte Carlo simulation can be accelerated by fac-
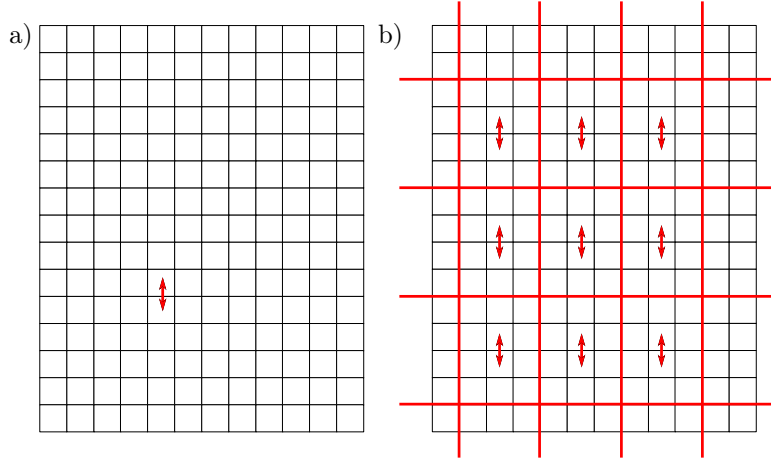
Figure C.1: a) One random move is performed in each step of a conventional Monte Carlo simulation. b) All moves in the red subgrid can be evaluated simultaneously and independently from one another. This allows for parallelization of the Monte Carlo simulation.

tors in the order of 10^4 to 10^5. In systems of size N^3 voxels and a subgrid of size $3 \times 3 \times 4 = 36$ voxels, $N^3/36$ steps can be evaluated in parallel. Due to the size of available GPUs, the speed-up is limited by the number of GPU cores.

RESOLUTION SCALING

A second method to accelerate the generation of three-dimensional morphologies is called resolution scaling. Here, the experimental input structure is first scaled down to a lower resolution. In this lower resolution, a three-dimensional representation is generated and simulated until convergence. Afterwards, the two-dimensional input and the converged three-dimensional representation are scaled up and used in a second simulation. Due to intrinsic uncertainties in the upscaling process, the initial three-dimensional structure of the second calculation contains defects and artifacts such as large step edges and random vacancies. During the simulations, these errors are fixed and the structure is equilibrated at the higher resolution. This procedure is repeated until the final resolution of the original experimental image is reached.

An example of this resolution scaling technique is shown in Fig. C.2. Here, an experimental input structure with the size 100×100 pixels (see Fig. C.2c) is scaled down to 25×25 (Fig. C.2a) and 50×50 pixels (Fig. C.2b) before the simulation reaches the full resolution. Fig. C.2a, b and c are the z-projections of the simulation. Fig. C.2d, e and f are projections in x-direction and Fig. C.2g,
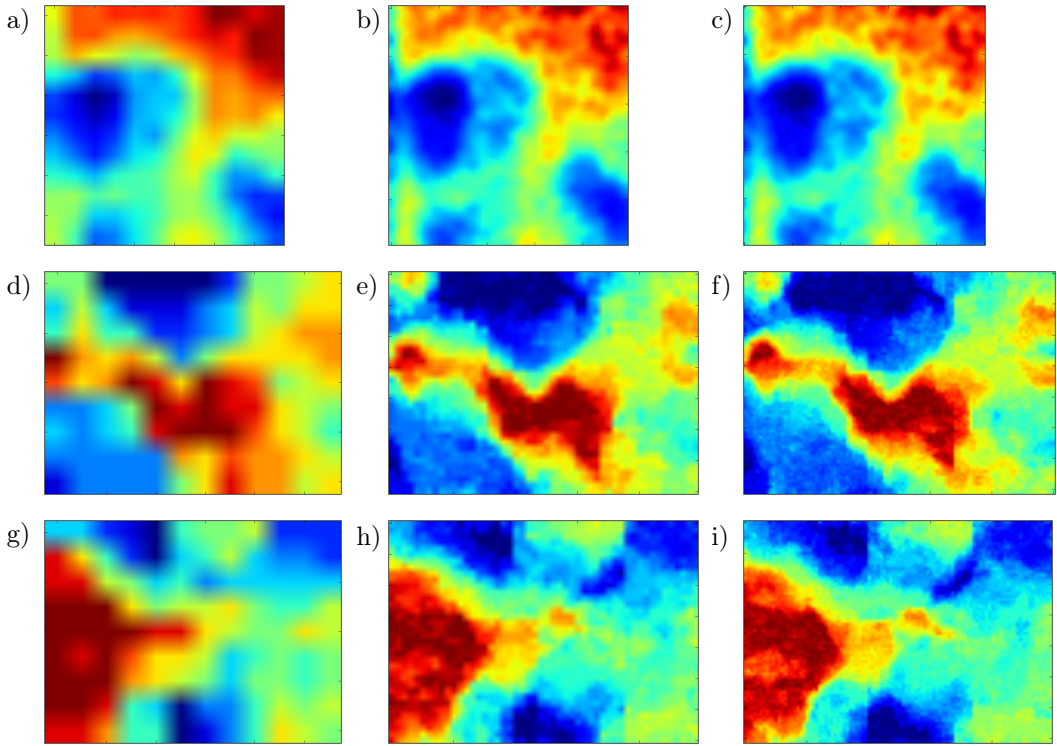
Figure C.2: Examples of the resolution scaling technique. The first column shows a simulation with a lateral box size of 25×25 pixels, while the simulation boxes in the second and the third column have sizes of 50×50 pixels and 100×100 pixels, respectively. The images in the first line (a, b and c) show z-projections of the simulation box while the images in the second (d, e and f) and third (g, h and i) line are projections in x-direction and y-direction, respectively.

h and i are projections in y-direction. It is visible that the converged structure shows similar grain sizes in all three dimensions.

D
Orbital degeneracy and level splitting

In this section, the structure and degeneracy of HOMO and LUMO orbitals of α-NPD, TCTA and Spiro-DPVBi in amorphous films is analyzed and compared to vacuum optimized structures of the molecules. The individual symmetry of the molecules in their vacuum relaxed structure leads to a characteristic degeneracy of occupied and unoccupied states. This degeneracy is lifted in the amorphous thin film due to disorder effects as discussed in the last chapters. The level spacing between different occupied orbitals (ΔE_{HOMO}) as well as between unoccupied orbitals (ΔE_{LUMO}) is analyzed in the following section. The names HOMO-1 and LUMO+1 refer to the orbitals below the highest occupied molecular orbital and above the lowest unoccupied molecular orbital, respectively.

SPIRO-DPVBI

The vacuum structure of Spiro-DPVBi shows a D2d symmetry with two equivalent molecular units rotated 90° with respect to each other. This leads to a degeneracy of both the HOMOs and the LUMOs (see Fig. D.1). The energy splitting between HOMO and HOMO-1 is $\Delta E_{\mathrm{HOMO}} = 0.060\,\mathrm{eV}$ while the energy splitting between LUMO and LUMO+1 is $\Delta E_{\mathrm{LUMO}} = 0.012\,\mathrm{eV}$. The energy gap below HOMO-1 and above LUMO+1 is considerably larger. In the amorphous phase, the symmetry is distorted which lifts the degeneracy of the energy levels. Energy splittings extracted from the molecular system are $\Delta E_{\mathrm{HOMO}} = (0.203 \pm 0.047)\,\mathrm{eV}$ and $\Delta E_{\mathrm{LUMO}} = (0.200 \pm 0.124)\,\mathrm{eV}$. As shown in Fig. D.2a and D.2b, HOMO and HOMO-1 are no longer symmetric and antisymmetric linear combinations of nearly degenerate orbitals of the two molecular units but rather show characteristics of molecular orbitals of the single units. The hybridization of orbitals as shown in HOMO and HOMO-1 in Fig. D.1 might be an artifact of missing
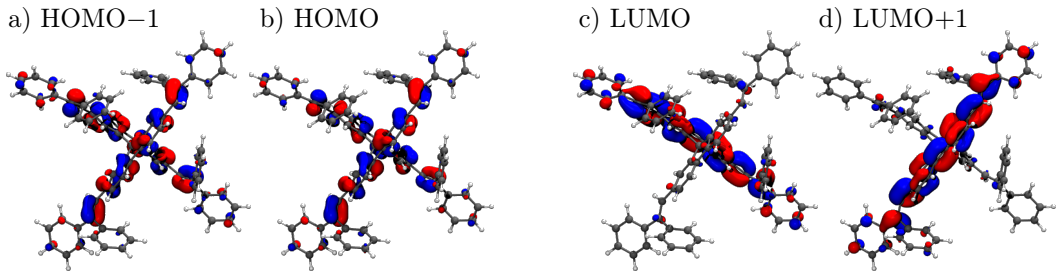
**Figure D.1:** Vacuum orbitals of Spiro-DPVBi.
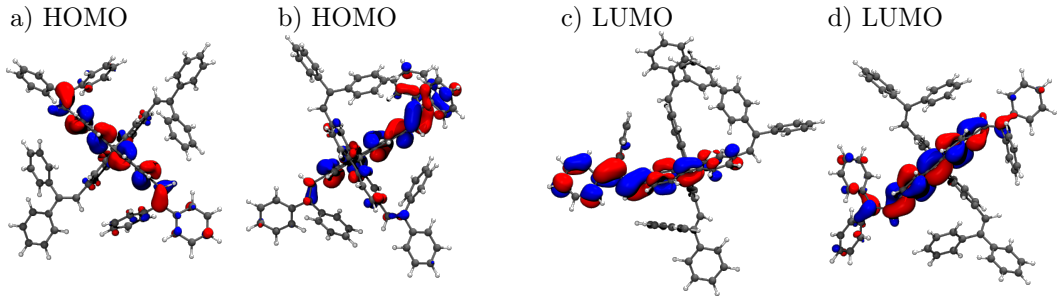
**Figure D.2:** Orbitals of Spiro-DPVBi in the amorphous phase.

exchange energy in LDA and GGA-functionals of DFT. Even the hybrid B3LYP functional used here may not fully correct this error. In addition to that, the molecular orbitals become asymmetric themselves due to environment and bending effects (see Fig. D.2b). The nearly degenerate vacuum LUMO and LUMO+1 keep their general shape but also become less symmetric in the amorphous system (see Fig. D.2c and D.2d).

α-NPD

The HOMO of α-NPD in vacuum is separated from the HOMO-1 by $0.455\,\mathrm{eV}$, whereas the LUMO and LUMO+1 shown in Fig. D.3 are separated by only $0.033\,\mathrm{eV}$. The reason for this is the molecular structure which contains two naphthyl groups with similar electronic structure. Similar to Spiro-DPVBi, this degeneracy is lifted in the solid state due to electrostatic interaction and conformational disorder of the molecules. The LUMO to LUMO+1 gap increases to $\Delta E_{\mathrm{LUMO}} = (0.093 \pm 0.058)\,\mathrm{eV}$. Also here, the hybridization of two unoccupied naphthyl orbitals to symmetric and antisymmetric linear combinations as shown in the LUMO and LUMO+1 in Fig. D.3 might be an artifact of DFT. In the solid phase, the HOMO remains delocalized over the entire molecule (Fig. D.4a and Fig. D.4b) while the symmetry of the two naphthyl units is distorted and the LUMOs localize on opposite sides of the molecule (see Fig. D.4c and D.4d).

a) HOMO   b) LUMO   c) LUMO+1
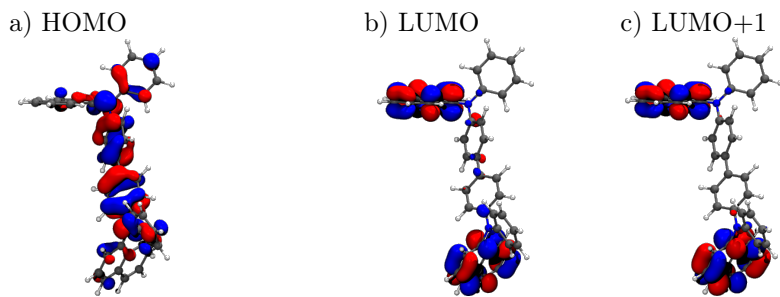
Figure D.3: Vacuum orbitals of α-NPD.


a) HOMO   b) HOMO   c) LUMO   d) LUMO
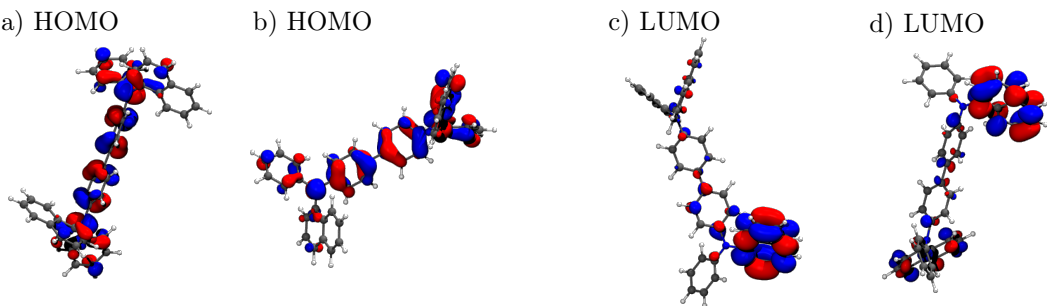
Figure D.4: Orbitals of α-NPD in the amorphous phase.

TCTA

TCTA shows a propeller-like C3 symmetry. The highest occupied molecular orbital is delocalized over all three arms of the molecule with a gap to HOMO-1 of 0.348 eV. The lowest unoccupied orbitals are linear combinations of orbitals of the three phenyl groups directly connected to the central nitrogen atom. Three of these linear combinations are very close in energy with gaps of 0.012 eV between LUMO and LUMO+1 and 0.023 eV between LUMO and LUMO+2 (see Fig. D.5). Similar to Spiro-DPVBi and α-NPD, the symmetry is broken in the amorphous state leading to an increase in energy splittings. In the solid state, $\Delta E_{\mathrm{LUMO,1}}$ becomes (0.090 ± 0.064) eV. and $\Delta E_{\mathrm{LUMO,2}}$ becomes (0.152 ± 0.075) eV. These (lifted) degeneracies reflect themselves in the shape of HOMOs and LUMOs in the matrix as shown in Fig. D.6. The HOMO of TCTA therefore localizes on two or only one arm whereas it is symmetrically delocalized in the vacuum geometry. The lowest unoccupied molecular orbital localizes on only one of the central phenyl rings (Fig. D.6c). In some cases, the orbital order even changes and a carbazole-orbital becomes the lowest unoccupied molecular orbital of TCTA as shown in Fig. D.6d.
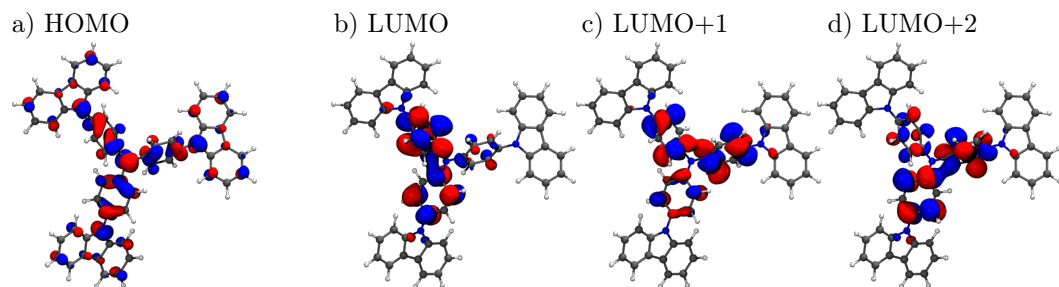
**Figure D.5:** Vacuum orbitals of TCTA.
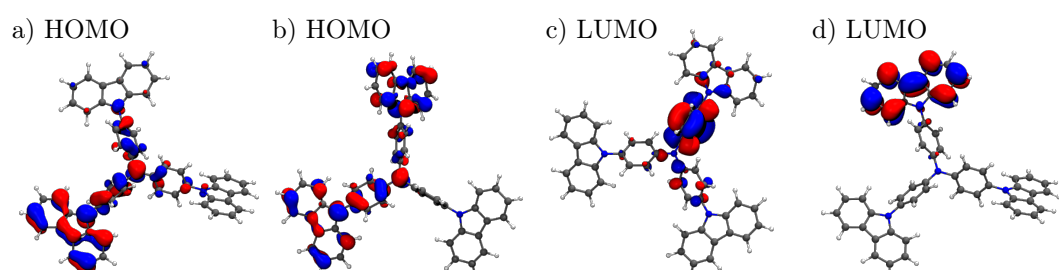
Figure D.6: Orbitals of TCTA in the amorphous phase.

E

C-factor dependence of charge mobility

As shown Rodin *et al.* [14, 68], the GEMM model with $C = 1/4$ corresponds to the effective medium limit. This is in agreement with previously reported effective medium approaches [14, 70, 99]. As illustrated in Fig. E.1, this C-factor leads to best agreement between simulated charge mobility and experimental data. Fig. E.1 furthermore shows the charge carrier mobility in case the GEMM expression is modified to KMC fitted values of $C = 0.36$ which are assumed to be valid for medium disorder strength and finally $C = 0.44$, which is valid in the percolation limit. For all materials except mBPD, the discrepancies between calculations and experiment become considerably larger with increasing C-factor. It is possible but unlikely that a systematic error in the calculation of the microscopic input parameters would bias the charge mobility of almost all materials tested toward the effective medium limit.

More complex analytic models have been discussed in literature (see *e.g.* Fischchuk *et al.* [95]). Such models use C-factors, which depend on the interplay between energy disorder and reorganization energy. As pointed out by Bässler *et al.* [53], this relationship depends on molecular connectivity and off-diagonal disorder. Many models are parameterized using kinetic Monte Carlo (KMC) calculations performed on perfect rectangular lattices. Rodin *et al.* pointed out in Ref. [14] that connectivity might actually be different for real morphologies compared to perfect rectangular or face-centered cubic (fcc) lattices. Therefore, the GEMM approach in Eq. 2.17) with $C = 0.25$ is used throughout this work. Nonetheless, kinetic Monte Carlo (KMC) simulations using realistic lattices and off-diagonal disorder are required to definitively answer this question. However, systems like Alq_3 require system sizes, which are not within the capability of KMC programs and hardware available today [98].

129
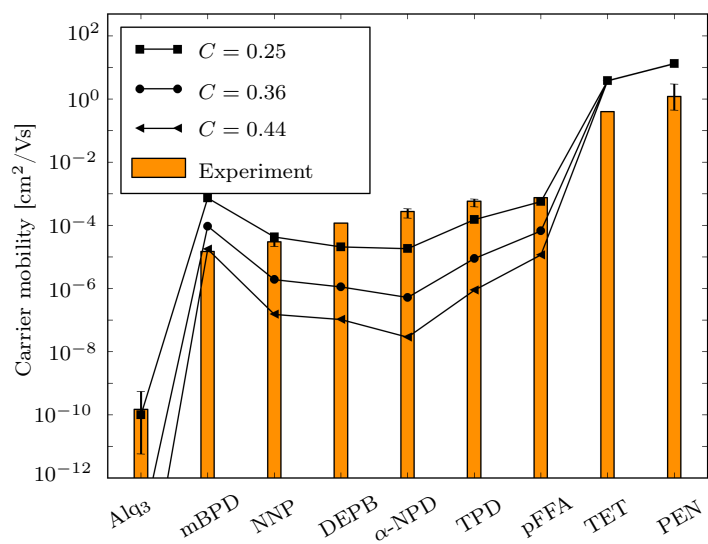
Figure E.1: Charge carrier mobility calculated using different C-factors in the GEMM model in Eq. 2.17. C varies between 0.25 (effective medium), 0.36 (KMC fitted, medium disorder strength), and 0.44 (percolation). The image is taken from Friederich *et al.* [131].

F
Correlations

Until now, the distribution of HOMO and LUMO energies (or ionization potentials and electron affinities) in amorphous molecular systems was considered to be distributed according to a Gaussian distribution. Calculation results as shown in Fig. 4.8a support this assumption. Nonetheless, correlations between energy levels of molecules can lead to deviations from this Gaussian distribution. One widely studied example are correlations arising from the long-range dipole interaction which is responsible for parts of the energy disorder [166, 219–222]. Analytic models as discussed in Bouhassoune *et al.* [219] investigate the influence of spatial correlations on the field- and disorder-dependence of the charge carrier mobility. Until recently, the strength of correlation effects could not be quantified due to a lack of computational approaches for the analysis of microscopic systems. Different models were used ranging from purely dipole correlated disorder to completely uncorrelated energy distributions.

In this chapter, amorphous systems of α-NPD, TCTA and Spiro-DPVBi are analyzed (see Fig. 4.1 and 4.2). Firstly, the effect of spatial correlations due to monopole-dipole and dipole-dipole interaction will be discussed. This discussion is also part of Massé *et al.* [20], my master's thesis [69] and Friederich *et al.* [131]. Afterwards, local correlations between HOMO and LUMO energies will be analyzed. This potentially influences electron-hole interactions as well as exciton transport and will be discussed in Massé *et al.* [21].

SPATIAL CORRELATIONS DUE TO LONG-RANGE ELECTROSTATIC INTERACTION

The energy disorder σ, which is used for the calculation of charge carrier mobility, is the width of the local density of states. It is calculated using the distribution
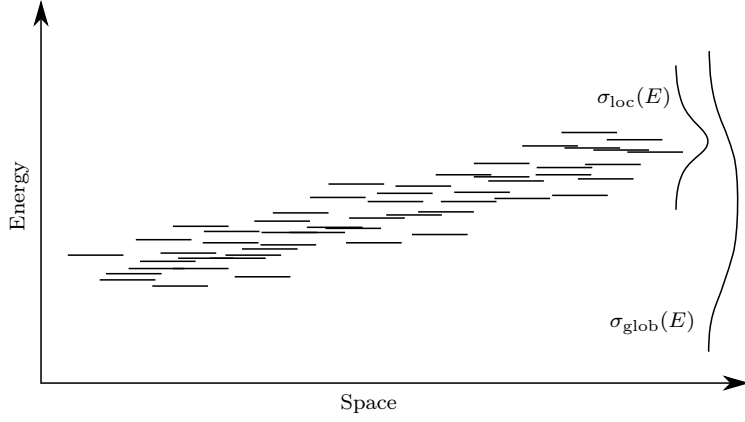
of local energy differences ΔE between molecules, which has a width of $\sigma(\Delta E)$. In this distribution of energy differences, only pairs with non-vanishing electronic couplings are included, following the assumption that the charge hopping is a local process limited to nearest-neighbor hopping events. Therefore, it contains only information about the local environment of charges and the local hopping rates which contribute to charge transport. This local energy disorder $\sigma_{\text{loc}}(E)$ shown in Tab. 4.5 is calculated as $\sigma(\Delta E)/\sqrt{2}$, which is the energy disorder of a reference system without spatial correlations but with the same distribution of local energy differences. From a microscopic point of view, spatial correlations due to long range electrostatic interaction might lead to a broadening of the global density of states ($\sigma_{\text{glob}}(E) > \sigma(\Delta E)/\sqrt{2}$). Local properties such as $\sigma(\Delta E)$ and the local energy disorder $\sigma_{\text{loc}}(E)$ on the other hand are insensitive to spatial correlations and thus will not be modified.

The difference of local and global energy distributions is shown in Fig F.1 for ferroelectric system with an internal electric field. While the local energy disorder $\sigma_{\text{loc}}(E)$ can be calculated using $\sigma_{\text{loc}}(E) = \sigma(\Delta E)/\sqrt{2}$, the global energy distribution is much wider and does not follow a Gaussian distribution.

Fig. F.2 shows the ratio of $\sigma(\Delta E)$ and $\sigma_{\text{glob}}(E)$ of different materials as a function of the maximum pair distance for different materials. In case of the uncorrelated model, this ratio is equal to $\sqrt{2}$ for all pair distances. In the dipole correlated model, the ratio is significantly smaller than $\sqrt{2}$, indicating a broadening of the global density of states compared to the local density of states. The correlation strength observed for amorphous α-NPD, TCTA and Spiro-DPVBi systems lies between the uncorrelated and the correlated model systems. Amorphous Spiro-DPVBi systems show weak correlations while the correlations in TCTA and α-NPD structures are not negligible. The off-set between $\sigma(\Delta E)/\sigma_{\text{glob}}(E)$ and $\sqrt{2}$ even at large pair-distances might arise from long-range ordering effects as theoretically investigated in Friederich *et al.* [16] and experimentally observed in Ref. [223–225] (see illustration in Fig. F.1). The correlation strength calculated in this section can be used in charge transport simulations using master equation based methods (see Chapter 2.2). More details about these simulations can be found in Massé *et al.* [20].

CORRELATIONS BETWEEN HOLE AND ELECTRON TRANSPORT LEVELS

In this section, the correlations between the frontier orbitals (HOMO and LUMO) of α-NPD, TCTA and Spiro-DPVBi are analyzed. The effect of conformational disorder is separated from the effect of electrostatic interaction with the neigh-

Figure F.1: Local and global distribution of molecular energies in case of a highly correlated ferroelectric system. While the local energy disorder $\sigma_{\mathrm{loc}}(E)$ can be calculated using local energy differences (see text), the global energy distribution is not a Gaussian distribution and the global energy disorder $\sigma_{\mathrm{glob}}(E)$ is not well defined any longer.
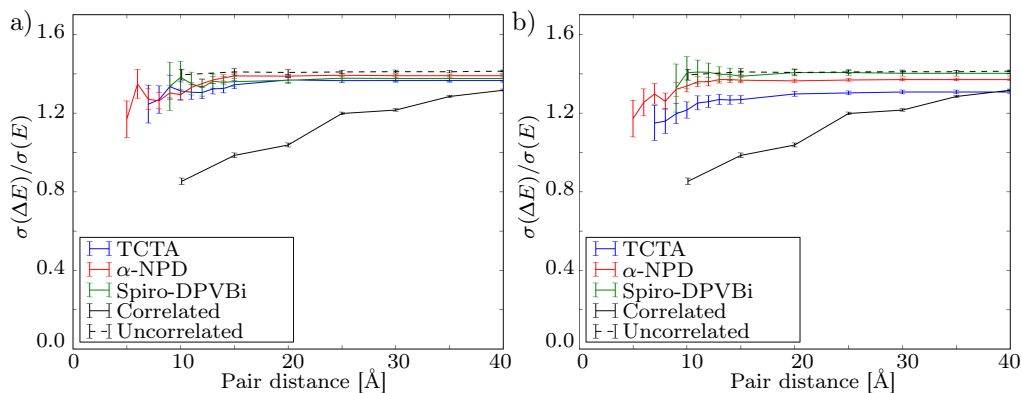
Figure F.2: Spatial correlations of a) HOMO and b) LUMO levels of α-NPD, TCTA and Spiro-DPVBi. These are compared to an uncorrelated and a dipole-correlated model. The data is published in Massé *et al.* [20].

133
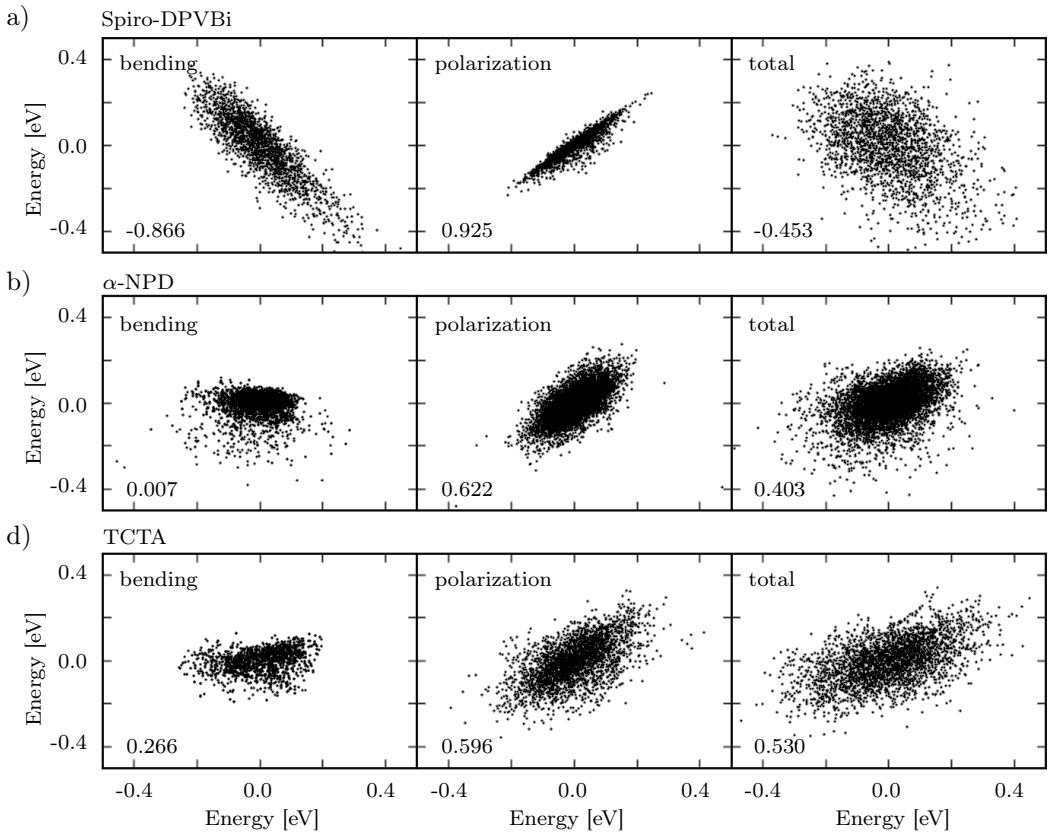
Figure F.3: HOMO and LUMO distributions of a) Spiro-DPVBi, b) α-NPD and c) TCTA. The numbers in the bottom left corners of each plot are the respective correlation coefficients. The scatter plots in the third column consider full energy differences between HOMO or LUMO energies of neighboring molecules. In the first column, contributions from internal molecular distortions (bending) to the full energy differences are extracted while in the second column, only intermolecular electrostatic interaction effects are considered (polarization). Using this analysis, it is possible to analyze the origin of the negative and positive energy level correlations for Spiro-DPVBi and α-NPD/TCTA, respectively.

boring molecules. The polarization effects show positive correlations due to the smooth long-range potential caused by the dipole moments of the molecules (see Fig. F.3). Internal dihedral distortions of α-NPD and TCTA do not lead to any significant correlation between HOMO and LUMO energies. In Spiro-DPVBi, the HOMO and LUMO energies show a strong anti-correlated behavior. This anti-correlation is caused by distortions of the dihedral angles connecting the side groups to the central spiro unit. The delocalization of occupied and unoccupied orbitals strongly depends on the dihedral angle leading to the anti-correlation of the HOMO and LUMO levels of Spiro-DPVBi.

In order to analyze the origin of local correlations between HOMO and LUMO orbitals, it is useful to separate the source of disorder into an electrostatic and a conformational part. The results of this analysis are shown in Fig. F.3. To quantify the correlations, the Pearson product-moment correlation coefficients c for the different HOMO and LUMO distributions was calculated (see Fig. F.3). The analysis shows that the correlation coefficient arising from orbital energy shifts due to electrostatic interaction and polarization (second column in Fig. F.3) is positive for all molecules. This indicates that the electrostatic potential varies on lengthscales larger than the typical size of molecules. This type of smooth electrostatic potential is caused by the (relatively small) dipole moments of the molecules. It influences and shifts HOMO and LUMO energies of each molecule in the same way, leading to a local correlation between HOMO and LUMO levels. The second contribution comes from internal distortions of the molecules in the solid state and shows a different behavior than the electrostatic correlations. In Spiro-DPVBi, a strong negative correlation coefficient ($c = -0.866$) between HOMO and LUMO energies can be observed. This negative correlation dominates the overall HOMO-LUMO correlation of Spiro-DPVBi. In α-NPD and TCTA, the correlation coefficient due to conformational disorder is almost negligible ($c = 0.007$ and $c = 266$, respectively). Here, the positive correlation coefficient due to electrostatic disorder dominates the overall HOMO-LUMO correlation.

In order to track down the strong, negative correlation between HOMO and LUMO energies in Spiro-DPVBi (see Fig. F.2, top left panel), the response of HOMO and LUMO orbital energies upon dihedral bending is analyzed. The four equivalent dihedral angles in direct contact to the central spiro unit of Spiro-DPVBi show a strongly anti-correlated behavior for HOMO and LUMO energies. One of these four (identical) dihedral potentials is shown in Fig. D.1, the position of the respective dihedral angle(s) is sketched in Fig. F.5.

The potential shown in Fig. F.5b shows a strong anti-correlated behavior of occupied and unoccupied orbital energies. While HOMO and HOMO-1 energies have a minimum at a dihedral angle of $\pm 90°$ and a maximum at $0°$, the unoccupied orbitals LUMO and LUMO$+1$ show the exact opposite trend. The dihedral angle dependence of the LUMO and LUMO$+1$ energies can be explained using the shape of these orbitals which are shown Fig. D.1a. As LUMO and LUMO$+1$ are decoupled orbitals of the two symmetric parts of the Spiro-DPVBi molecule (see also Fig. D.1), one of these two orbitals strongly reacts on distortions of a single dihedral angle and the other does not. At a dihedral angle of $0°$, the delocalization of the LUMO has its maximum. Increase of the dihedral angle towards $90°$ decreases this delocalization, leading to higher energies of the LUMO. At around
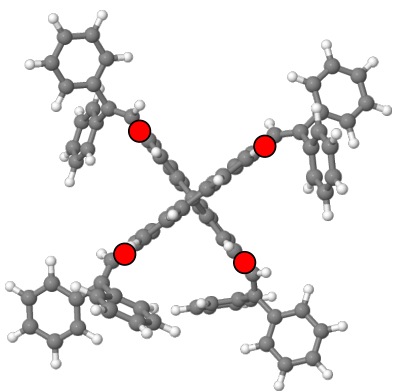
Figure F.4: Dihedral angles of Spiro-DPVBi, which show an anti-correlated behavior of HOMO and LUMO energies (see Fig. F.5) are marked with green dots. Distortions of these dihedral angles may cause the anti-correlation of Spiro-DPVBi in Fig. F.3.

approximately 40°, the order of LUMO and LUMO+1 changes and the orbital incorporating the ligand with a distorted dihedral angle becomes higher in energy than the undistorted one.

The HOMO orbitals on the other hand behave differently (see Fig. F.5c). At 0°, the HOMO orbitals of the two symmetric molecular units hybridize. HOMO and HOMO−1 are linear combinations of these orbitals and delocalize over the entire spiro unit and parts of the side-groups. A dihedral angle of 90° prevents delocalization, leading to a symmetry breaking of the two molecular units. This asymmetry of the two units hinders hybridization, separating the HOMO and HOMO−1 on two different parts of the Spiro-DPVBi molecule. This is energetically favorable for HOMO and HOMO−1, leading to a decrease rather than to an increase in orbital energy.
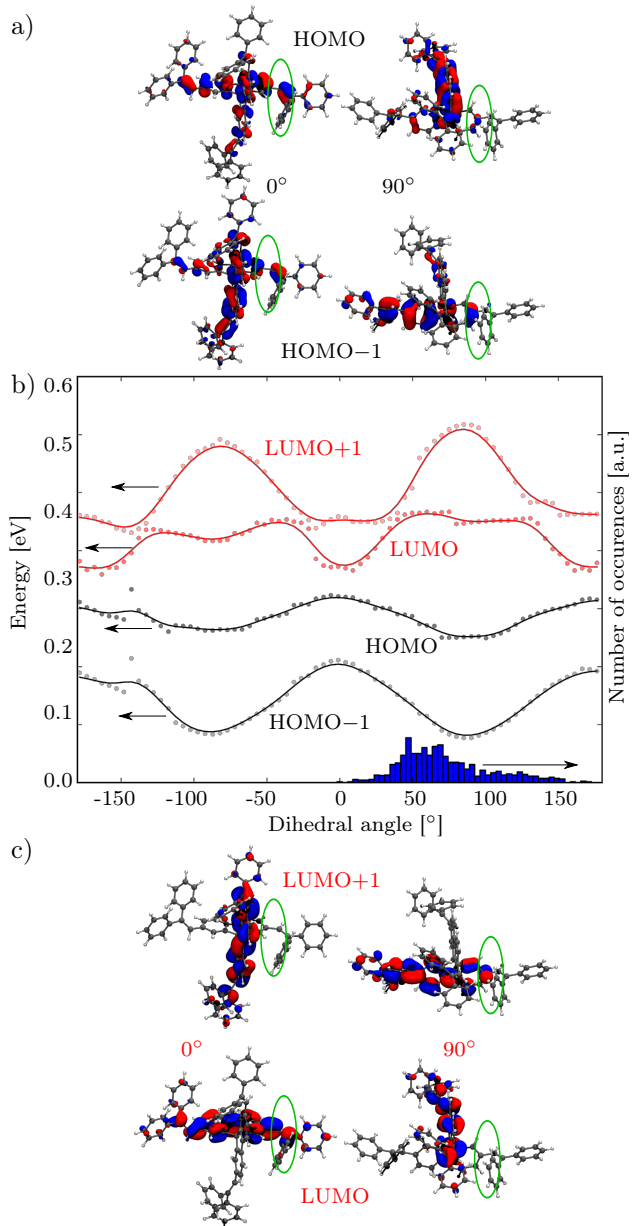
Figure F.5: a) HOMO−1 and HOMO orbitals at dihedral angles of 0° and 90°. The distribution of dihedral angles in an amorphous morphology is shown as a histogram. b) Dihedral potential for two occupied and two unoccupied frontier orbitals. c) LUMO and LUMO+1 orbitals at dihedral angles of 0° and 90°. The dihedral angle which is rotated is indicated in green. All other dihedral angles are relaxed. The energy scale is in eV but the orbital energies have an off-set and the HOMO-LUMO gap is decreased. The solid lines are a spline fit to the calculated data shown as points.

Bibliography

[1]   G. Li, R. Zhu, and Y. Yang. *Polymer solar cells.* Nat Photon 2012, 6(3), 153–161.

[2]   B. Kippelen and J.-L. Brédas. *Organic photovoltaics.* Energy Environ. Sci. 2009, 2(3), 251–261.

[3]   A. W. Hains, Z. Liang, M. A. Woodhouse, and B. A. Gregg. *Molecular semiconductors in organic photovoltaic cells.* Chemical reviews 2010, 110(11), 6689–6735.

[4]   C. N. Hoth, P. Schilinsky, S. A. Choulis, S. Balasubramanian, and C. J. Brabec. *Solution-processed organic photovoltaics. Applications of Organic and Printed Electronics.* Springer, 2013, 27–56.

[5]   C. Groves. *Organic light-emitting diodes: Bright design.* Nature Materials 2013, 12(7), 597–598.

[6]   T. Kalyani and S. Dhoble. *Organic light emitting diodes: Energy saving lighting technology - A review.* Renewable & Sustainable Energy Reviews 2012, 16(5), 2696–2723.

[7]   C. D. Dimitrakopoulos and P. R. Malenfant. *Organic thin film transistors for large area electronics.* Advanced Materials 2002, 14(2), 99–117.

[8]   I. G. Lezama and A. F. Morpurgo. *Progress in organic single-crystal field-effect transistors.* MRS bulletin 2013, 38(01), 51–56.

[9]   http://www.nrel.gov/ncpv.

[10] M. A. Green, K. Emery, Y. Hishikawa, W. Warta, and E. D. Dunlop. *Solar cell efficiency tables (version 47).* Progress in Photovoltaics: Research and Applications 2016, 24.

[11] V. Fiore, P. Battiato, S. Abdinia, S. Jacobs, I. Chartier, R. Coppard, G. Klink, E. Cantatore, E. Ragonese, and G. Palmisano. *An integrated 13.56 MHz RFID tag in a printed organic complementary TFT technology on flexible substrate.* IEEE Transactions on Circuits and Systems I: Regular Papers 2015, 62(6), 1668–1677.

[12] T. Neumann, D. Danilov, C. Lennartz, and W. Wenzel. *Modeling disordered morphologies in organic semiconductors.* Journal of Computational Chemistry 2013, 34(31), 2716–2725.

[13] T. Neumann. *Simulation of structural and electronic properties of nanoscale systems.* PhD thesis. Institut für Nanotechnologie, Karlsruhe Institut für Technologie (KIT), 2016.

[14] V. Rodin, F. Symalla, P. Friederich, V. Meded, D. Danilov, A. Poschlad, G. Nelles, F. von Wrochem, and W. Wenzel. *A generalized effective medium model for the carrier mobility in amorphous organic semiconducturs.* Physical Review B 2015, 91(15), 155203.

[15] T. Schneider, F. Limberg, K. Yao, A. Armin, N. Jürgensen, J. Czolk, B. Ebenhoch, P. Friederich, W. Wenzel, J. Behrends, H. Krüger, and A. Colsmann. *p-Doping of polystyrene polymers with attached functional side-groups from solution.* Submitted to the Journal of Materials Chemistry C 2016.

[16] P. Friederich, V. Rodin, F. von Wrochem, and W. Wenzel. *Theoretical investigation of the giant surface potential effect in amorphous organic semiconductors.* In preparation 2016.

[17] Z. Karipidou, B. Branchi, M. Sarpasan, N. Knorr, V. Rodin, P. Friederich, T. Neumann, V. Meded, S. Rosselli, G. Nelles, W. Wenzel, M. A. Rampi, and F. von Wrochem. *Ultrarobust Thin-Film Devices from Self-Assembled Metal-Terpyridine Oligomers.* Advanced Materials 2016, 28(18), 3473–3480.

[18] T. Neumann, J. Liu, T. Wächter, P. Friederich, F. Symalla, A. Welle, V. Mugnaini, V. Meded, M. Zharnikov, C. Wöll, and W. Wenzel. *Superexchange Charge Transport in Loaded Metal Organic Frameworks.* ACS nano 2016, 10(7), 7085–7093.

[19] F. Symalla, P. Friederich, A. Massé, V. Meded, P. A. Bobbert, and W. Wenzel. *Long range hopping mechanism for charge transport in doped organic semiconductors.* Submitted to PRL 2016.

[20] A. Massé, P. Friederich, F. Symalla, F. Liu, R. Nitsche, R. Coehoorn, W. Wenzel, and P. A. Bobbert. *Ab initio charge-carrier mobility model for amorphous molecular semiconductors.* Physical Review B 2016, 93(19), 195209.

[21] A. Massé, P. Friederich, V. Meded, W. Wenzel, and P. A. Bobbert. *The role of correlations in disordered organic systems.* In preparation 2016.

[22] A. D. Becke. *A new mixing of Hartree-Fock and local density-functional theories.* The Journal of Chemical Physics 1993, 98(2), 1372–1377.

[23] A. Schafer, H. Horn, and R. Ahlrichs. *Fully optimized contracted Gaussian basis sets for atoms Li to Kr.* The Journal of Chemical Physics 1992, 97(4), 2571–2577.

[24] *TURBOMOLE V6.5 2013, a development of University of Karlsruhe and Forschungszentrum Karlsruhe GmbH, 1989-2007, TURBOMOLE GmbH, since 2007; available from* http://www.turbomole.com.

[25] M. Hiramoto, H. Fujiwara, and M. Yokoyama. *Three-layered organic solar cell with a photoactive interlayer of codeposited pigments.* Applied physics letters 1991, 58(10), 1062–1064.

[26] G. Yu, J. Gao, J. C. Hummelen, F. Wudl, and A. J. Heeger. *Polymer photovoltiac cells: Enhanced efficiencies via a network of internal donor-acceptor heterojunctions.* Science 1995, 270(5243), 1789.

[27] H. W. Kroto, J. R. Heath, S. C. O'Brien, R. F. Curl, and R. E. Smalley. C_{60}: *buckminsterfullerene.* Nature 1985, 318(6042), 162–163.

[28] Q. Zhang, B. Kan, F. Liu, G. Long, X. Wan, X. Chen, Y. Zuo, W. Ni, H. Zhang, M. Li, Z. Hu, F. Huang, Y. Cao, Z. Liang, M. Zhang, T. P. Russell, and Y. Chen. *Small-molecule solar cells with efficiency over 9%.* Nature Photonics 2015, 9(1), 35–41.

[29] S. Rohr. *Heliatek consolidates its technology leadership by establishing a new world record for organic solar technology with a cell efficiency of 12%.* Heliatek. Heliatek GmbH 2013, 16.

[30] M. C. Scharber, D. Mühlbacher, M. Koppe, P. Denk, C. Waldauf, A. J. Heeger, and C. J. Brabec. *Design rules for donors in bulk-heterojunction solar cells-Towards 10% energy-conversion efficiency.* Advanced materials 2006, 18(6), 789–794.

[31] G. Dennler, M. C. Scharber, T. Ameri, P. Denk, K. Forberich, C. Waldauf, and C. J. Brabec. *Design Rules for Donors in Bulk-Heterojunction Tandem Solar Cells Towards 15% Energy-Conversion Efficiency.* Advanced Materials 2008, 20(3), 579–583.

[32] H. Yersin, A. F. Rausch, R. Czerwieniec, T. Hofbeck, and T. Fischer. *The triplet state of organo-transition metal compounds. Triplet harvesting and singlet harvesting for efficient OLEDs.* Coordination Chemistry Reviews 2011, 255(21), 2622–2652.

[33] M. A. Baldo, D. O'brien, Y You, A Shoustikov, S Sibley, M. Thompson, and S. Forrest. *Highly efficient phosphorescent emission from organic electroluminescent devices.* Nature 1998, 395(6698), 151–154.

[34] M. Baldo, S. Lamansky, P. Burrows, M. Thompson, and S. Forrest. *Very high-efficiency green organic light-emitting devices based on electrophosphorescence.* Applied Physics Letters 1999, 75, 4.

[35] F. B. Dias, K. N. Bourdakos, V. Jankus, K. C. Moss, K. T. Kamtekar, V. Bhalla, J. Santos, M. R. Bryce, and A. P. Monkman. *Triplet harvesting with 100% efficiency by way of thermally activated delayed fluorescence in charge transfer OLED emitters.* Advanced Materials 2013, 25(27), 3707–3714.

[36] Y. Tao, K. Yuan, T. Chen, P. Xu, H. Li, R. Chen, C. Zheng, L. Zhang, and W. Huang. *Thermally activated delayed fluorescence materials towards the breakthrough of organoelectronics.* Advanced Materials 2014, 26(47), 7931–7958.

[37] M. P. GAJ, C. FUENTES-HERNANDEZ, Y. ZHANG, S. R. MARDER, AND B. KIPPELEN. *Highly efficient organic light-emitting diodes from thermally activated delayed fluorescence using a sulfone–carbazole host material.* Organic Electronics 2015, 16, 109–112.

[38] S. Y. LEE, T. YASUDA, H. KOMIYAMA, J. LEE, AND C. ADACHI. *Thermally Activated Delayed Fluorescence Polymers for Efficient Solution-Processed Organic Light-Emitting Diodes.* Advanced Materials 2016, 28(21), 4019–4024.

[39] V. ADAMOVICH, J. BROOKS, A. TAMAYO, A. M. ALEXANDER, P. I. DJUROVICH, B. W. D'ANDRADE, C. ADACHI, S. R. FORREST, AND M. E. THOMPSON. *High efficiency single dopant white electrophosphorescent light emitting diodes.* New journal of chemistry 2002, 26(9), 1171–1178.

[40] B. W. DANDRADE, J. BROOKS, V. ADAMOVICH, M. E. THOMPSON, AND S. R. FORREST. *White Light Emission Using Triplet Excimers in Electrophosphorescent Organic Light-Emitting Devices.* Advanced Materials 2002, 14(15), 1032–1036.

[41] C.-I. CHAO AND S.-A. CHEN. *White light emission from exciplex in a bilayer device with two blue light-emitting polymers.* Applied physics letters 1998, 73(4), 426–428.

[42] J. FENG, F. LI, W. GAO, S. LIU, Y. LIU, AND Y. WANG. *White light emission from exciplex using tris-(8-hydroxyquinoline) aluminum as chromaticity-tuning layer.* Applied Physics Letters 2001, 78(25), 3947–3949.

[43] M MAZZEO, D PISIGNANO, F DELLA SALA, J THOMPSON, R. BLYTH, G GIGLI, R CINGOLANI, G SOTGIU, AND G BARBARELLA. *Organic single-layer white light-emitting diodes by exciplex emission from spin-coated blends of blue-emitting molecules.* Applied physics letters 2003, 82(3), 334–336.

[44] E. L. WILLIAMS, K. HAAVISTO, J. LI, AND G. E. JABBOUR. *Excimer-based white phosphorescent organic light-emitting diodes with nearly 100% internal quantum efficiency.* Advanced Materials 2007, 19(2), 197–202.

143

[45] M. Flämmich, J. Frischeisen, D. S. Setz, D. Michaelis, B. C. Krummacher, T. D. Schmidt, W. Brütting, and N. Danz. *Oriented phosphorescent emitters boost OLED efficiency*. Organic Electronics 2011, 12(10), 1663–1668.

[46] M. J. Jurow, C. Mayr, T. D. Schmidt, T. Lampe, P. I. Djurovich, W. Brütting, and M. E. Thompson. *Understanding and predicting the orientation of heteroleptic phosphors in organic light-emitting materials*. Nature materials 2015.

[47] B. Baumeier, O. Stenzel, C. Poelking, D. Andrienko, and V. Schmidt. *Stochastic modeling of molecular charge transport networks*. Physical Review B 2012, 86(18), 184202.

[48] H Bässler. *Charge transport in disordered organic photoconductors a Monte Carlo simulation study*. physica status solidi (b) 1993, 175(1), 15–56.

[49] W. Pasveer, J. Cottaar, C. Tanase, R. Coehoorn, P. A. Bobbert, P. Blom, D. De Leeuw, and M. Michels. *Unified description of charge-carrier mobilities in disordered semiconducting polymers*. Physical review letters 2005, 94(20), 206601.

[50] V. Coropceanu, J. Cornil, D. A. da Silva Filho, Y. Olivier, R. Silbey, and J.-L. Brédas. *Charge transport in organic semiconductors*. Chemical reviews 2007, 107(4), 926–952.

[51] W. Pasveer, J. Cottaar, C. Tanase, R. Coehoorn, P. A. Bobbert, P. Blom, D. De Leeuw, and M. Michels. *Unified description of charge-carrier mobilities in disordered semiconducting polymers*. Physical review letters 2005, 94(20), 206601.

[52] H Bässler. *Localized states and electronic transport in single component organic solids with diagonal disorder*. physica status solidi (b) 1981, 107(1), 9–54.

[53] H Bässler. *Charge transport in disordered organic photoconductors a Monte Carlo simulation study*. physica status solidi (b) 1993, 175(1), 15–56.

144

[54] A. Miller and E. Abrahams. *Impurity conduction at low concentrations.* Physical Review 1960, 120(3), 745.

[55] R. A. Marcus. *On the Theory of Oxidation-Reduction Reactions Involving Electron Transfer. I.* The Journal of Chemical Physics 1956, 24(5), 966–978.

[56] R. A. Marcus. *Electrostatic free energy and other properties of states having nonequilibrium polarization. I.* The Journal of Chemical Physics 1956, 24, 979.

[57] A. Fuchs, T. Steinbrecher, M. S. Mommer, Y. Nagata, M. Elstner, and C. Lennartz. *Molecular origin of differences in hole and electron mobility in amorphous Alq$_3$ - a multiscale simulation study.* Physical Chemistry Chemical Physics 2012, 14(12), 4259–4270.

[58] S. Arrhenius. *Über die Dissociationswärme und den Einfluss der Temperatur auf den Dissociationsgrad der Elektrolyte.* Wilhelm Engelmann, 1889.

[59] S. Arrhenius. *Über die Reaktionsgeschwindigkeit bei der Inversion von Rohrzucker durch Säuren.* Zeitschrift für physikalische Chemie 1889, 4, 226–248.

[60] A. Troisi. *Charge transport in high mobility molecular semiconductors: classical models and new theories.* Chemical Society Reviews 2011, 40(5), 2347–2358.

[61] P.-O. Löwdin. *On the non-orthogonality problem connected with the use of atomic wave functions in the theory of molecules and crystals.* The Journal of Chemical Physics 1950, 18, 365.

[62] V. Stehr, J. Pfister, R. F. Fink, B. Engels, and C. Deibel. *First-principles calculations of anisotropic charge-carrier mobilities in organic semiconductor crystals.* Phys. Rev. B 15 2011, 83, 155208.

[63] P. Kleine. *The effect of explicit charge and environment on transfer integrals in disordered organic semiconductors.* Master's thesis. Karlsruhe Institute of Technology, Institute of Nanotechnology, 2014.

[64] S. F. NELSEN, S. C. BLACKSTOCK, AND Y. KIM. *Estimation of inner shell Marcus terms for amino nitrogen compounds by molecular orbital calculations.* Journal of the American Chemical Society 1987, 109(3), 677–682.

[65] V. RÜHLE, A. LUKYANOV, F. MAY, M. SCHRADER, T. VEHOFF, J. KIRKPATRICK, B. BAUMEIER, AND D. ANDRIENKO. *Microscopic simulations of charge transport in disordered organic semiconductors.* Journal of chemical theory and computation 2011, 7(10), 3335–3345.

[66] D. P. MCMAHON AND A. TROISI. *Evaluation of the external reorganization energy of polyacenes.* The Journal of Physical Chemistry Letters 2010, 1(6), 941–946.

[67] J. E. NORTON AND J.-L. BRÉDAS. *Polarization energies in oligoacene semiconductor crystals.* Journal of the American Chemical Society 2008, 130(37), 12377–12384.

[68] P. FRIEDERICH, F. SYMALLA, V. MEDED, T. NEUMANN, AND W. WENZEL. *Ab Initio Treatment of Disorder Effects in Amorphous Organic Materials: Toward Parameter Free Materials Simulation.* Journal of Chemical Theory and Computation 2014, 10(9), 3720–3725.

[69] P. FRIEDERICH. *Simulation of energetic disorder and charge transport in amorphous organic semiconductors.* Master's thesis. Karlsruhe Institute of Technology, Institute of Nanotechnology, 2013.

[70] R. COEHOORN, W. PASVEER, P. BOBBERT, AND M. MICHELS. *Charge-carrier concentration dependence of the hopping mobility in organic materials with Gaussian disorder.* Physical Review B 2005, 72(15), 155206.

[71] R. SCHMECHEL. *Gaussian disorder model for high carrier densities: Theoretical aspects and application to experiments.* Physical Review B 2002, 66(23), 235206.

[72] R. H. YOUNG. *Dipolar lattice model of disorder in random media analytical evaluation of the gaussian disorder model.* Philosophical Magazine Part B 1995, 72(4), 435–457.

[73] Y. N. GARTSTEIN AND E. CONWELL. *High-field hopping mobility in molecular systems with spatially correlated energetic disorder*. Chemical Physics Letters 1995, 245(4), 351–358.

[74] M BOUHASSOUNE, S. VAN MENSFOORT, P. BOBBERT, AND R. COEHOORN. *Carrier-density and field-dependent charge-carrier mobility in organic semiconductors with correlated Gaussian disorder*. Organic Electronics 2009, 10(3), 437–445.

[75] A DIECKMANN, H BÄSSLER, AND P. BORSENBERGER. *An assessment of the role of dipoles on the density-of-states function of disordered molecular solids*. The Journal of chemical physics 1993, 99(10), 8136–8141.

[76] M. VISSENBERG AND M MATTERS. *Theory of the field-effect mobility in amorphous organic transistors*. Physical Review B 1998, 57(20), 12964.

[77] O TAL, Y ROSENWAKS, Y PREEZANT, N TESSLER, C. CHAN, AND A KAHN. *Direct determination of the hole density of states in undoped and doped amorphous organic films with high lateral resolution*. Physical review letters 2005, 95(25), 256405.

[78] W. L. KALB, S. HAAS, C. KRELLNER, T. MATHIS, AND B. BATLOGG. *Trap density of states in small-molecule organic semiconductors: A quantitative comparison of thin-film transistors with single crystals*. Physical Review B 2010, 81(15), 155315.

[79] R. L. MARTIN, J. D. KRESS, I. H. CAMPBELL, AND D. L. SMITH. *Molecular and solid-state properties of tris-(8-hydroxyquinolate)-aluminum*. Phys. Rev. B 2000, 61(23), 15804–15811.

[80] G. G. MALLIARAS, Y. SHEN, D. H. DUNLAP, H. MURATA, AND Z. KAFAFI. *Nondispersive electron transport in Alq_3*. Applied Physics Letters 2001, 79(16), 2582–2584.

[81] S. DIFLEY, L.-P. WANG, S. YEGANEH, S. R. YOST, AND T. VAN VOORHIS. *Electronic properties of disordered organic semiconductors via QM/MM simulations*. Accounts of chemical research 2010, 43(7), 995–1004.

[82] Q. WU AND T. VAN VOORHIS. *Direct calculation of electron transfer parameters through constrained density functional theory*. The Journal of Physical Chemistry A 2006, 110(29), 9212–9218.

[83] T. VAN VOORHIS, T. KOWALCZYK, B. KADUK, L.-P. WANG, C.-L. CHENG, AND Q. WU. *The diabatic picture of electron transfer, reaction barriers, and molecular dynamics.* Annual review of physical chemistry 2010, 61, 149–170.

[84] Q. WU AND T. VAN VOORHIS. *Direct optimization method to study constrained systems within density-functional theory.* Physical Review A 2005, 72(2), 024502.

[85] P. SCHWENN, P. BURN, AND B. POWELL. *Calculation of solid state molecular ionisation energies and electron affinities for organic semiconductors.* Organic Electronics 2011, 12(2), 394 –403.

[86] V. RÜHLE, A. LUKYANOV, F. MAY, M. SCHRADER, T. VEHOFF, J. KIRKPATRICK, B. BAUMEIER, AND D. ANDRIENKO. *Microscopic Simulations of Charge Transport in Disordered Organic Semiconductors.* Journal of Chemical Theory and Computation 2011, 7(10), 3335–3345.

[87] P. REN AND J. W. PONDER. *Consistent treatment of inter-and intramolecular polarization in molecular mechanics calculations.* Journal of computational chemistry 2002, 23(16), 1497–1506.

[88] P. REN AND J. W. PONDER. *Polarizable atomic multipole water model for molecular mechanics simulation.* The Journal of Physical Chemistry B 2003, 107(24), 5933–5947.

[89] J. W. PONDER, C. WU, P. REN, V. S. PANDE, J. D. CHODERA, M. J. SCHNIEDERS, I. HAQUE, D. L. MOBLEY, D. S. LAMBRECHT, R. A. DISTASIO, M. HEAD-GORDON, G. N. I. CLARK, M. E. JOHNSON, AND T. HEAD-GORDON. *Current status of the AMOEBA polarizable force field.* The Journal of Physical Chemistry B 2010, 114(8), 2549–2564.

[90] J. KWIATKOWSKI, J. NELSON, H. LI, J.-L. BREDAS, W. WENZEL, AND C. LENNARTZ. *Simulating charge transport in tris (8-hydroxyquinoline) aluminium (Alq$_3$).* Physical Chemistry Chemical Physics 2008, 10(14), 1852–1858.

[91] J. ÅQVIST AND A. WARSHEL. *Simulation of enzyme reactions using valence bond force fields and other hybrid quantum/classical approaches.* Chemical reviews 1993, 93(7), 2523–2544.

[92] J. E. Norton and J.-L. Brédas. *Polarization energies in oligoacene semiconductor crystals.* Journal of the American Chemical Society 2008, 130(37), 12377–12384.

[93] J Frenkel. *On pre-breakdown phenomena in insulators and electronic semi-conductors.* Physical Review 1938, 54(8), 647.

[94] R. Hall. *The Poole-Frenkel effect.* Thin Solid Films 1971, 8(4), 263–271.

[95] I. Fishchuk, A. Kadashchuk, S. Hoffmann, S Athanasopoulos, J. Genoe, H Bässler, and A Köhler. *Unified description for hopping transport in organic semiconductors including both energetic disorder and polaronic contributions.* Physical Review B 2013, 88(12), 125202.

[96] S. Baranovskii. *Theoretical description of charge transport in disordered organic semiconductors.* physica status solidi (b) 2014, 251(3), 487–525.

[97] J. Cottaar, L. Koster, R. Coehoorn, and P. A. Bobbert. *Scaling theory for percolative charge transport in disordered molecular semiconductors.* Physical Review Letters 2011, 107(13), 136601.

[98] A Massé, R Coehoorn, and P. Bobbert. *Universal size-dependent conductance fluctuations in disordered organic semiconductors.* Physical review letters 2014, 113(11), 116604.

[99] Y. Roichman, Y. Preezant, and N. Tessler. *Analysis and modeling of organic devices.* physica status solidi (a) 2004, 201(6), 1246–1262.

[100] M. Van der Auweraer, F. C. De Schryver, P. M. Borsenberger, and H. Bässler. *Disorder in charge transport in doped polymers.* Advanced materials 1994, 6(3), 199–213.

[101] J. Holland-Cunz. *Simulation of exciton dissociation and charge transport in disordered amorphous semiconductor junctions.* Master's thesis. Karlsruhe Institute of Technology, Institute of Nanotechnology, 2016.

[102] F. Symalla. *The effect of super-exchange on charge transport in organic electronics.* PhD thesis. Karlsruhe Institute of Technology, Institute of Nanotechnology, To be submitted in 2017.

[103] L. H. Thomas. *The calculation of atomic fields.* Mathematical Proceedings of the Cambridge Philosophical Society 05 1927, 23, 542–548.

[104] P. HOHENBERG AND W. KOHN. *Inhomogeneous Electron Gas*. Phys. Rev. 3B 1964, 136, B864–B871.

[105] W. KOHN AND L. J. SHAM. *Self-Consistent Equations Including Exchange and Correlation Effects*. Phys. Rev. 4A 1965, 140, A1133–A1138.

[106] W. BRÜTTTING. *Physics of Organic Semiconductors*. Erste Auflage. Weinheim: Wiley-VCH, 2005.

[107] A. D. BECKE. *Density-functional exchange-energy approximation with correct asymptotic behavior*. Phys. Rev. A 1988, 38(6), 3098–3100.

[108] J. P. PERDEW. *Density-functional approximation for the correlation energy of the inhomogeneous electron gas*. Phys. Rev. B 1986, 33(12), 8822–8824.

[109] C. LEE, W. YANG, AND R. G. PARR. *Development of the Colle-Salvetti correlation-energy formula into a functional of the electron density*. Physical review B 1988, 37(2), 785.

[110] S. H. VOSKO, L. WILK, AND M. NUSAIR. *Accurate spin-dependent electron liquid correlation energies for local spin density calculations: a critical analysis*. Canadian Journal of physics 1980, 58(8), 1200–1211.

[111] J. C. SLATER. *Atomic shielding constants*. Physical Review 1930, 36(1), 57.

[112] S. F. BOYS. *Electronic Wave Functions. I. A General Method of Calculation for the Stationary States of Any Molecular System*. Proceedings of the Royal Society of London. Series A, Mathematical and Physical Sciences 1950, 200(1063), pp. 542–554.

[113] P. M. GILL. *Molecular integrals Over Gaussian Basis Functions*. Ed. by J. R. Sabin and M. C. Zerner. Vol. 25. Advances in Quantum Chemistry. Academic Press, 1994, 141 –205.

[114] W. J. HEHRE, R. F. STEWART, AND J. A. POPLE. *Self-Consistent Molecular-Orbital Methods. I. Use of Gaussian Expansions of Slater-Type Atomic Orbitals*. The Journal of Chemical Physics 1969, 51(6), 2657–2664.

[115] R. Ditchfield, W. J. Hehre, and J. A. Pople. *Self-Consistent Molecular-Orbital Methods. IX. An Extended Gaussian-Type Basis for Molecular-Orbital Studies of Organic Molecules.* The Journal of Chemical Physics 1971, 54(2), 724–728.

[116] M. J. Frisch, J. A. Pople, and J. S. Binkley. *Self-consistent molecular orbital methods 25. Supplementary functions for Gaussian basis sets.* The Journal of Chemical Physics 1984, 80(7), 3265–3269.

[117] A. Schafer, C. Huber, and R. Ahlrichs. *Fully optimized contracted Gaussian basis sets of triple zeta valence quality for atoms Li to Kr.* The Journal of Chemical Physics 1994, 100(8), 5829–5835.

[118] W. D. Cornell, P. Cieplak, C. I. Bayly, I. R. Gould, K. M. Merz, D. M. Ferguson, D. C. Spellmeyer, T. Fox, J. W. Caldwell, and P. A. Kollman. *A second generation force field for the simulation of proteins, nucleic acids, and organic molecules.* Journal of the American Chemical Society 1995, 117(19), 5179–5197.

[119] A. D. MacKerell, D. Bashford, M. Bellott, R. L. Dunbrack, J. D. Evanseck, M. J. Field, S. Fischer, J. Gao, H. Guo, S. Ha, D. Joseph-McCarthy, L. Kuchnir, K. Kuczera, F. T. K. Lau, C. Mattos, S. Michnick, T. Ngo, D. T. Nguyen, B. Prodhom, W. E. Reiher, B. Roux, M. Schlenkrich, J. C. Smith, R. Stote, J. Straub, M. Watanabe, J. Wiórkiewicz-Kuczera, D. Yin, and M. Karplus. *All-atom empirical potential for molecular modeling and dynamics studies of proteins.* The journal of physical chemistry B 1998, 102(18), 3586–3616.

[120] A. D. MacKerell, M. Feig, and C. L. Brooks. *Extending the treatment of backbone energetics in protein force fields: Limitations of gas-phase quantum mechanics in reproducing protein conformational distributions in molecular dynamics simulations.* Journal of computational chemistry 2004, 25(11), 1400–1415.

[121] A. Lukyanov, C. Lennartz, and D. Andrienko. *Amorphous films of tris (8-hydroxyquinolinato) aluminium: Force-field, morphology, and charge transport.* physica status solidi (a) 2009, 206(12), 2737–2742.

151

[122] R. S. MULLIKEN. *Electronic Population Analysis on LCAO-MO Molecular Wave Functions. I.* Journal of Chemical Physics 1955, 23, 1833–1840.

[123] U. C. SINGH AND P. A. KOLLMAN. *An approach to computing electrostatic charges for molecules.* Journal of Computational Chemistry 1984, 5(2), 129–145.

[124] B. H. BESLER, K. M. MERZ, AND P. A. KOLLMAN. *Atomic charges derived from semiempirical methods.* Journal of Computational Chemistry 1990, 11(4), 431–439.

[125] C. LEE, R. WATERLAND, AND K. SOHLBERG. *Prediction of Charge Mobility in Amorphous Organic Materials through the Application of Hopping Theory.* Journal of Chemical Theory and Computation 2011, 7(8), 2556–2567.

[126] P. KORDT, J. J. VAN DER HOLST, M. AL HELWI, W. KOWALSKY, F. MAY, A. BADINSKI, C. LENNARTZ, AND D. ANDRIENKO. *Modeling of organic light emitting diodes: From molecular to device properties.* Advanced Functional Materials 2015, 25(13), 1955–1971.

[127] B. BAUMEIER, F. MAY, C. LENNARTZ, AND D. ANDRIENKO. *Challenges for in silico design of organic semiconductors.* Journal of Materials Chemistry 2012, 22(22), 10971–10976.

[128] S. M. RYNO, C. RISKO, AND J.-L. BRÉDAS. *Impact of molecular packing on electronic polarization in organic crystals: the case of pentacene vs TIPS-pentacene.* Journal of the American Chemical Society 2014, 136(17), 6421–6427.

[129] P. FRIEDERICH, V. MEDED, F. SYMALLA, M. ELSTNER, AND W. WENZEL. *A QM/QM approach to model energy disorder in amorphous organic semiconductors.* Journal of Chemical Theory and Computation 2015, 11(2), 560567.

[130] P. FRIEDERICH, T. STRUNK, W. WENZEL, AND I. KONDOV. *Multiscale Simulation of Organic Electronics Via Smart Scheduling of Quantum Mechanics Computations.* Procedia Computer Science 2016, 80, 1244–1254.

[131] P. FRIEDERICH, V. MEDED, A. POSCHLAD, T. NEUMANN, V. RODIN, V. STEHR, F. SYMALLA, D. DANILOV, G. LÜDEMANN, R. F. FINK, I. KONDOV, F. VON WROCHEM, AND W. WENZEL. *Molecular Origin of the Charge Carrier Mobility in Small Molecule Organic Semiconductors.* Advanced Functional Materials 2016, 26(31), 5757–5763.

[132] T. MÖNCH, P. FRIEDERICH, F. HOLZMÜELLER, B. RUTKOWSKI, J. BENDUHN, T. STRUNK, C. KÖRNER, K. VANDEWAL, A. CZYRSKA-FILEMONOWICZ, W. WENZEL, AND K. LEO. *Influence of Meso and Nanoscale Structure on the Properties of Highly Efficient Small Molecule Solar Cells.* Advanced Energy Materials 2015.

[133] T. MÖNCH, P. FORMANEK, J. A. KOSTER, P. FRIEDERICH, M. RIEDE, C. KÖRNER, K. VANDEWAL, W. WENZEL, AND K. LEO. *Microscopic investigations on ZnPc:C_{60} blends.* Organic Electronics 2015, 27, 183–191.

[134] A. MASSÉ, R. COEHOORN, AND P. A. BOBBERT. *Universal Size-Dependent Conductance Fluctuations in Disordered Organic Semiconductors.* Phys. Rev. Lett. 11 2014, 113, 116604.

[135] W. L. JORGENSEN AND J. TIRADO-RIVES. *The OPLS [optimized potentials for liquid simulations] potential functions for proteins, energy minimizations for crystals of cyclic peptides and crambin.* Journal of the American Chemical Society 1988, 110(6), 1657–1666.

[136] J. WANG, R. M. WOLF, J. W. CALDWELL, P. A. KOLLMAN, AND D. A. CASE. *Development and testing of a general amber force field.* Journal of computational chemistry 2004, 25(9), 1157–1174.

[137] T. STRUNK, M. WOLF, M. BRIEG, K. KLENIN, A. BIEWER, F. TRISTRAM, M. ERNST, P. KLEINE, N. HEILMANN, AND I. KONDOV. *SIMONA 1.0: An efficient and versatile framework for stochastic simulations of molecular and nanoscale systems.* Journal of Computational Chemistry 2012, 33(32), 2602–2613.

[138] B. J. ALDER AND T. E. WAINWRIGHT. *Studies in Molecular Dynamics. I. General Method.* The Journal of Chemical Physics 1959, 31(2), 459–466.

[139] A. RAHMAN. *Correlations in the Motion of Atoms in Liquid Argon.* Phys. Rev. 1964, 136(2A), A405–A411.

153

[140] H. J. BERENDSEN, D. VAN DER SPOEL, AND R. VAN DRUNEN. *GRO-MACS: a message-passing parallel molecular dynamics implementation.* Computer Physics Communications 1995, 91(1), 43–56.

[141] A. JAKALIAN, B. L. BUSH, D. B. JACK, AND C. I. BAYLY. *Fast, efficient generation of high-quality atomic Charges. AM1-BCC model: I. Method.* Journal of Computational Chemistry 2000, 21(2), 132–146.

[142] A. JAKALIAN, D. B. JACK, AND C. I. BAYLY. *Fast, efficient generation of high-quality atomic charges. AM1-BCC model: II. Parameterization and validation.* Journal of computational chemistry 2002, 23(16), 1623–1641.

[143] C. CALEMAN, P. J. VAN MAAREN, M. HONG, J. S. HUB, L. T. COSTA, AND D. VAN DER SPOEL. *Force field benchmark of organic liquids: density, enthalpy of vaporization, heat capacities, surface tension, isothermal compressibility, volumetric expansion coefficient, and dielectric constant.* Journal of chemical theory and computation 2011, 8(1), 61–74.

[144] J. WANG AND T. HOU. *Application of molecular dynamics simulations in molecular property prediction. 1. density and heat of vaporization.* Journal of chemical theory and computation 2011, 7(7), 2151–2165.

[145] V. MEDED, P. FRIEDERICH, F. SYMALLA, T. NEUMANN, D. DANILOV, AND W. WENZEL. *A self-consistent first-principle based approach to model carrier mobility in organic materials.* AIP Conf. Proc. 2016, 1702, 090027.

[146] T. A. WESOLOWSKI AND A. WARSHEL. *Frozen density functional approach for ab initio calculations of solvated molecules.* The Journal of Physical Chemistry 1993, 97(30), 8050–8053.

[147] T. A. WESOLOWSKI AND J. WEBER. *Kohn-Sham equations with constrained electron density: an iterative evaluation of the ground-state electron density of interacting molecules.* Chemical physics letters 1996, 248(1), 71–76.

[148] M. ELSTNER, D. POREZAG, G JUNGNICKEL, J ELSNER, M HAUGK, T. FRAUENHEIM, S. SUHAI, AND G. SEIFERT. *Self-consistent-charge density-functional tight-binding method for simulations of complex materials properties.* Physical Review B 1998, 58(11), 7260.

154

[149] J. JORTNER, M. BIXON, T. LANGENBACHER, AND M. E. MICHEL-BEYERLE. *Charge transfer and transport in DNA*. Proceedings of the National Academy of Sciences 1998, 95(22), 12759–12765.

[150] C. LAMBERT, G. NÖLL, AND J. SCHELTER. *Bridge-mediated hopping or superexchange electron-transfer processes in bis (triarylamine) systems*. Nature materials 2002, 1(1), 69–73.

[151] R. E. RUDD AND J. Q. BROUGHTON. *Coarse-grained molecular dynamics and the atomic limit of finite elements*. Physical Review B 1998, 58(10), R5893.

[152] K. A. SCOTT, P. J. BOND, A. IVETAC, A. P. CHETWYND, S. KHALID, AND M. S. SANSOM. *Coarse-grained MD simulations of membrane protein-bilayer self-assembly*. Structure 2008, 16(4), 621–630.

[153] S. J. MARRINK, H. J. RISSELADA, S. YEFIMOV, D. P. TIELEMAN, AND A. H. DE VRIES. *The MARTINI force field: coarse grained model for biomolecular simulations*. The Journal of Physical Chemistry B 2007, 111(27), 7812–7824.

[154] N. SINGH, U. RAI, AND O. SINGH. *Chemistry of eutectic and monotectic; phenanthrene-succinonitrile system*. Journal of crystal growth 1985, 71(2), 353–360.

[155] M. KONRAD. *Coarse-grained Monte Carlo simulations of morphology and phase-separation in binary organic systems*. Master's thesis. Karlsruhe Institute of Technology, Institute of Nanotechnology, To be submitted in 2017.

[156] N. KARL. *Studies of organic semiconductors for 40 years-III*. Molecular Crystals and Liquid Crystals 1989, 171(1), 31–51.

[157] W SHOCKLEY AND J BARDEEN. *Energy bands and mobilities in monatomic semiconductors*. Physical Review 1950, 77(3), 407.

[158] H. EHRENREICH. *Electron mobility of indium arsenide phosphide [In($As_y P_{1-y}$)]*. Journal of Physics and Chemistry of Solids 1959, 12(1), 97–104.

[159] M NEUBERGER. *III-V ternary semiconducting compounds-data tables*. Springer Science & Business Media, 2013.

[160] S. Naka, H. Okada, H. Onnagawa, Y. Yamaguchi, and T. Tsutsui. *Carrier transport properties of organic materials for EL device operation.* Synthetic metals 2000, 111, 331–333.

[161] H. Fong and S. So. *Hole transporting properties of tris (8-hydroxyquinoline) aluminum.* Journal of applied physics 2006, 100(9), 094502–094502.

[162] R. Kepler, P. Beeson, S. Jacobs, R. Anderson, M. Sinclair, V. Valencia, and P. Cahill. *Electron and hole mobility in tris (8-hydroxyquinolinolato-N1, O8) aluminum.* Applied physics letters 1995, 66(26), 3618–3620.

[163] J. Kalinowski, N. Camaioni, P. Di Marco, V. Fattori, and A. Martelli. *Kinetics of charge carrier recombination in organic light-emitting diodes.* Applied physics letters 1998, 72.

[164] S. Tse, K. Kwok, and S. So. *Electron transport in naphthylamine-based organic compounds.* Applied physics letters 2006, 89(26), 2102.

[165] K. Okumoto, K. Wayaku, T. Noda, H. Kageyama, and Y. Shirota. *Amorphous molecular materials: charge transport in the glassy state of N, N'-di (biphenylyl)-N, N'-diphenyl-[1, 1'-biphenyl]-4, 4'-diamines.* Synthetic metals 2000, 111, 473–476.

[166] S. Novikov, D. Dunlap, V. Kenkre, P. Parris, and A. Vannikov. *Essential role of correlations in governing charge transport in disordered organic materials.* Physical Review Letters 1998, 81(20), 4472.

[167] D. Huber. *Diffusion of optical excitation at finite temperatures.* The Journal of chemical physics 1983, 78(5), 2530–2532.

[168] S. Kaminski, M. Gaus, and M. Elstner. *Improved electronic properties from third-order SCC-DFTB with cost efficient post-SCF extensions.* The Journal of Physical Chemistry A 2012, 116(48), 11927–11937.

[169] S. Schiefer, M. Huth, A. Dobrinevski, and B. Nickel. *Determination of the crystal structure of substrate-induced pentacene polymorphs in fiber structured thin films.* Journal of the American Chemical Society 2007, 129(34), 10316–10317.

[170] H. H. Fong and S. K. So. *Hole transporting properties of tris(8-hydroxyquinoline) aluminum (Alq₃).* Journal of Applied Physics 2006, 100(9), 094502, 094502.

[171] A. G. Mückl, S. Berleb, W. Brütting, and M. Schwoerer. *Transient electroluminescence measurements on organic heterolayer light emitting diodes.* Synthetic metals 2000, 111, 91–94.

[172] P. Borsenberger and J. Shi. *Hole transport in a vapor deposited phenylenediamine molecular glass.* physica status solidi (b) 1995, 191(2), 461–469.

[173] T. Mori, E. Sugimura, and T. Mizutani. *Estimate of hole mobilities of some organic photoconducting materials using the time-of-flight method.* Journal of Physics D: Applied Physics 1993, 26(3), 452.

[174] M Stolka, J. Yanus, and D. Pai. *Hole transport in solid solutions of a diamine in polycarbonate.* The Journal of Physical Chemistry 1984, 88(20), 4707–4714.

[175] R. De Boer, T. Klapwijk, and A. Morpurgo. *Field-effect transistors on tetracene single crystals.* Applied physics letters 2003, 83(21), 4345–4347.

[176] H. Klauk, M. Halik, U. Zschieschang, G. Schmid, W. Radlik, and W. Weber. *High-mobility polymer gate dielectric pentacene thin film transistors.* Journal of Applied Physics 2002, 92(9), 5259–5263.

[177] S. Engelbrecht, M Prinz, T. Arend, and R Kersting. *Terahertz spectroscopy on hole transport in pentacene thin films.* Applied Physics Letters 2014, 105(1), 012101.

[178] H. Li, L. Duan, D. Zhang, and Y. Qiu. *Influence of Molecular Packing on Intramolecular Reorganization Energy: A Case Study of Small Molecules.* The Journal of Physical Chemistry C 2014, 118(27), 14848–14852.

[179] P. Borsenberger and H Bässler. *Concerning the role of dipolar disorder on charge transport in molecularly doped polymers.* The Journal of chemical physics 1991, 95(7), 5327–5331.

157

[180] K.-M. Weitzel and H Bässler. *Semiempirical treatment of the benzophenone molecule as a function of twist angle.* The Journal of chemical physics 1986, 84(3), 1590–1597.

[181] C. W. Tang and S. A. VanSlyke. *Organic electroluminescent diodes.* Applied physics letters 1987, 51(12), 913–915.

[182] T.-H. Lai, J. W. Lee, J. R. Manders, and F. So. *Multi-spectral imaging with infrared sensitive organic light emitting diode.* Scientific reports 2014, 4.

[183] J. Zou, K. Zhang, J. Li, Y. Zhao, Y. Wang, S. K. R. Pillai, H. V. Demir, X. Sun, M. B. Chan-Park, and Q. Zhang. *Carbon Nanotube Driver Circuit for 6×6 Organic Light Emitting Diode Display.* Scientific reports 2015, 5.

[184] H. Park, D.-S. Shin, H.-S. Yu, and H.-B. Chae. *Electron mobility in tris(8-hydroxyquinoline)aluminum (Alq$_3$) films by transient electroluminescence from single layer organic light emitting diodes.* Applied Physics Letters 2007, 90(20), 202103, 202103.

[185] J Cottaar, R Coehoorn, and P. Bobbert. *Scaling theory for percolative charge transport in molecular semiconductors: Correlated versus uncorrelated energetic disorder.* Physical Review B 2012, 85(24), 245205.

[186] S. Braun, W. R. Salaneck, and M. Fahlman. *Energy-level alignment at organic/metal and organic/organic interfaces.* Advanced Materials 2009, 21(14-15), 1450–1472.

[187] B. Lüssem, M. Riede, and K. Leo. *Doping of organic semiconductors.* physica status solidi (a) 2013, 210(1), 9–43.

[188] E. Ito, Y. Washizu, N. Hayashi, H. Ishii, N. Matsuie, K. Tsuboi, Y. Ouchi, Y. Harima, K. Yamashita, and K. Seki. *Spontaneous buildup of giant surface potential by vacuum deposition of Alq$_3$ and its removal by visible light irradiation.* Journal of applied physics 2002, 92, 7306–7310.

[189] T. Setzer, P. Friederich, F. Symalla, V. Meded, A. Dreuw, W. Wenzel, and C. Lennartz. *Enhancing the lifetime of blue emitters.* In preparation 2016.

158

[190] W. Ma, J. R. Tumbleston, M. Wang, E. Gann, F. Huang, and H. Ade. *Domain purity, miscibility, and molecular orientation at donor/-acceptor interfaces in high performance organic solar cells: paths to further improvement.* Advanced Energy Materials 2013, 3(7), 864–872.

[191] J. R. Tumbleston, B. A. Collins, L. Yang, A. C. Stuart, E. Gann, W. Ma, W. You, and H. Ade. *The influence of molecular orientation on organic bulk heterojunction solar cells.* Nature Photonics 2014, 8(5), 385–391.

[192] T. Mönch, P. Guttmann, J. Murawski, C. Elschner, M. Riede, L. Müller-Meskamp, and K. Leo. *Investigating local (photo-) current and structure of $ZnPc:C_{60}$ bulk-heterojunctions.* Organic Electronics 2013, 14(11), 2777–2788.

[193] D. Wynands, M. Levichkova, K. Leo, C. Uhrich, G. Schwartz, D. Hildebrandt, M. Pfeiffer, and M. Riede. *Increase in internal quantum efficiency in small molecular oligothiophene: C_{60} mixed heterojunction solar cells by substrate heating.* Applied Physics Letters 2010, 97(7), 3503.

[194] K. Schulze, C. Uhrich, R. Schüppel, K. Leo, M. Pfeiffer, E. Brier, E. Reinold, and P. Baeuerle. *Efficient Vacuum-Deposited Organic Solar Cells Based on a New Low-Bandgap Oligothiophene and Fullerene C_{60}.* Advanced Materials 2006, 18(21), 2872–2875.

[195] C. Koerner, C. Elschner, N. C. Miller, R. Fitzner, F. Selzer, E. Reinold, P. Bäuerle, M. F. Toney, M. D. McGehee, K. Leo, and M. Riede. *Probing the effect of substrate heating during deposition of $DCV4T:C_{60}$ blend layers for organic solar cells.* Organic Electronics 2012, 13(4), 623–631.

[196] C. Poelking, M. Tietze, C. Elschner, S. Olthof, D. Hertel, B. Baumeier, F. Würthner, K. Meerholz, K. Leo, and D. Andrienko. *Impact of mesoscale order on open-circuit voltage in organic solar cells.* Nature materials 2015, 14(4), 434–439.

[197] R. Fitzner, E. Reinold, A. Mishra, E. Mena-Osteritz, H. Ziehlke, C. Körner, K. Leo, M. Riede, M. Weil, O. Tsaryova, A. Weiss, C. Uhrich, M. Pfeiffer, and P. Bäuerle. *Dicyanovinyl–Substituted*

Oligothiophenes: Structure-Property Relationships and Application in Vacuum-Processed Small Molecule Organic Solar Cells. Advanced Functional Materials 2011, 21(5), 897–910.

[198] H. ZIEHLKE, L. BURTONE, C. KOERNER, R. FITZNER, E. REINOLD, P. BÄUERLE, K. LEO, AND M. RIEDE. *Increase of charge carrier lifetime in dicyanovinyl–quinquethiophene: fullerene blends upon deposition on heated substrates.* Organic Electronics 2011, 12(12), 2258–2267.

[199] R. SCHÜPPEL, K. SCHMIDT, C. UHRICH, K. SCHULZE, D. WYNANDS, J.-L. BRÉDAS, E. BRIER, E REINOLD, H.-B. BU, P. BÄUERLE, B. MÄNNIG, M. PFEIFFER, AND K LEO. *Optimizing organic photovoltaics using tailored heterojunctions: A photoinduced absorption study of oligothiophenes with low band gaps.* Physical Review B 2008, 77(8), 085311.

[200] R. MEERHEIM, C. KÖRNER, AND K. LEO. *Highly efficient organic multi-junction solar cells with a thiophene based donor material.* Applied Physics Letters 2014, 105(6), 063306.

[201] D. B. WILLIAMS AND C. B. CARTER. *High Energy-Loss Spectra and Images. Transmission Electron Microscopy.* Springer, 2009, 715–739.

[202] M. PFANNMÖLLER, H. FLÜGGE, G. BENNER, I. WACKER, C. SOMMER, M. HANSELMANN, S. SCHMALE, H. SCHMIDT, F. A. HAMPRECHT, T. RABE, W. KOWALSKY, AND R. R. SCHRÖDER. *Visualizing a homogeneous blend in bulk heterojunction polymer solar cells by analytical electron microscopy.* Nano letters 2011, 11(8), 3099–3107.

[203] J. B. GILCHRIST, T. BASEY-FISHER, S. C. CHANG, F. SCHELTENS, D. W. McCOMB, AND S. HEUTZ. *Uncovering buried structure and interfaces in molecular photovoltaics.* Advanced Functional Materials 2014, 24(41), 6473–6483.

[204] F. MAIER-FLAIG, C. KÜBEL, J. RINCK, T. BOCKSROCKER, T. SCHERER, R. PRANG, A. K. POWELL, G. A. OZIN, AND U LEMMER. *Looking inside a working SiLED.* Nano letters 2013, 13(8), 3539–3545.

[205] J. Wen, D. J. Miller, W. Chen, T. Xu, L. Yu, S. B. Darling, and N. J. Zaluzec. *Visualization of Hierarchical Nanodomains in Polymer/Fullerene Bulk Heterojunction Solar Cells*. Microscopy and Microanalysis 2014, 20(05), 1507–1513.

[206] P. K. Watkins, A. B. Walker, and G. L. Verschoor. *Dynamical Monte Carlo modelling of organic solar cells: the dependence of internal quantum efficiency on morphology*. Nano letters 2005, 5(9), 1814–1818.

[207] J. Wang, Z. Zhou, W. Zhang, T. M. Garoni, and Y. Deng. *Bond and site percolation in three dimensions*. Physical Review E 2013, 87(5), 052107.

[208] K. Malarz and S. Galam. *Square-lattice site percolation at increasing ranges of neighbor bonds*. Physical Review E 2005, 71(1), 016125.

[209] D. Wynands, B. Männig, M. Riede, K. Leo, E. Brier, E. Reinold, and P. Bäuerle. *Organic thin film photovoltaic cells based on planar and mixed heterojunctions between fullerene and a low bandgap oligothiophene*. Journal of Applied Physics 2009, 106(5), 4509.

[210] S.-B. Rim, R. F. Fink, J. C. Schöneboom, P. Erk, and P. Peumans. *Effect of molecular packing on the exciton diffusion length in organic solar cells*. Applied Physics Letters 2007, 91(17), 173504.

[211] P. Peumans, A. Yakimov, and S. R. Forrest. *Small molecular weight organic thin-film photodetectors and solar cells*. Journal of Applied Physics 2003, 93(7), 3693–3723.

[212] R. R. Lunt, J. B. Benziger, and S. R. Forrest. *Relationship between crystalline order and exciton diffusion length in molecular organic semiconductors*. Advanced Materials 2010, 22(11), 1233–1236.

[213] R. Fitzner, E. Mena-Osteritz, A. Mishra, G. Schulz, E. Reinold, M. Weil, C. Körner, H. Ziehlke, C. Elschner, K. Leo, M. Riede, M. Pfeiffer, C. Uhrich, and P. Bäuerle. *Correlation of π-conjugated oligomer structure with film morphology and organic solar cell performance*. Journal of the American Chemical Society 2012, 134(27), 11064–11067.

[214] A. MAGRI, P. FRIEDERICH, B. SCHÄFER, V. FATTORI, X. SUN, T. STRUNK, V. MEDED, L. E. HUESO, W. WENZEL, AND M. RUBEN. *Charge carriers mobility and electronic properties of Al(Op)$_3$: impact of excimer formation.* Beilstein Journal of Nanotechnology 2015, 6, 11071115.

[215] P. FRIEDERICH, M. JENNE, C. SPRAU, A. MAGRI, V. GÓMEZ, V. MEDED, F. SCHRAMM, A. COLSMANN, M. RUBEN, AND W. WENZEL. *Thin Film Charge Mobility of Alq$_3$-derivatives: Towards in-silico Rational Design in Organic Electronics.* In preparation 2016.

[216] R. AHLRICHS, M. BÄR, M. HÄSER, H. HORN, AND C. KÖLMEL. *TURBOMOLE, V5.* Chem. Phys. Lett 1989, 162, 165.

[217] G SEIFERT, D POREZAG, AND T. FRAUENHEIM. *Calculations of molecules, clusters, and solids with a simplified LCAO-DFT-LDA scheme.* International journal of quantum chemistry 1996, 58(2), 185–192.

[218] M. GAUS, Q. CUI, AND M. ELSTNER. *DFTB3: extension of the self-consistent-charge density-functional tight-binding method (SCC-DFTB).* J. Chem. Theory Comput 2011, 7(4), 931–948.

[219] M. BOUHASSOUNE, S. VAN MENSFOORT, P. A. BOBBERT, AND R. COEHOORN. *Carrier-density and field-dependent charge-carrier mobility in organic semiconductors with correlated Gaussian disorder.* Organic Electronics 2009, 10(3), 437–445.

[220] J. FLORES. *Transport in models with correlated diagonal and off-diagonal disorder.* Journal of Physics: Condensed Matter 1989, 1(44), 8471.

[221] Y. N. GARTSTEIN AND E. CONWELL. *High-field hopping mobility in molecular systems with spatially correlated energetic disorder.* Chemical Physics Letters 1995, 245(4), 351–358.

[222] D. DUNLAP, P. PARRIS, AND V. KENKRE. *Charge-dipole model for the universal field dependence of mobilities in molecularly doped polymers.* Physical review letters 1996, 77(3), 542.

[223] Y. NOGUCHI, N. SATO, Y. MIYAZAKI, AND H. ISHII. *Light-and ion-gauge-induced space charges in tris-(8-hydroxyquinolate) aluminum-based organic light-emitting diodes.* Applied Physics Letters 2010, 96(14), 143305.

[224] Y. Noguchi, H. Lim, T. Isoshima, E. Ito, M. Hara, W. W. Chin, J. W. Han, H. Kinjo, Y. Ozawa, Y. Nakayama, and H. Ishii. *Influence of the direction of spontaneous orientation polarization on the charge injection properties of organic light-emitting diodes*. Applied Physics Letters 2013, 102(20), 203306.

[225] Y. Noguchi, Y. Miyazaki, Y. Tanaka, N. Sato, Y. Nakayama, T. D. Schmidt, W. Brütting, and H. Ishii. *Charge accumulation at organic semiconductor interfaces due to a permanent dipole moment and its orientational order in bilayer devices*. Journal of Applied Physics 2012, 111(11), 114508.

L
List of Publications

ARTICLES

IN PREPARATION

ANDREA MASSÉ, PASCAL FRIEDERICH, VELIMIR MEDED, WOLFGANG WENZEL, PETER A. BOBBERT
Effects of energy correlations and superexchange on charge transport and exciton formation in amorphous molecular semiconductors: An ab initio study

TANJA SCHNEIDER, FELIX LIMBERG, KELVIN YAO, ARDALAN ARMIN, NILS JÜRGENSEN, JENS CZOLK, PASCAL FRIEDERICH, WOLFGANG WENZEL, M. BRUNS, JAN BEHRENDS, HARTMUT KRÜGER AND ALEXANDER COLSMANN
Solution-processed p-doped hole injection layers for highly efficient organic light emitting diodes

TOBIAS SETZER, PASCAL FRIEDERICH, FRANZ SYMALLA, VELIMIR MEDED, ANDREAS DREUW, WOLFGANG WENZEL AND CHRISTIAN LENNARTZ
Beyond Exciton-Positive Polaron Interaction in Blue Phosphorescent Organic Light Emitting Diodes

PASCAL FRIEDERICH, MICHAEL JENNE, CHRISTIAN SPRAU, ANDREA MAGRI, VERÓNICA GÓMEZ, VELIMIR MEDED, FRANK SCHRAMM, ALEXANDER COLSMANN, MARIO RUBEN, WOLFGANG WENZEL
Thin film charge mobility of Alq_3-derivatives: Towards in-silico rational design in organic electronics

PASCAL FRIEDERICH, VADIM RODIN, FLORIAN VON WROCHEM AND WOLFGANG WENZEL
Theoretical investigation of the giant surface potential effect in amorphous organic semiconductors

SUBMITTED

16. FRANZ SYMALLA, PASCAL FRIEDERICH, ANDREA MASSÉ, VELIMIR MEDED, REINDER COEHOORN, PETER BOBBERT AND WOLFGANG WENZEL
Charge transport by superexchange in molecular host-guest systems
Submitted to PRL

15. FEILONG LIU, ANDREA MASSÉ, PASCAL FRIEDERICH, FRANZ SYMALLA, ROBERT NITSCHE, WOLFGANG WENZEL, REINDER COEHOORN AND PETER A. BOBBERT
Ab initio modeling of impedance spectroscopy on hole-only α-NPD devices
Sumitted to APL

14. TANJA SCHNEIDER, FELIX LIMBERG, KELVIN YAO, ARDALAN ARMIN, NILS JÜRGENSEN, JENS CZOLK, BERND EBENHOCH, PASCAL FRIEDERICH, WOLFGANG WENZEL, JAN BEHRENDS, HARTMUT KRÜGER AND ALEXANDER COLSMANN
p-Doping of polystyrene polymers with attached functional side-groups from solution
Submitted to the Journal of Materials Chemistry C

2016

13. TESSY BABY, MANUEL ROMMEL, PASCAL FRIEDERICH, FALK VON SEGGERN, SIMONE DEHM, CHRISTIAN REITZ, CHRISTIAN KÜBEL, WOLFGANG WENZEL, HORST HAHN AND SUBHO DASGUPTA
Sub-50 nm channel vertical field-effect transistors using conventional ink-jet printing
Accepted in Adv. Mater., 2016

12. ANDREA MASSÉ, PASCAL FRIEDERICH, FRANZ SYMALLA, WOLFGANG WENZEL, ROBERT NITSCHE, REINDER COEHOORN AND PETER A. BOBBERT
Ab-initio charge-carrier mobility model of amorphous molecular semiconductors
Phys. Rev. B, 2016, 93, Pages 195-209

165

11. Pascal Friederich, Velimir Meded, Angela Poschlad, Tobias Neumann, Vadim Rodin, Vera Stehr, Franz Symalla, Denis Danilov, Gesa Lüdemann, Reinhold F. Fink, Ivan Kondov, Florian von Wrochem and Wolfgang Wenzel
Molecular origin of the charge carrier mobility in small molecule organic semiconductors
Adv. Functional Mater. 2016, 26 (31), Pages 5757-5763

10. Pascal Friederich, Timo Strunk, Wolfgang Wenzel and Ivan Kondov
Multiscale simulation of organic electronics via smart scheduling of quantum mechanics computations
Procedia Comput. Sci., 2016, 80, Pages 1244-1254

9. Tobias Neumann, Jianxi Liu, Tobias Wächter, Pascal Friederich, Franz Symalla, Alexander Welle, Veronica Mugnaini, Velimir Meded, Michael Zharnikov, Christof Wöll and Wolfgang Wenzel
Superexchange charge transport in loaded metal organic frameworks
ACS Nano, 2016, 10, Pages 7085-7093

2015

8. Tobias Mönch, Pascal Friederich, Felix Holzmueller, Bogdan Rutkowski, Johannes Benduhn, Timo Strunk, Christian Koerner, Koen Vandewal, Aleksandra Czyrska-Filemonowicz, Wolfgang Wenzel and Karl Leo
Influence of meso and nanoscale structure on the properties of highly efficient small molecule solar cells
Adv. Energy Mater., 2015

7. Barbara Branchi, Zoi Karipidou, Mustafa Sarpasan, Nikolaus Knorr, Vadim Rodin, Pascal Friederich, Tobias Neumann, Velimir Meded, Silvia Rosselli, Gabriele Nelles, Wolfgang Wenzel, Maria Anita Rampi and Florian von Wrochem
Ultra-robust thin film devices from self-assembled metal-terpyridine oligomers
Adv. Mater., 2015, 28, Pages 3473-3480

6. Pascal Friederich, Velimir Meded, Franz Symalla, Marcus Elstner and Wolfgang Wenzel
QM/QM approach to model energy disorder in amorphous organic semiconductors
J. Chem. Theory Comput., 2015, 11 (2), Pages 560-567

166

5. Vadim Rodin, Franz Symalla, Velimir Meded, Pascal Friederich, Denis Danilov, Angela Poschlad, Gabriele Nelles, Florian von Wrochem and Wolfgang Wenzel
Generalized effective-medium model for the carrier mobility in amorphous organic semiconductors
Phys. Rev. B, 2015, 91, 155203

4. Velimir Meded, Pascal Friederich, Franz Symalla, Tobias Neumann, Denis Danilov and Wolfgang Wenzel
A self-consistent first-principle based approach to model carrier mobility in organic materials
AIP Conf. Proc., 2015, 1702, 090027

3. Andrea Magri, Pascal Friederich, Bernhard Schäfer, Valeria Fattori, Xiangnan Sun, Timo Strunk, Velimir Meded, Luis E. Hueso, Wolfgang Wenzel and Mario Ruben
Charge carrier mobility and electronic properties of Al(Op)$_3$: impact of excimer formation
Beilstein J. Nanotechnol., 2015, 6, Pages 1107-1115

2. Tobias Mönch, Tejas S. Sherkar, L. Jan Anton Koster, Pascal Friederich, Moritz Riede, Peter Formanek, Christian Koerner, Koen Vandewal, Wolfgang Wenzel and Karl Leo
Experimental and theoretical study of phase separation in ZnPc:C$_{60}$ blends
Org. Electron., 2015, 27, Pages 183-191

2014

1. Pascal Friederich, Franz Symalla, Velimir Meded, Tobias Neumann and Wolfgang Wenzel
Ab initio treatment of disorder effects in amorphous organic materials: Toward parameter free materials simulation
J. Chem. Theory Comput., 2014, 10 (9), Pages 3720-3725

Conference and Collaboration contributions

Oral presentations

- 8th Multiscale Materials Modeling (MMM) International Conference 2016, Dijon, France
  Molecular origin of the charge carrier mobility in small molecule organic semiconductors

- European Congress and Exhibition on Advanced Materials and Processes (EUROMAT) 2015, Warsaw, Poland
  Simulation of morphology and charge transport in printed field effect transistors

- Collaboration meeting with a scientific committee of Sony Europe (Materials Science Laboratory) and Sony Japan (Advanced Materials Laboratories), 2014, 2015 and 2016

- Collaboration meeting of the MODEOLED project with scientific committee of TU Eindhoven, BASF Ludwigshafen and Philips Eindhoven, 2014, 2015 and 2016

Poster presentations

- 8th Multiscale Materials Modeling (MMM) international conference 2016, Dijon, France
  Influence of meso and nanoscale structure on the properties of highly efficient small molecule solar cells

- 8th Multiscale Materials Modeling (MMM) international conference 2016, Dijon, France
  Charge transport in OLED guest host systems: The role of molecular superexchange

- 8th International Conference on Molecular Electronics (ElecMol) 2016, Paris, France
  Parameter-free mobility prediction and OLED material design

- Stipendiary meeting of the Carl-Zeiss-Stiftung 2015, Oberkochen, Germany
  Parameter-free mobility prediction and OLED material design

- European Materials Research Society (E-MRS) Spring Meeting 2014, Lille, France
  Ab-initio simulation of charge transport in amorphous organic materials: Towards parameter-free materials simulation

- Organic Electronics Summer School 2014, Boutheon, France
  Ab-initio simulation of charge transport in amorphous organic materials: Towards parameter-free materials simulation

- Stipendiary meeting of the Carl-Zeiss-Stiftung 2014, Mainz, Germany
  Ab-initio simulation of charge transport in amorphous organic materials: Towards parameter-free materials simulation

- POF3 Evaluation 2014, Karlsruhe, Germany
  Self-consistent first-principles treatment of disorder effects in organic conductors

Miscellaneous

- 65th Lindau Nobel Laureate Meeting 2015, Lindau, Germany

A
Acknowledgment